Microstructure and phase stability of multi-phase alloys in refractory-metal base systems

by

Li PENG

Dissertation submitted in partial fulfillment of

the requirements for the degree of Doctor of Philosophy

HOKKAIDO
UNIVERSITY

Graduate School of Materials Science and Engineering

Hokkaido University, Hokkaido, Japan

Supervisor: Professor Seiji Miura

Acknowledgement

First, I would like to first thank Prof. Seiji Miura for giving me the opportunity of studying in his laboratory. His invaluable guidance and advice have pointed out the direction toward my research. His down-to-earth attitude toward research and the way of solving problems will benefit me in my whole life. Prof. Miura also has given me several opportunities to conduct academic communications through attending national or international conferences and writing publications.

I would also like to thank associate Prof. Ken-ichi Ikeda for his advices on presentations and experiments. Also, many thanks to his help on TEM observation and discussions given for the thesis.

I would like to thank to assistant Prof. Satoshi Takizawa for his advices and discussions on how to understand and explain experimental results through calculation aspects.

I would also like to thank research assistant staff Hiroyuki Uesugi for his arrangement on consumables in laboratory, reservation of experimental facilities, and the operation methods of experimental apparatuses.

I would like to address my thanks to Dr. Takuya Yamanouchi and Dr. Takahiro Mineta who have already graduated. They have helped me a lot both in research work and life when I was just enrolled in Hokkaido University. Thanks to them that I can adapt the study and life in Japan so fast.

Many thanks to my research group members for their assistance and the time we spent together. They are Dr. Soma, graduate students Mr. Mastuzaki, Mr. Miyakawa, Mr. Satou, Mr. Fukagawa, Mr. Moriyama, Mr. Yasumoto, Mr. Yamanaka, Mr. Goto, Mr. Yasuhara, Mr. TianHang Sun, Mr. Shirakami and undergraduate students Mr. Ishizaka, Mr. Kudo, Mr. Nakano and Mr. Hashimoto.

In addition, I would like thank specially appointed assistant Prof. YongMing Wang, Mr. Miyazaki, Mr. Endo and Ms. Kurishiba from Laboratory of Nano-Mirco Materials Analysis for their help on operating EPMA, FIB and TEM. And many thanks to Mr.

Suzuki from Laboratory of XPS analysis for his help on how to process the sample surface by CP and the operation of AES apparatus.

Lastly, I would like to thank my family and friends for their support and encouragement.

Abstract

The AB_2-type intermetallic Laves phases with topologically close-packed (TCP) structures have been considered for high-temperature structural materials, because of their high melting points and attractive mechanical properties at elevated temperature. Although the concept of ductile phase toughening has been applied to improve their room temperature toughness of some alloys including Nb/$NbCr_2$ and Cr/$TaCr_2$, the strength of the ductile phase, mostly the BCC structure for refractory-metal based materials, is not adequate at high temperatures. To overcome this trade-off, a new BCC_1/BCC_2/Laves three-phase alloy is proposed. It is intended to introduce second BCC phase with a fine structure to bring the BCC_1/BCC_2 interfaces into the conventional single ductile phase and AB_2 Laves phases disperse in the BCC_1/BCC_2 two-phase microstructure.

To design the alloy composition and determine the heat treatment temperature, the isothermal sections of the Cr-Mo-Nb ternary phase diagram have been studied. The C15 NbCr2 Laves precipitation behavior in three different alloys has been investigated in the Cr-Mo-Nb ternary system. The orientation relationship (OR) of NbCr2 in BCC matrix among BCC/Laves two-phase alloys and Cr-rich BCC1/Mo-rich BCC2/Laves three-phase alloy is different at 1473 K; OR 1: (011)BCC // $(11\bar{1})$C15, $[0\bar{1}1]$BCC // $[\bar{1}10]$C15 and OR 2: $(\bar{4}11)$BCC // (111)C15, $[0\bar{1}1]$BCC // $[\bar{1}10]$C15 with low lattice mismatch are both observed in Cr-rich alloys #3 (74Cr-16Mo-10Nb) and #2 (50Cr-30Mo-20Nb). OR 3: (011)BCC // (111)C15, $[\bar{1}1\bar{1}]$BCC // $[01\bar{1}]$C15 with a lattice mismatch relatively larger than that of OR 1 and OR 2 is only observed in alloy #2, which may be due to the presence of BCC_1 and BCC_2 interphases formed after BCC decomposition. Only discontinuous precipitation is observed at grain boundaries in Cr-lean alloy #1 (42Cr-31Mo-27Nb) without obvious OR between the BCC matrix and Laves phase.

The supersaturated BCC single-phase solid solution alloy obtained by homogenization at 1973 K for 1 h underwent microstructural evolution during heat

treatment at 1473 K. Intragranular nucleation of the Cr-rich BCC_1 phase occurred, which led to the formation of an alternating BCC_1/BCC_2 two-phase microstructure through a discontinuous precipitation process, followed by nucleation of the Laves phase at the BCC_1/BCC_2 interphase boundaries. At a higher temperature of 1523 K, a similar microstructure was obtained, with increased BCC decomposition and Laves precipitation rates, while the alloy consisted of BCC and Laves phase at 1773 K. A similar microstructure was obtained with increased BCC decomposition and Laves precipitation rates at 1523 K, while the alloy consisted of BCC and Laves phase at 1773 K. The mechanical properties of alloys heat treated at 1473 K for various periods after the solid solution treatment were also investigated. The highest fracture compressive strength of 1493 MPa and minimum hardness of 773±7 HV were obtained for the alloy aged for 24 h, where the BCC_1/BCC_2 two-phase microstructure dominates. The Vickers hardness of the alloy aged for 72 h with a fine structure including the Laves phase was 839±8 HV under a load of 0.5 kgf, and no obvious microcracks were observed.

Besides, silicon has been chosen to add to the Cr-Mo-Nb system to study the stability of $NbCr_2$ Laves phase. It is found that the amount of Laves phase in as-cast increases with the increase of the Si addition. In 1973 K heat-treated alloys with 0.5Si and 1Si, Laves phase still exists. It is also found that Si is enriched in $NbCr_2$ phase and Mo is also tend to be distributed into the Laves phase. It indicates that $NbCr_2$ is relatively stabilized with Si addition and the solvus line of BCC moves towards Mo-rich direction.

Table of Contents

Chapter 1

Introduction

The higher operation temperatures are pursued for gas turbines in order to obtain higher efficiency. Higher operation temperatures require high-temperature materials that can serve in the severe environment. The conventional Nickel-base superalloys are mostly widely used high-temperature structure materials because of the good combination of chemical resistance and mechanical properties. However, this class of materials will soon reach the limits of application and cannot meet the increasing demand of structural materials that can operate at higher temperatures due to the relatively low melting temperature. The refractory metals, especially Nb and Mo, which have relatively low density and high melting temperatures, are one of the candidates. However, these metals are susceptible to oxidation at high temperature. On the other hand, intermetallic compounds are also very attractive as high temperature structural materials because of their high melting temperatures and superior high-temperature strength. The mechanical properties at ambient conditions are still insufficient for application in a single-phase form due to their complex structures. This chapter will firstly discuss the traditional Ni-base superalloys. Then the development of potential candidate materials, especially Nb-base alloys and intermetallics, will be provided. Finally, in consideration of the limitation of these candidates, a new BCC_1/BCC_2/Laves three-phase alloy will be put forward based on the atomic size.

1.1 Ni-base superalloys

Ni-base superalloys are the most widely used materials for turbine blades to increase the operating temperature of gas turbines because of their excellent mechanical properties, high strength, good creep resistance, as well as corrosion and oxidation resistance, at high temperatures.

The ever-changing demand of the higher efficiency of turbine engines, which is

governed by the turbine inlet temperature (TIT), promotes the development of Ni-base superalloys. Tremendous success has been achieved in designing new alloy compositions to increase the operating temperature in the past several decades. Different types of Ni-base superalloys may have different microstructures and mechanical properties, depending on which component of turbine engines these alloys are designed for. Single-crystal Ni-base superalloys are more commonly used than poly-crystal Ni-base superalloys for turbine blades due to better creep and fatigue properties. Grain boundary (GB) is detrimental to the creep property. GB sliding is avoided by using singe-crystal superalloys. Besides, single-crystal superalloys have different properties in different directions. The stresses will be lower for a crystal orientation with a low Young's modulus when a constant strain is considered. Therefore, fatigue life can be enhanced by choosing the crystallographic direction with a lower Young's modulus.

The typical microstructure of Ni-based single-crystal superalloys is a dual phase microstructure, which is composed of a disordered a FCC structured γ matrix and ordered $L1_2$ intermetallic precipitates γ' phase, see Fig. 1 [1]. The cuboidal γ' precipitates are surrounded by γ matrix.

The γ' phase plays an important role in the high temperature mechanical properties. The morphology of the γ' precipitates affects the creep performances of Ni-base superalloys.

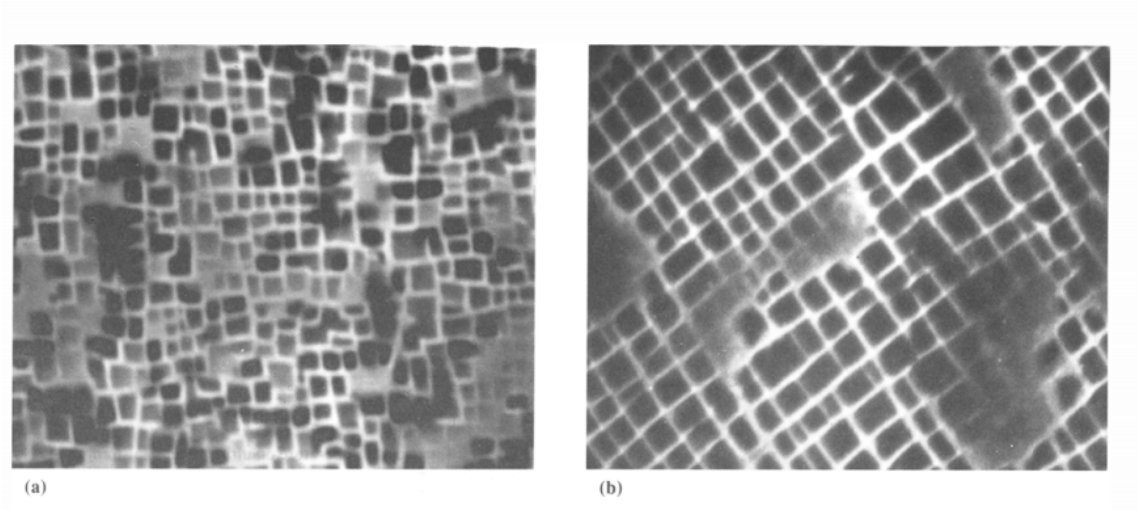

Fig. 1. The microstructures of single-crystal Ni-base superalloy CMSX-4 with different heat-treated conditions. (a) final aging at 871˚C for 20 h, (b) final aging at 871˚C for 100 h [1].

The γ' phase plays an important role in the high temperature mechanical properties. The morphology of the γ' precipitates affects the creep performances of Ni-base superalloys.

Murakumo el al. [2] investigated the creep strength of Ni-base superalloys with various γ' phase volume fractions at 900 ˚C, 392 MPa and 1100 ˚C, 137 MPa. Fig. 2 shows the effect of the volume fraction of γ' phase on creep rupture life of TMS-75 and TMS-82. The creep rupture life reaches a peak when the volume fraction of γ' phase is in the range of 60%~75% for both alloys.

Nathal [3] studied the influence of initial γ' shape and size on the creep rupture life of MAR-M200 superalloy. Fig. 3 shows the relationship between initial γ' shape and size and the creep life. Three types of precipitate morphologies were evaluated, spherical, cuboidal and irregular raft. The highest creep life was obtained when the alloy presented a cuboidal morphology and the optimal initial size of cuboidal γ' shape is around 0.5 μm.

A typical example of A_3B $L1_2$ ordered structure is Ni_3Al, the Ni atoms occupy the face-centered positions and Al atoms in the corners of the cube [4], see Fig. 4. The ordered $L1_2$ γ' phase has a high selectivity of elements. In addition to Ni and Al, the other common precipitation elements are Ti and Ta [5, 6], therefore, it can be expressed as Ni_3(Al, Ti, Ta). The alloying elements also influence the strength and plasticity of γ' phase by changing the formation energy of APB.

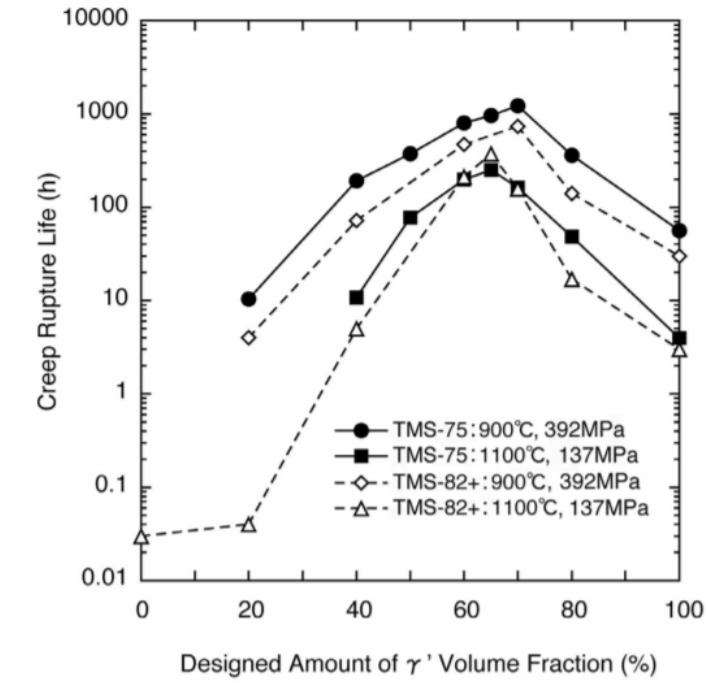

Fig. 2. Effect of the volume of the volume fraction of γ' phase on creep rupture life [2].

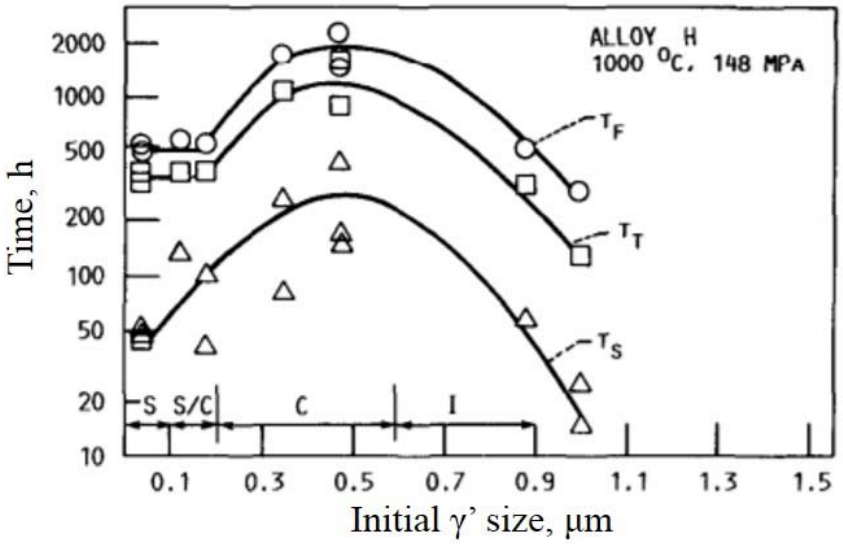

Fig. 3. Effect of the initial size of γ' phase on creep rupture life of MAR-M200 superalloy. T_F: the time of final rupture, T_T: the third stage creep, T_S: the second stage creep. The shapes of γ' precipitates are presented: S, spheroidal; C, cuboidal; I irregular raft [3].

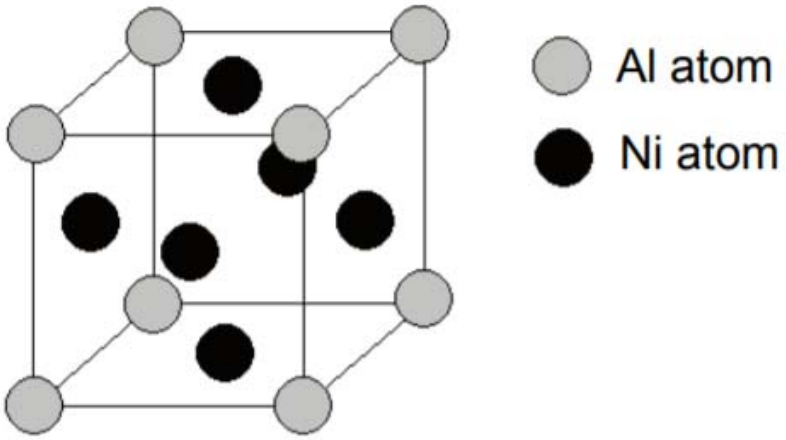

Fig. 4. A_3B type $L1_2$ ordered structure of the γ' phase.

Ni-base superalloy is mainly strengthened by γ' phase by two mechanisms: precipitation strengthening and structural strengthening. The γ' precipitates maintain coherent interfaces with the γ phase matrix. The interfaces between γ and γ' phases impede dislocation motion effectively. The γ' phase has an ordered crystal structure which is less tolerant to dislocations. When a dislocation cuts through an ordered precipitate, a faulted interface called anti-phase boundary (APB) [7] is created. The high interfacial energy associated with APB hinders the movement of dislocation and prevents it from entering the precipitate. Both of them are effective in lowering creep rate and extending service life.

The coherency between γ and γ' phases is quantified by lattice misfit δ, which has strong effect on the density of dislocation and the creep rupture life of the Ni-base superalloys [8]. A small value of lattice misfit indicates high coherency. The lattice misfit can be adjusted by controlling the segregation of the alloying elements in γ and γ' phases [9, 10]. The lattice misfit is defined as:

$$\delta = 2 \times \frac{a_\gamma - a_{\gamma'}}{a_\gamma + a_{\gamma'}} \tag{1}$$

where a_γ and $a_{\gamma'}$ are the lattice parameters of γ and γ' phases, respectively [7]. A preferable microstructure and thermal stability can be expected with a small lattice misfit where γ' coarsening is restricted. The value of lattice misfit has large effect on the morphology of γ' phase [11], see Fig. 5. It is suggested by Nathal [3] that the γ' precipitates are cuboids when the lattice misfit is less than 0.5%. The precipitates become spherical when the magnitude of the lattice mismatch increases due to the loss of coherency. Besides, the lattice misfit is also depending on the temperature. Since the thermal expansion coefficient of γ' phase is smaller than that of γ phase [12], the lattice misfit becomes more negative as the temperature increases.

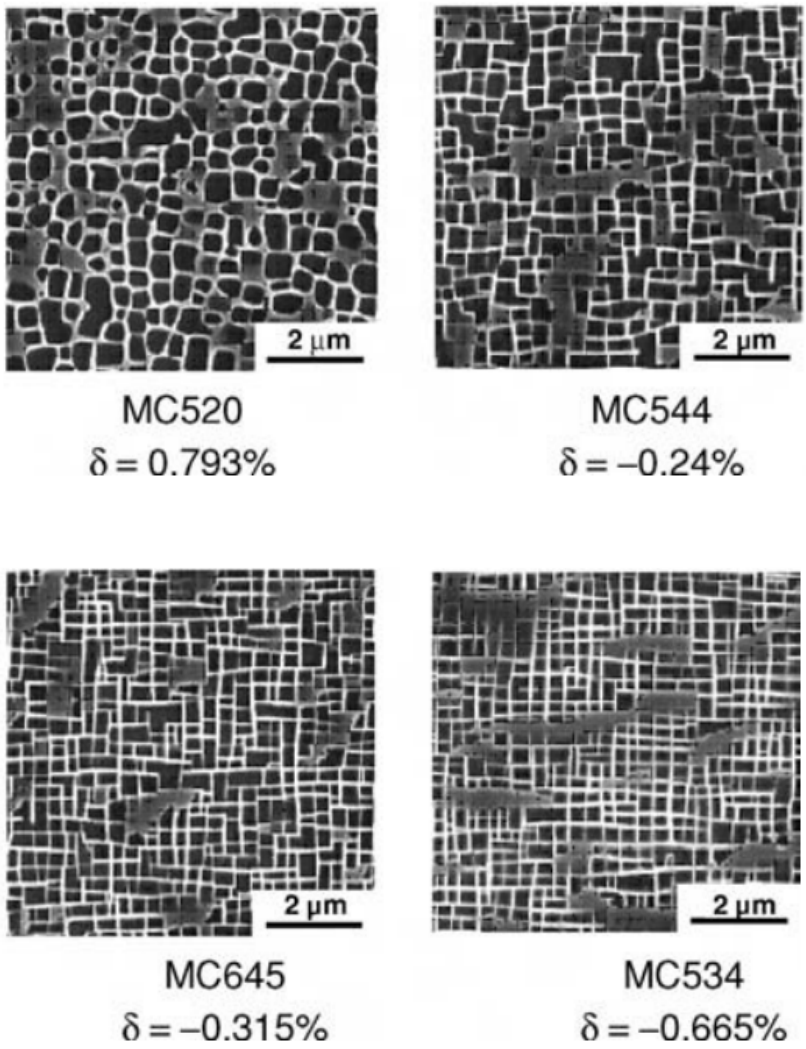

Fig. 5. Relationship between lattice misfit and the shape of the γ' precipitates.

The alloying elements have been adopted not just to adjust the lattice misfit, but also to introduce solid solution strengthening effect to γ phase. The typical alloying elements are Cr, Co, Mo, W, Re and Ru. In addition to introducing solid solution strengthening effect, these elements can also increase the solidus temperatures and decrease the stacking fault energy, which will enhance the thermal stability of γ phase and hinder the motion of dislocation. The atomic diameters of all the alloying elements are larger than that of Ni in Ni-base superalloys [7, 13], following the order of Ni<Co<Cr<Ru<Mo<W. Thus, the lattice parameter of γ phase will always decrease with these alloying elements.

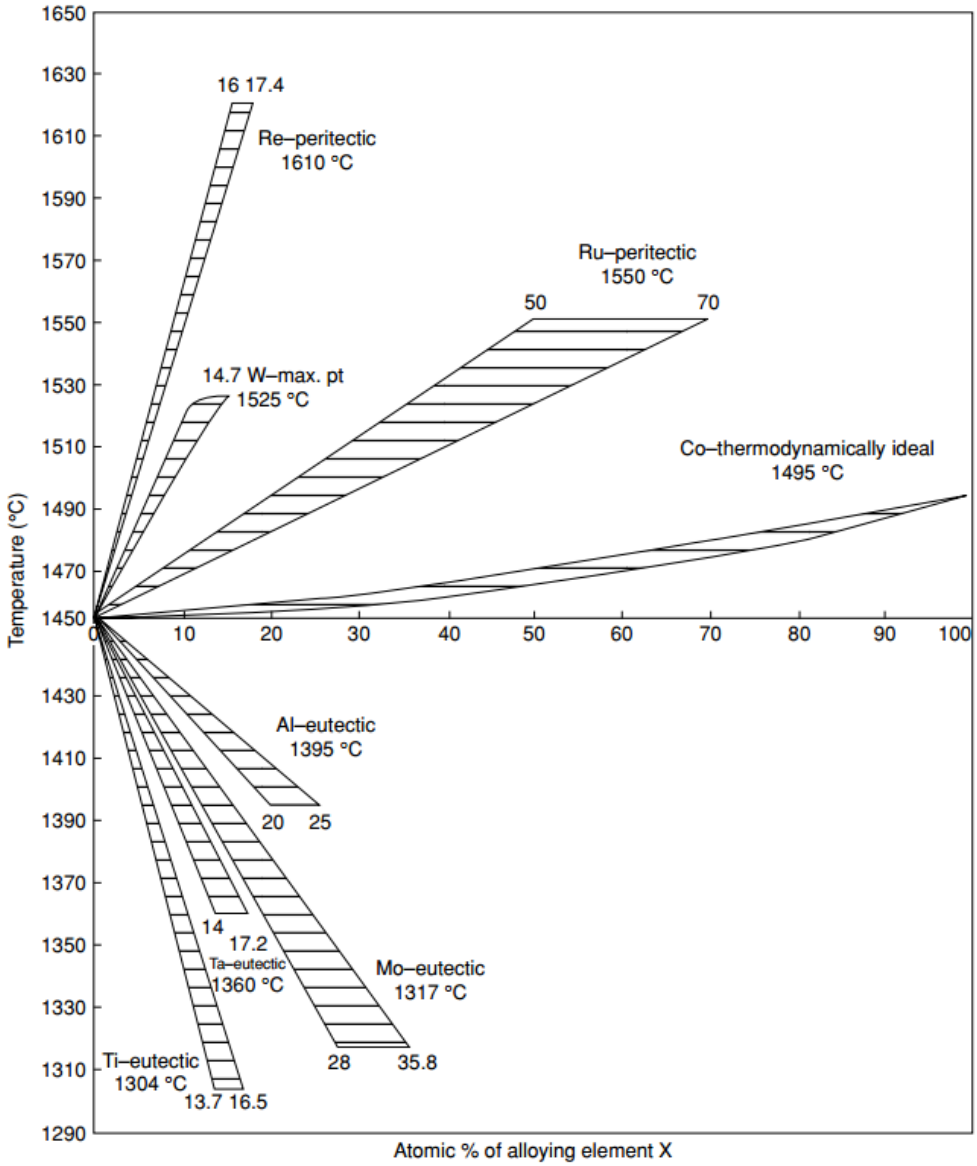

Fig. 6. The solidus and liquidus lines with alloys element X [7].

Fig. 6 shows the solidus and liquidus lines in different Ni-X binary systems [7]. The horizontal line indicates the melting temperature of Ni (1450 ˚C). As is seen in Fig. 6, there are two types of elements, which type I (Re, W, Ru, Co) increases the liquidus and solidus temperatures and type II (Ti, Mo, Ta, Cr) decreases the liquidus and solidus tempreatures. The effect of the alloying elements on the liquidus and solidus does not correlate with their melting temperatures. For example, W and Ta increase and decrease the liquidus temperature by about +5 K/at% and -5 K/at% of solute, respectively. The element Re, however, is notable for its strong positive influence on the liquidus temperature. In order to keep the melting temperature of a superalloy higher than that of the γ' phase (1668 K for Ni_3Al), the amount of additional elements of type II must be restricted to a suitable level.

It should be noted that alloying elements Cr [14, 15], Mo [16, 17], W [18] and Re [19, 20] have been reported to facilitate the formation of topologically close-packed (TCP) phases, like σ, μ and P phases. The formation of TCP phases consumes these elements and reduces the solid solution strengthening effect on γ phase.

In practical application, although the thermal barrier coatings (TBC) and cooling systems are employed to increase the operating temperature of Ni-base superalloys, the melting temperature of Ni limits its development for the further demand of higher efficiency. The materials with higher melting temperature and can operate at high temperatures are preferred. The promising candidates are refractory-base alloys with high melting temperature and room-temperature ductility, especially Nb and Mo, and intermetallics with high melting temperature and good high temperature strength.

The intermetallic compounds are one of the promising candidate for Ni-base superalloys due to their high melting points and good high temperature strength. Nb silicide and Lave phase are considered to have great potential for turbine applications.

1.2 Laves phase

The refractory metals and their intermetallic compounds with high melting temperature and high-temperature strength [21, 22] are considered to be the candidates for high-temperature structural materials for turbine blades to increase the operating temperature of gas turbines. The AB_2-type intermetallic Laves phases with topologically close-packed (TCP) structures are classified into such intermetallic compounds group, the ideal atomic size ratio R_A/R_B is 1.225 [23] (where R_A and R_B are diameters of A and B atoms, respectively, and in general, $R_A>R_B$). [24, 25]. In reality for elements forming Laves phases, the size ratio has been found to lie between 1.05 and 1.68. To interpret such deviant ratios, it is not hard to understand that atoms of one sort have to be compressed, the other on expanded, to reach the ideal ratio. There are three major types of Laves phases, the cubic $MgCu_2$ type C15 phase, the hexagonal $MgZn_2$ C14 phase and the dihexagonal $MgNi_2$ C36 phase, as shown in Fig. 7 [26]. These consist of double layers of hexagonal arrays of A atoms surrounded by tetrahedral of the B elements. One stacking layer consists of four sub-layers, and thus, they are called quadruple layers. The cubic C15 structure consists of such layers stacked ABCABC, while the C14 consists of such layers stacked ABABABAB. C36 may be regarded as a transitional phase between the C15 and C14 structures with a stacking of these layers ABACABAC.

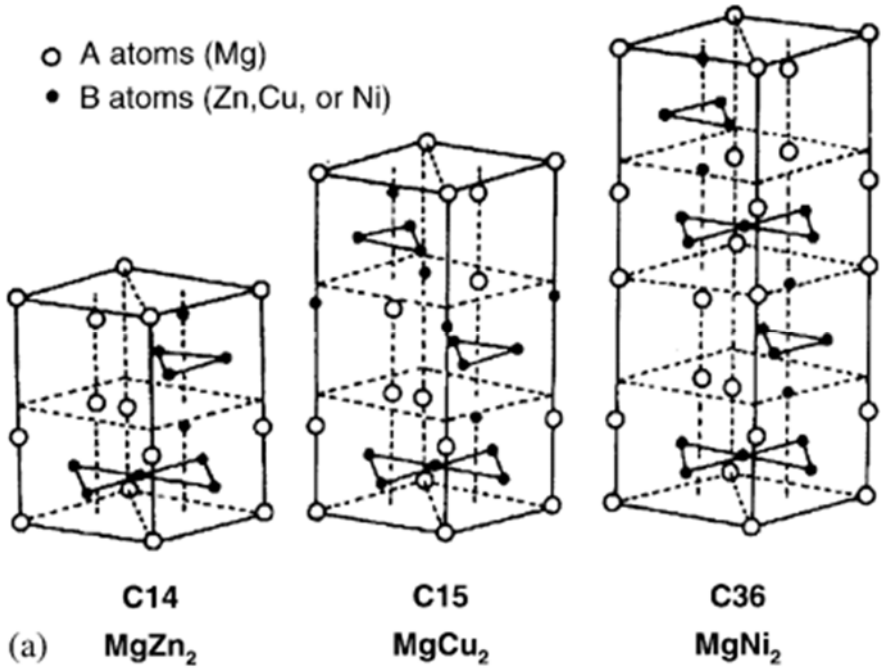

Fig. 7. The three types of Laves phase structure [26].

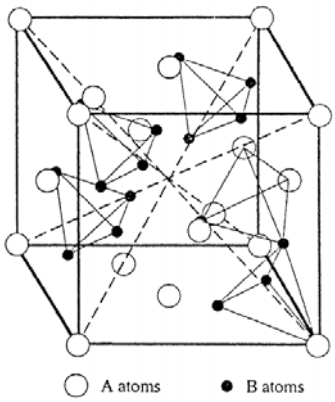

Fig. 8. Crystal structure of C15 Laves phase [27].

1.2.1 Factors affecting the structure and stability of Laves phase

It is not easy to predict whether a Laves phase occurs in a particular alloy system and which of the possible polytype is the stable one. It is known that some geometric and electronic factors such as the atomic size ratio of A and B atoms, electronegativities and their valence electron numbers affect the occurrence of a Laves phase. Some researchers have discussed the influence of the different factors on the stability of Laves phase [24, 28, 29]. A model in terms of only one of these factors cannot be enough to discuss the formation of Laves phases.

Fig. 9 shows the real size ratios lie in a certain range and there is no obvious relationship between the size ratio and the structure type of Laves phase, especially for some C14 Laves phases with very large size ratios, e.g. 1.517 for $YbCu_2$ and 1.648 for KAu_2 [30]. Dwight [31] concluded from the observed deviations of the radius ratios from the ideal value that the radii of the atoms in a Laves phase is different from those of the pure A and B metals and that the major factor controlling the formation of Laves phases is the ability of the atoms to contract or expand in order to obtain the ideal ratio, which had already discussed by Laves [32].

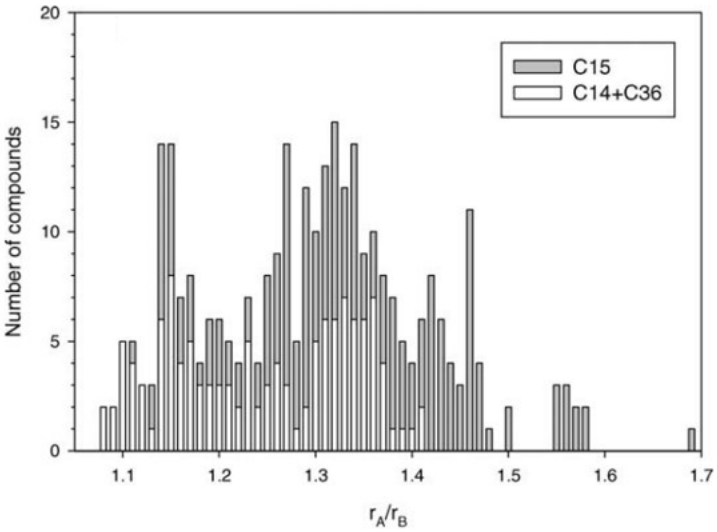

Fig. 9. Frequency of Laves phase structure type vs. atomic size ratio r_A/r_B (data form Ref. [33]) [26].

Zhu et al. [34] studied the effect of atomic size ratio on the enthalpies of formation of Laves phases and plotted the enthalpies of formation of a large number of Laves phases as a function of the atomic radius ratio, as shown in Fig. 10. Two lines have been drawn and enveloped all the data points with the line, $\Delta H=0$. The two lines intersect at the ideal radius ratio of 1.225, which indicates the most stable Laves phases may be found at the ideal atomic size ratio. Furthermore, the two lines intersect with the line, $\Delta H=0$, at $R_A/R_B=1.03$ and $R_A/R_B=1.65$, which are the about the observed lower and upper limit of R_A/R_B for Laves phases. Based on the observation, a thermodynamic interpretation of the size ratio limits for Laves phase formation has also provided by them [35].

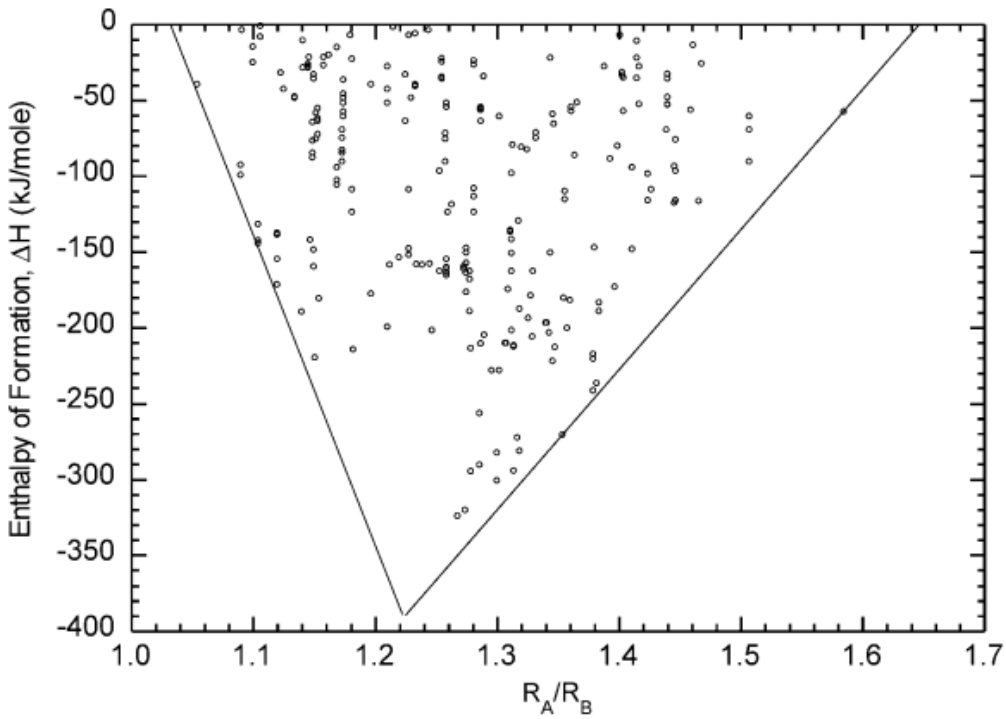

Fig. 10. Enthalpy of formation versus R_A/R_B for binary Laves phases [34].

Edwards [36] studied the influence of the difference in electronegativities of A and B atoms on the atomic sizes in Laves phase structure. The contraction caused by attractive interaction between A and B atoms is found to be proportional to the square of the difference in the electronegativities. The alloying effect on the interatomic potentials leads to a renormalization of the effective atomic radii. Especially the possibility of the formation of Laves phases with large non-ideal Goldschmidt radii ratios.

Laves and Witte [37] have already discussed the effect of average number of valence electrons (e/a) on the stable Laves phase structure. Fig. 11 shows the frequency of Laves phase as a function of the valence electron concentration (VEC). It is not possible to predict the stable Laves phase structure just from the VEC. Nevertheless, in Laves and Witte' studies [37], a valence electron concentration rule was found to control the occurrence of various Laves structures, with C15 stabilized at low e/a values, C14 stabilized at high e/a values, and C36 in between, as shown in Fig. 12. The correlation is reasonably good; however, both non-transition and transition metals were involved in forming some Laves phases in their study, making it difficult to analyze the VEC in the alloys. This difficulty results from the fact that for a transition element, the valence electron number is not a constant value, but varies in different systems. This behavior may contribute to the scattering in the critical e/a values corresponding to the phase transitions for the different ternary systems.

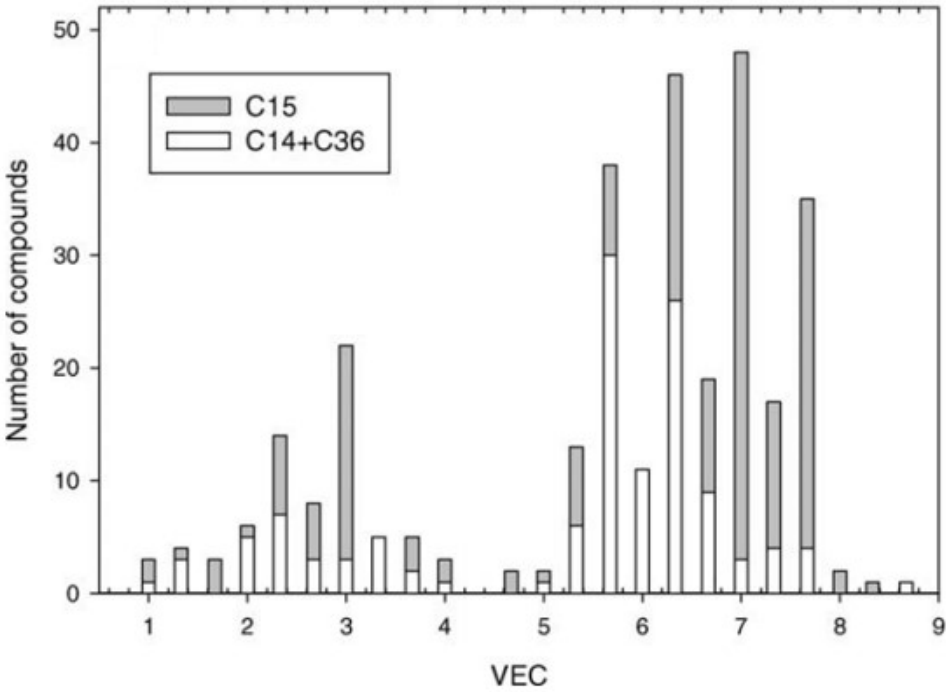

Fig. 11. Frequency of Laves phase structure type vs. VEC (data form Ref. [33]) [26].

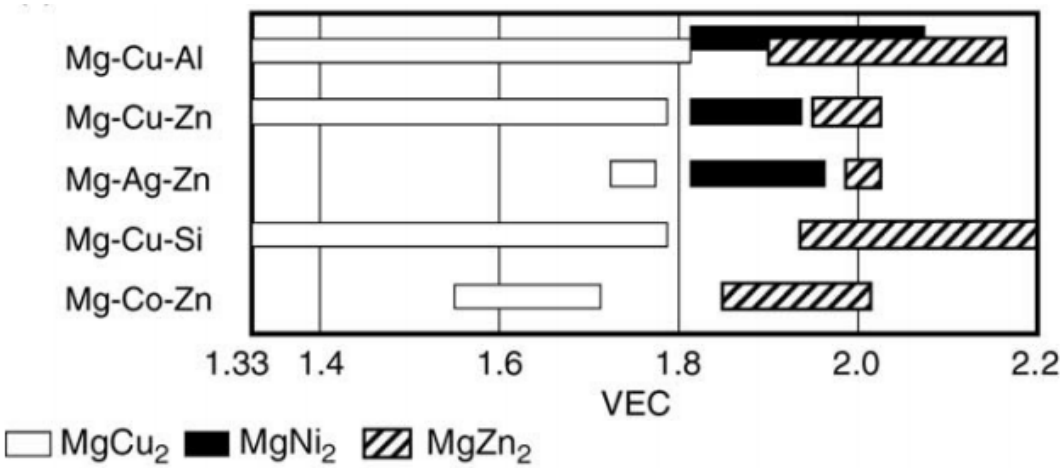

Fig. 12. Effect of the value of VEC on the Laves phase structure type in Mg-based Laves phases [37].

Zhu et al. [38, 39] selected a series of transition metal Laves phases. Instead of using the valence electron concentration, the average electron concentration was chosen for correlation purposes. With e/a ≤5.76, the C15 structure is stabilized; at an e/a range of 5.88–7.53, the C14 structure is stabilized; with e/a ≥ 7.65, the C15 structure is stabilized again. A further increase in electron concentration (e/a>8) leads to the disordering of the alloy. It is postulated that at 5.88>e/a>5.76 and 7.65>e/a>7.53, the C36 and other intermediate structures may be stabilized, as shown in Fig. 13. Still, this relation is only valid for this particular series of Laves phases. And the definition of the valencies for transition metal makes it more complicated. For example, different valencies of Ni have been taken in different studies [37, 40, 41].

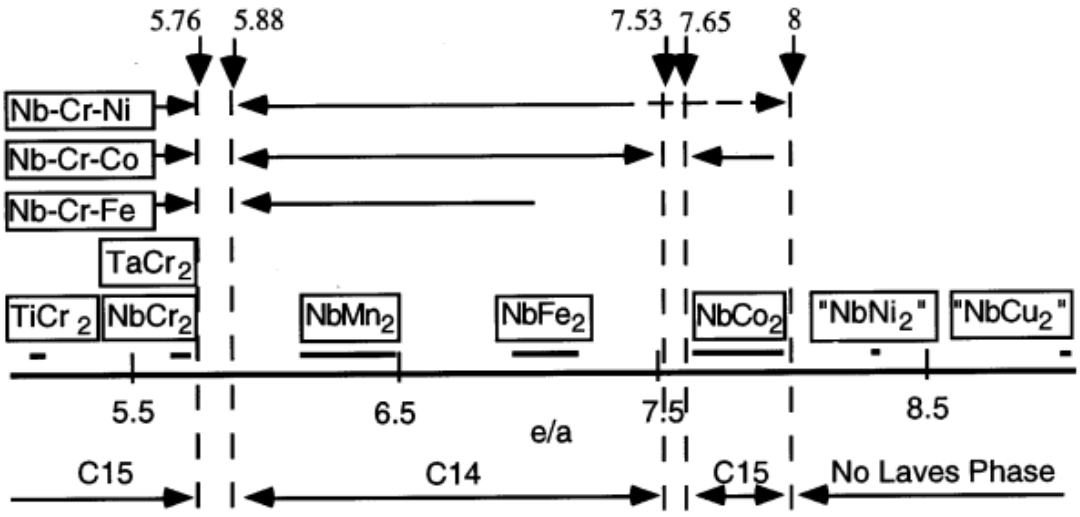

Fig. 13. Effect of the number of VEC on the polytype of a number of transition metal Laves phases [39].

Johannes et al. [42] also studied the relationship between VEC and Laves phase structures in transition metal Laves phases using first-principles total energy calculations. As is shown in Fig. 14, it is found that VECs between 3.4 and 4.9 C15 is the most stable structure, then C14 in the range 4.9–6.5, next C36 up to 6.9, again C15 up to 7.7, and finally C36 above 7.7.

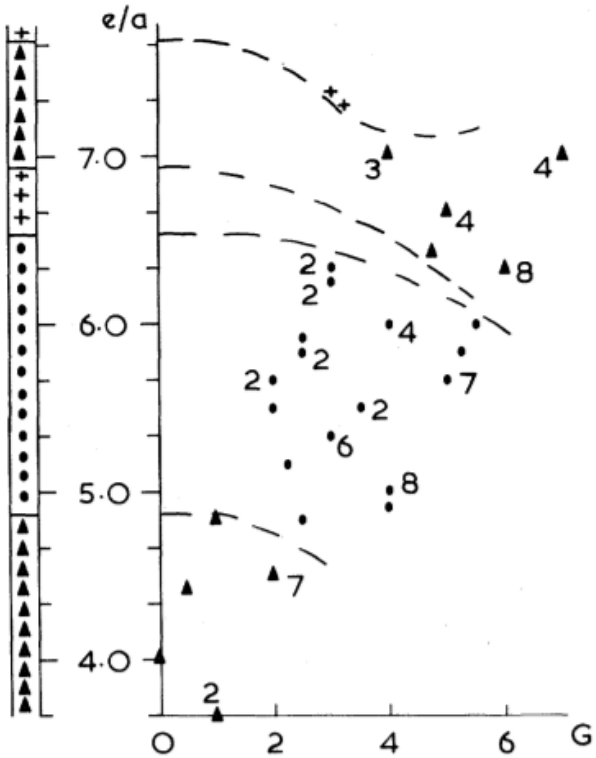

Fig. 14. Laves phase structures as a function of d-band filling per atom, e/a, and group-number difference G between components. ▲, $MgCu_2$ structure; ●, $MgZn_2$ structure; +, $MgNi_2$ structure [42].

The compound formation diagrams or so-called structure maps has been adopted to predict the stable Laves phase structure type. The structure maps show the stable structure types as a function of different factors such as atomic ratios, atomic numbers, electronegativities or VECs [43-45]. Fig. 15 shows the structure map for binary Laves phases with transition metal in terms of atomic ratio and the VEC [44]. The C14 Laves phases are stable in a certain range of VECs and radius ratios. However, there are still Laves phases do not follow the behavior. For example, the C14 Laves phase ZrAl2 with a VEC of 3.33 and a radius ratio of 1.19 lies outside the stability range.

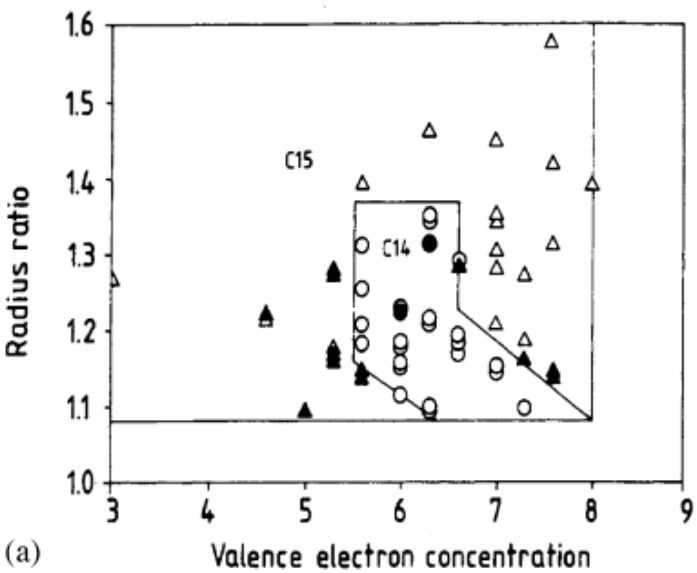

Fig. 15. Stability ranges of C14 and C15 binary transition metal Laves phases as a function of the VEC and the radius ratio (circles and triangles indicate C14 and C15 structures, respectively) [44].

Pettifor [46] introduced the so-called Mendeleev number M as a phenomenological coordinate which orders all the elements in the periodic table in a one-dimensional string. The order in this string of elements was chosen in a way giving the best structural separation for the binary AB compounds. The structure map for AB_2 transition metal compounds with the Mendeleev numbers of the A and B atoms as x and y axis, respectively, shows that all the Laves phase compounds are located above the diagonal M_A=M_B with hexagonal and cubic structures in well separated ranges, see Fig. 16. Nevertheless, the spreading of the data points loses the systematic relationship when non-transition metals are considered. For example, Laves phases $MgCu_2$, $MgZn_2$ and $MgNi_2$ are located near the diagonal because of M_{Mg}=73, M_{Cu}=72, M_{Zn}=76 and M_{Ni}=67.

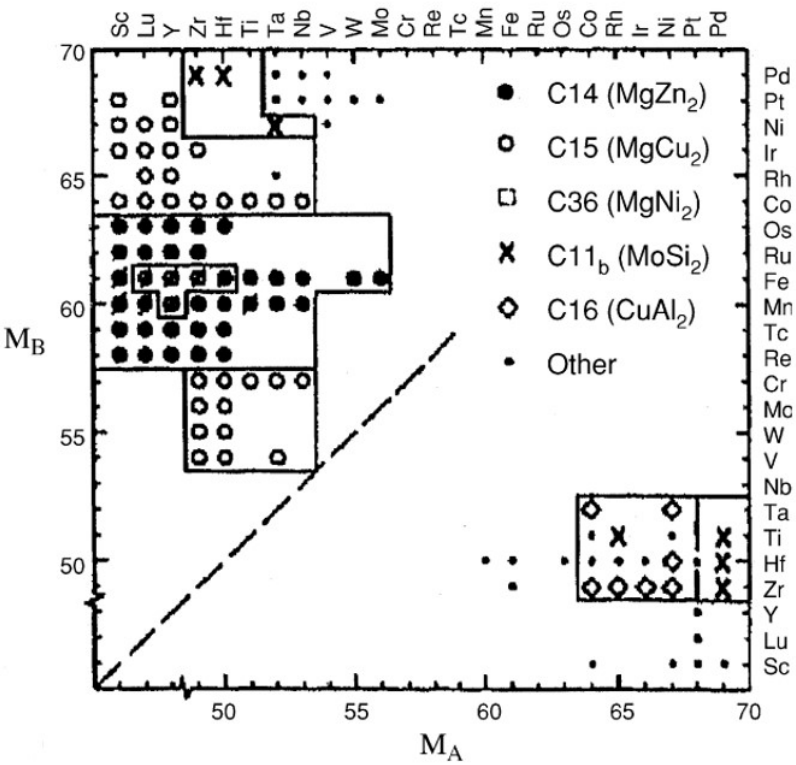

Fig. 16. The structure map for AB2 transition metal Laves phases as a function of the Mendeleev numbers of A and B atoms [43].

1.2.2 Effect of alloying elements

Laves phases may have extended homogeneity ranges to the A-rich, the B-rich or to both sides of the stoichiometric composition [24]. Antisite atoms, vacancies and the combinations of both enabled the occurrence of off-stoichiometric compositions. Alloying elements have been adopted to improve the fracture toughness of Laves phases [47-53]. Among the three types of Laves phases, the C15 structure is especially attractive due to the cubic structure, which suggests the existence of sufficient independent slip and/or twinning systems for general plastic deformation [54].

Inoue et al. [55, 56] have reported that Hf-Nb-V alloys with large volume fraction of C15 HfV_2-based Laves phase can be rolled without cracking at room temperature. Livingston and Hall [57] found that mechanical twinning with $\{111\}\langle 11\bar{2}\rangle$ system is the major deformation mode in C15 HfV_2-based Laves phase. the substitution of Nb into HfV2 appears to facilitate twinning by increasing the free volume in planes undergoing synchroshear [58]. Luzzi et al. [59] suggested two possible routes to improve the room temperature ductility of alloys containing C15 Laves phase. One is refining the grain size of Laves phase and the other one is to select proper alloy composition, which can reduce the stalking fault energy (SFE) of the cubic Laves phase.

Based on the size rule, Takasugi et al. [48] suggested the ternary C atoms with an intermediate atomic diameter ($R_A>R_B>R_C$) occupying either the A and B atoms, the atomic size ratio generally decreases, then improving the deformability of C15 Laves phase by increasing the free volume between synchroshear planes. It was found that alloying element Mo in $NbCr_2$ decreased the 0.2% yield stress and the brittle-ductile transition temperature (BDTT) in comparison with the unalloyed $NbCr_2$. However, no mechanical twinning occurred at low temperatures below BDTT in both unalloyed $NbCr_2$ and alloyed $NbCr_2$, which may be due to the high Peierls stress at low temperatures.

In order to find an appropriate alloying element for Laves phases and deformation mechanism, it is very important to understand the preferred site occupation of the added

elements. Lots of work has been done to study the site occupancies of additive elements in C15 $NbCr_2$ Laves phase [60-69]. Okaniwa et al. [61] studied the site occupancy by ALCHEMI on the Nb-Cr-X Laves phase. it was found that W, Ti and Mo prefer the Nb sites and V prefer the Cr sites. Yao et al. [70] studied the site occupancy behaviors of ternary additions of Ti, V, Zr, Mo and W in C15 $NbCr_2$ by first-principles calculations using the FLAPW method within the GGA and the supercell method. Long et al. [65] calculated the lattice parameters and the atomic free volumes of the $NbCr_2$ binary and ternary compounds using first-principles calculations. It is found that Re is the best choice to improve the fracture toughness of $NbCr_2$ Laves phase since because it has the largest atomic free volume. Wei et al. [69] predicted the site occupancy behaviors of NbCr2-based C15 Laves phase with additional elements Ti, V, Mo and W and $Hf_{0.25}V_{0.6}Nb_{0.15}$ C15 Laves phases at finite temperature using sublattice model.

1.2.3 Ductile phase toughening

In order to further increase the room temperature toughness of Laves phases, many research results have shown that the ductile phase toughening is effective to prevent the brittle tendencies of Laves phases [47, 50, 71-77]. The two-phase alloys containing Laves phase and ductile toughening phase can be obtained in binary systems and ternary systems with additive element. For example, the Cr-12 at% Nb alloy has considerable compressive ductility at room temperature [78]. Li et al. [79] investigated the microstructure characterization and mechanical properties of arc-melted Cr-20% Nb. It was found that the Cr phase toughening and GB toughening is very effective to enhance the room temperature toughness of $NbCr_2$. Besides, the ductile phase can also be introduced by enough amount of alloying elements. Fujita et al. [80] found that the deformability of $NbCr_2$ Laves phase was enhanced by ductile BCC phase in Cr-Nb-Hf and Cr-Nb-Ta systems. Davidson et al. [81] found that the addition of Ti was more effective and the fracture toughness of the composites in ternary Cr-Nb-Ti system can reach 20 MPa√m. However, the volume fraction of Laves phase was too high to obtain

excellent high temperature properties [76]. For balancing the volume fraction of Laves phase and the fracture toughness of Cr-Nb-Ti alloys, Xue et al. [50] investigated several $NbCr_2$ based alloys, and it was found that the fracture toughness of the Cr_2Nb–20/30/40Ti alloys increased with increasing the Ti content both in the arc melting and heat treatment conditions.

Besides, some researchers have used powder metallurgy technologies to fabricate the $NbCr_2$ Laves phase, which can obtain a homogeneous microstructure and simultaneously refine grains [66, 82]. Rapid solidification [73], spark plasma sintering [83] and laser surface melting were also employed to overcome the disadvantages, like composition segregation, coarsening microstructure and other metallurgical defects, caused by the usual method, i.e., vacuum arc-melting or directional solidification [84].

1.3 Design of three-phase alloys based on refractory metals

Refractory metals are a class of metals with high melting points that are resistant to heat and wear and they are being used or studied for ultrahigh temperature applications such as hot parts of advanced gas turbines and jet engines. The definition of which elements belong to this group differs. The most common definition includes five elements: two of the fifth period (Nb and Mo) and three of the sixth period (Ta, W, Re). They all share some properties, including a melting point above 2000 ˚C and high hardness at room temperature. Besides, refractory metals are stable against creep deformation to very high temperatures due to the high melting points. While the wider definition includes a varying number of other additional elements: Ti, V, Cr, Zr, Hf, Ru, Rh, Os and Ir. Most of the crystal structure of the refractory metals is BCC and they have good room temperature toughness, especially Nb.

The ductile phase has often been used to enhance the room temperature fracture toughness of intermetallics, which have excellent high temperature strength and oxidation resistance, such as Laves phases. It has been suggested that fine-grained strengthening is one way to increase the room temperature ductility [59]. The larger the

volume fraction of ductile phase, the tougher the materials are at room temperature. However, the strength of the ductile phase, mainly BCC structure for refractory ductile phase, is not adequate at high temperature [76]. The mechanical properties of two-phase alloys are strongly dependent on the morphology, volume fraction and the orientation relationship (OR) of the second phase [85]. However, it is difficult to control the microstructure of two-phase alloys composed of Laves and ductile phases, especially in binary systems, because for almost all of the binary Laves systems, the dual phase is obtained by a eutectic reaction because many Laves phases are in equilibrium with the ductile BCC phase with a limited solid solubility, which is insufficient for the large volume fraction of Laves phase precipitation.

In order to overcome this trade-off relationship, a new BCC_1/BCC_2/Laves three-phase alloy is put forward. It is intended to introduce second BCC phase with a fine structure to bring the BCC_1/BCC_2 interfaces into the conventional single ductile phase. Similarly with Ni-based γ/γ' alloys [2, 86], high-temperature strength and creep resistance might be improved by the microstructure modification. In the meantime, AB_2 Laves phase dispersed in the BCC_1/BCC_2 two-phase microstructure. Hence, in this aspect, the BCC_1/BCC_2/Laves three-phase alloys with a complicated structure is proposed. Besides, good high-temperature strength, as well as high microstructure stability, can also be expected.

Nine refractory elements that most of them may be classed as relatively abundant refractory metals have been selected to design the three-phase alloy, their position in periodic table is shown in Fig. 17. The melting points of these elements are shown in Table 1.

It is known that the size factor plays an important role in the formation of Lave phase. Besides, the atomic radius is also vital for substitutional solid solutions according to Hume-Rothery rules.

The binary phase diagrams of each two elements are investigated [87] and there are three major types. They are defined as type I where continuous solid solution is

obtained; type II where a miscibility gap exists; and type III where intermetallic Laves phase forms, see Fig. 18. Based on the atomic radius, the types of the binary phase diagram of every two elements are listed in Table 2. It is found that the atomic ratio r_A/r_B ($r_A>r_B$) for type I is 1.01~1.09, for type II is 1.06~1.10, and for type III is 1.09~1.26. The relationship between the types of the binary phase diagram and atomic ratio is shown in Fig. 19.

As the three-phase alloy consist of two BCC phases and Laves phase, type II and type III is necessary to design the alloy in a ternary system. There are three combinations from two out of three elements. For the rest combination, type I and type II are both feasible. According to Table 2, just several ternary systems are possible to obtain three-phase alloy, such as Cr-Mo-Nb, Cr-Nb-W and Cr-Ti-W.

To control the microstructure and avoid the aggregation of Laves phase, the Cr-Mo-Nb ternary system is selected to study the three-phase alloy. The existing two BCC phases provides higher strength than the singe BCC phase and a fine and stable structure can be obtained at high temperature by adjusting the lattice mismatch between the two BCC phases. The fine structure can restrain the growth of Laves phase and prohibit the crack propagation in Laves phase, thus improve the toughness of the alloy at low temperature. In this study, the isothermal sections of the ternary phase diagrams in Cr-Mo-Nb were investigated. The Lave phase precipitation behavior was studied in both Laves/BCC two-phase alloy and BCC_1/BCC_2/Laves three-phase alloy. The microstructure evolution of the three-phase alloy was observed and room temperature mechanical properties were evaluated. The effect of Si on the stability of Laves phase was also investigated.

Table 1 melting temperature of the selected elements

Element	Cr	V	Mo	W	Nb	Ta	Ti	Hf	Zr
M.T./°C	1860	1887	2617	3410	2468	2996	1660	2230	1852

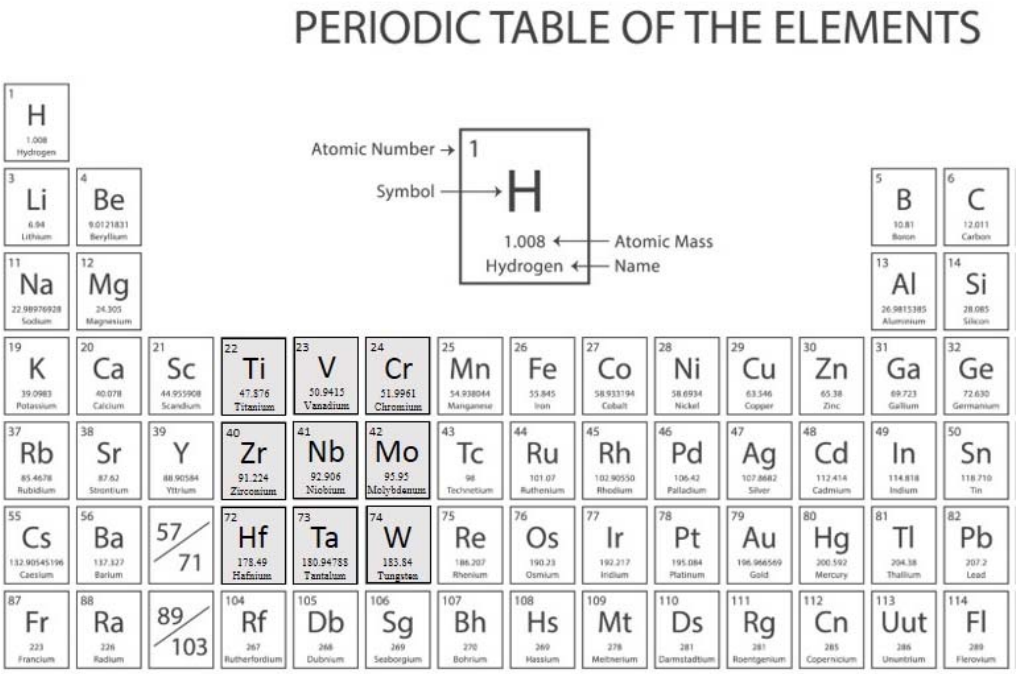

Fig. 17. Selected elements (with gray background) in the periodic table.

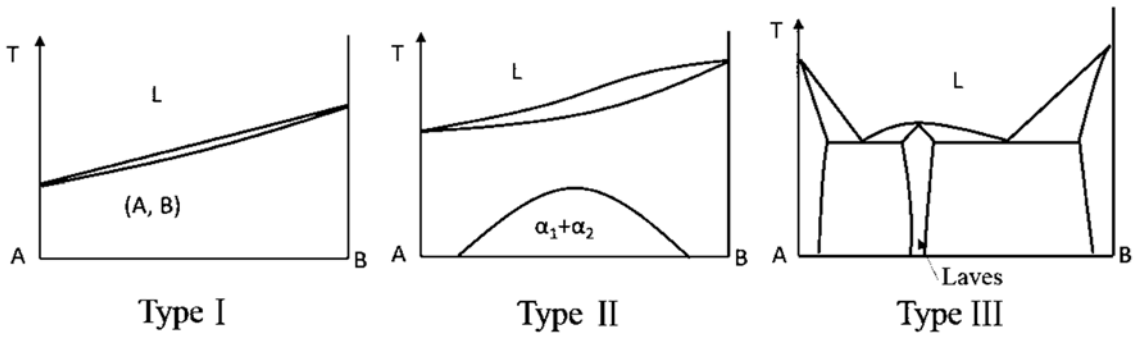

Fig. 18. Three types of the binary phase diagram.

Table 2 type of binary phase diagram of every two elements

Element	Cr	V	Mo	W	Nb	Ta	Ti	Hf	Zr
Cr		I	II	II	III	III	III	III	III
V	I		I	I	I	III	II	III	III
Mo	II	I		I	I	I	II	III	III
W	II	I	I		I	I	II	III	III
Nb	III	I	I	I		I	I	I	II
Ta	III	III	I	I	I		I	II	II
Ti	III	II	II	II	I	I		I	I
Hf	III	III	III	III	I	II	I		I
Zr	III	III	III	III	II	II	I	I	
Atomic Radius (r/nm)	0.125	0.131	0.136	0.137	0.143	0.143	0.143	0.156	0.156

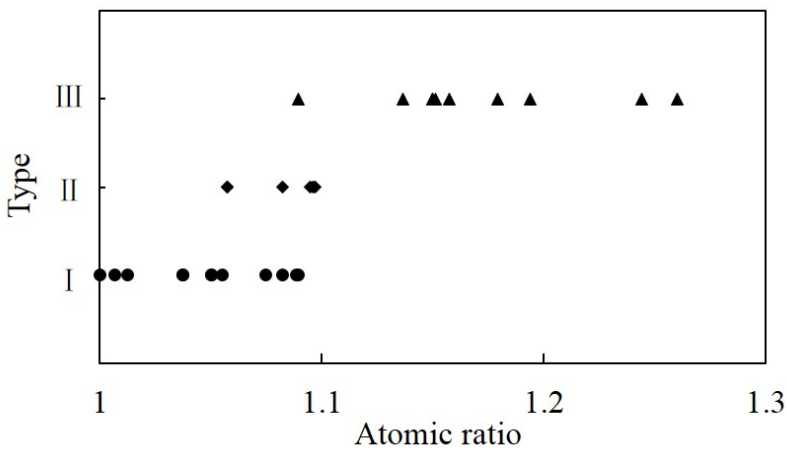

Fig. 19. Type of the binary phase diagram vs. atomic ratio.

Chapter 2

Experimental procedures

This chapter aims to provide the detailed experimental procedures carried out in this thesis from the composition design and alloy preparation to the microstructure analysis and mechanical tests.

2.1 Arc melting

All the alloys investigated in this study were prepared by NEV-AD03 arc melting furnace with a MRHP-300 (9-1) TIG welding power supply under an argon atmosphere. The purities of the raw materials (The Nilaco Corporation) were 99.9 wt% Nb, 99.99 wt% Cr, and 99.95 wt% Mo, respectively. 99.9 wt% Si was also employed to study the effect of Si on the stability of Laves phase.

The chamber was vacuumed under a vacuum degree of 5×10^{-5} Pa before the high-purity argon (99.99%) was introduced into the chamber using a diffusion pump. Pure Ti and raw materials were both put in the melting chamber. Pure Ti was melting for three time before melting the raw materials to absorb possible oxygen, and the pure Ti was melted once after using the rotating arm. The button ingots (ca. 7g) were tuned over and melted more than ten times on a water-cooled copper hearth to ensure chemical homogeneity.

2.2 Heat treatment

The arc-melted alloys were cut and sealed in quartz tubes using ULVAC VPC-051A vacuum pump with a vacuum degree under 2×10^{-4} Pa and aged in different temperature conditions followed by water quenching or furnace cooling for phase equilibrium studies.

In order to investigate the precipitation behavior of Laves phase in the supersaturated BCC matrix phase, solution treatment for alloys was performed in a high-frequency induction furnace (NEV-MO3C) at 1973 K, because the quartz tubes

cannot stand in temperatures higher than 1793 K. The sample was placed inside the graphite crucible, the layout is shown in Fig. 20. Then the solution treated samples were aged at 1473 K and other temperatures.

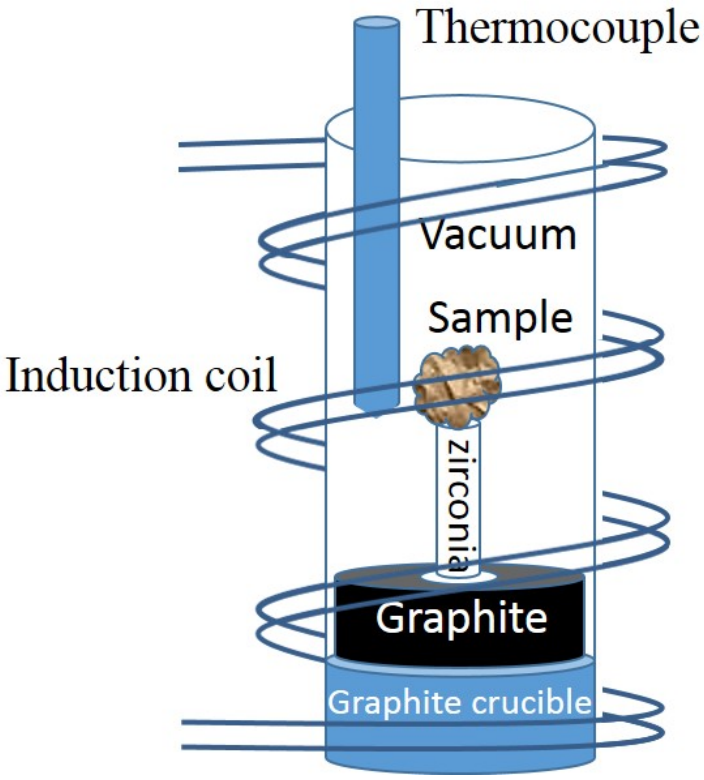

Fig. 20. Layout inside the induction furnace

.

2.3 Microstructure observation and crystal structure analysis

2.3.1 XRD

X-ray diffraction (XRD) (PANalytical X'Pert PRO, Cu Kα) with 2θ scans from 30° to 80° were also performed on the as-cast and heat treated samples to identify the crystal structures of the constituent phases at a current of 40 mA and a voltage of 40 kV. Jade 6.0 software was used to analyze the XRD pattern. The lattice parameters of C15 Laves phase and the BCC phase was calculated by extrapolation method.

2.3.2 SEM

The microstructure was observed using field emission scanning electron microscope (FE-SEM, JEOL JXA-8530F) equipped with an electron probe micro-analyzer. Wavelength dispersive spectroscopy (WDS) was employed to determine the average composition of the alloys with a large spot size of ca. 20 μm and the composition of constituent phases. An electron backscatter diffraction (EBSD) system attached in scanning electron microscope (SEM, JEOL JAMP-9500F) was used to investigate the orientation relationship between C15 Laves phase and the BCC matrix phase.

2.3.3 TEM

After two-stage heat treatment, the structure of the three-phase alloy is too fine to distinguish by SEM, transmission electron microscopy (TEM, JEOL JEM-2010) was employed to investigate the microstructure of the three-phase alloys heat treated at different conditions. The alloys were fabricated by (focused ion beam) FIB (JEOL JIB-4601F). Selected area diffraction (SAED) method was employed to determine the crystal structures of the constituent phases. Energy dispersive spectroscopy (EDS) in TEM was used to examine the composition of each phase.

2.4 Mechanical tests

2.4.1 Vickers hardness tests

The strength of the alloys heat-treated at different conditions is evaluated by mico hardness tester (type M, Shimadzu Seidakusho LTD.) under a load of 0.5kgf with a holding time of 30 s at room temperature.

2.4.2 Nanoindentation tests

Nanoindentation test (Hysitron TI 950) is also conducted on the sample polished by cross-section polisher (JEOL SM-09010) to assess the hardness of the constituent phases under the load of 4000 μN at room temperature. Fifty tests were conducted in a grid automatically, then combining with SEM, the hardness of each phase was evaluated.

2.4.3 Compression tests

Parallelepiped compression samples with a dimension of 3 × 3 × 6 mm were cut from the aged buttons by a wheel cutter and mirror-polished. Compression tests with an initial strain rate of 1×10^{-4} s^{-1} were conducted by Instron 5584 tester at room temperature.

Chapter 3

Laves phase precipitation behavior

The introduction of a ductile phase into Laves phase-based materials is attractive to obtain a two-phase alloy, which may preferably balance the strength and fracture toughness, in both binary and ternary systems [50]. The mechanical properties of two-phase alloys are strongly dependent on the morphology, volume fraction and the OR of the second phase [85]. However, it is difficult to control the microstructure of two-phase alloys composed of Laves and ductile phases, there are few works related to details on the precipitation behavior of Laves phase from a supersaturated ternary solid solution. Laves phases sometimes precipitate from the BCC phase, as with the Cr/$NbCr_2$ alloys [78, 88], and sometimes just precipitate along the GBs, for example, in the Nb-20W-10Cr alloy [89].

This chapter aims to understand the Laves phase precipitation behavior in the BCC phase. Based on the isothermal section of Nb-Mo-Cr ternary phase diagram [92], the binary phase diagrams are also shown in Fig. 21, four alloys with different compositions were prepared (Table 3) , which have different equilibrium BCC matrix compositions with $NbCr_2$ precipitates after annealing at 1473 K. The Laves precipitation behavior was investigated and the OR between the Laves and BCC phases was examined.

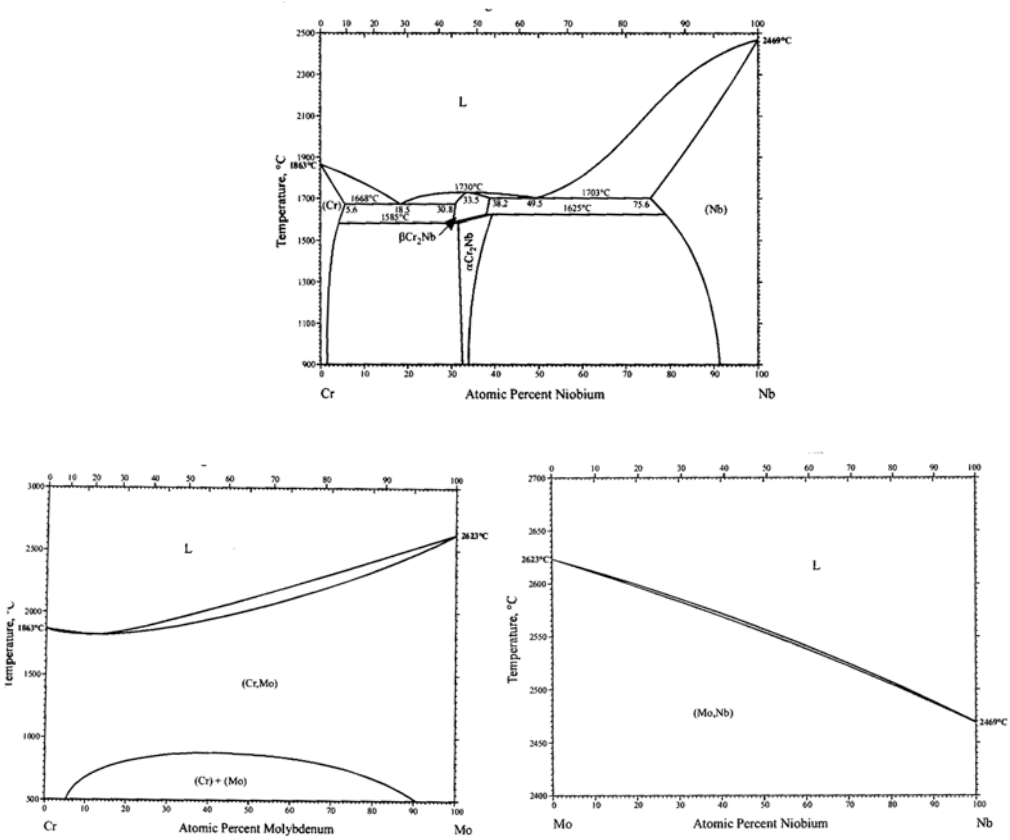

Fig. 21. The binary phase diagram of Cr-Nb, Cr-Mo and Mo-Nb [87].

Table 3 Nominal compositions of alloys for isothermal section study (at%).

No.	Cr	Mo	Nb
#1	42	31	27
#2	50	30	20
#3	74	16	10
#4	62	18	20

3.1 Isothermal section ternary phase diagram

Fig. 22 shows an SEM image and XRD pattern of alloy #2 heat-treated at 1473 K for 168 h. The XRD pattern confirmed that the alloy consists of Cr-rich BCC_1 phase, Mo-rich BCC_2 phase, and C15 Laves phase $NbCr_2$ at 1473 K. Based on the WDS results (Table 4), the bright phase (B) is the Mo-rich BCC_2 phase, the gray phase (C) is the Laves phase and the dark particles (A) are the Cr-rich BCC_1 phase in Fig. 22(a). On the other hand, after the heat treatment at 1773 K, two-phase equilibrium (BCC and Laves phase) is observed in alloy #2 and #4, as shown in Fig. 23.

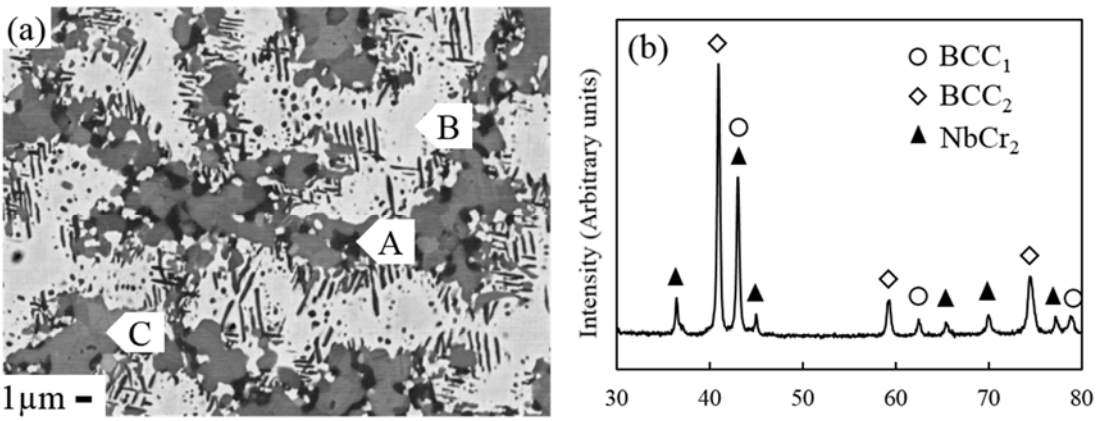

Fig. 22. (a) Microstructure and (b) XRD pattern of alloy #2 heat-treated at 1473 K for 168 h.

Table 4 WDS results for each phase in alloy #2 at 1473 K, plotted in Fig. 22(a) (at%).

	Cr	Mo	Nb	Phase constituent
A	71.9	19.5	8.6	Cr-rich BCC_1
B	31.9	47.0	21.1	Mo-rich BCC_2
C	63.8	9.1	27.1	$NbCr_2$

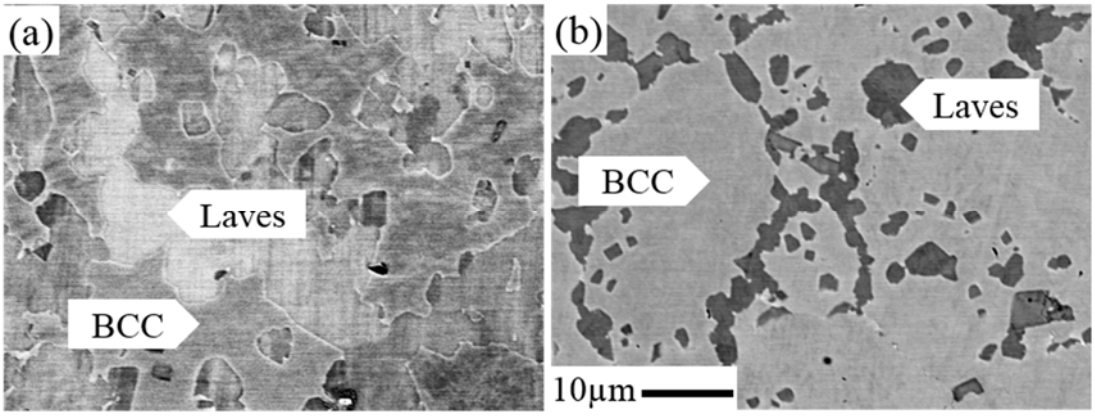

Fig. 23. SEM images of alloys (a) #4 and (b) #2 heat-treated at 1773 K for 24 h.

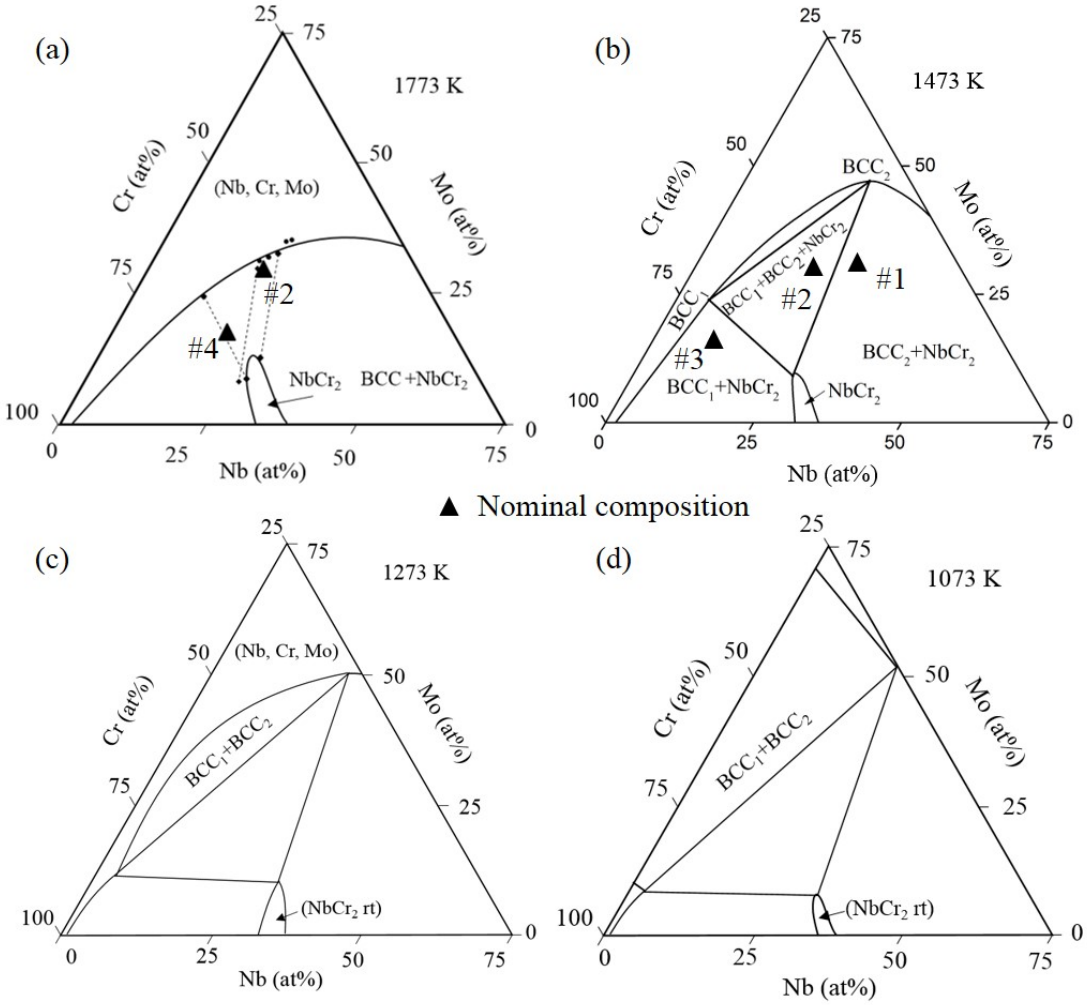

Fig. 24. Cr-rich corner of Cr-Mo-Nb isothermal sections at (a) 1773 K, (b) 1473 K, (c) 1273 K [90] and (d) 1073 K (speculated).

Fig. 24 shows isothermal sections of the Cr-rich corner of the Cr-Mo-Nb ternary system at different temperatures [90]. As the temperature is too high for BCC decomposition, no three-phase region is observed at 1773 K, and a BCC/$NbCr_2$ two-phase region surrounds the $NbCr_2$ Laves phase (Fig. 24(a)). The $NbCr_2$ single-phase field extends in a certain direction, which indicates Mo atoms mainly occupy Nb-sites [64] and Mo solubility in the $NbCr_2$ Laves phase at 1773 K is 13%, which is higher than the 9 at.% observed at 1473 K.

A three-phase region appears at 1473 K, and the area of the region seems to spread at 1273 K when compared to the early work of Svechnikov and Kobzenko [90]. Wang et al. [91] evaluated the parameters for thermodynamic calculation of the Cr-Mo-Nb phase diagram including BCC phase decomposition. According to the results, the decomposition of the BCC phase in the Cr-Mo system was enhanced by the addition of Nb; therefore, the BCC_1 and BCC_2 two-phase region, in which no BCC decomposition appears at the Cr-Mo binary edge where a continuous solid solution region emerges, exists at 1273 K and 1473 K. At a relatively lower temperature of 1070 K, it is speculated that the ternary phase diagram exhibits the BCC_1 and BCC_2 two-phase region, which spreads and contacts the Cr-Mo binary edge because there is a two-phase decomposition region in the Cr-Mo binary system at 1070 K (Fig. 24(d)).

Fig. 25 shows isothermal sections of the Cr-rich corner of the Cr-Mo-Nb ternary system at 1473 K. Zakharova and Prokoshkin [92] reported the isothermal section of the Cr-Mo-Nb ternary system at 1473 K, as shown in Fig. 25(a). The composition of each phase in the three-phase region was mainly determined by coupling XRD results and composition of alloys investigated. The Cr-rich BCC_1 phase has almost the same composition with the present result shown in Fig. 25(b), however, the composition of the Mo-rich BCC_2 phase is far different from the that of the present work which is determined on the basis of the WDS results. Each alloy is also plotted with a triangle in Fig. 25(b). It should also be noted that according to the ternary phase diagram reported by Zakharova and Prokoshkin [92] alloy #1 is in the three-phase region. However, it is

in BCC-Laves two-phase region as will be discussed in the following sections.

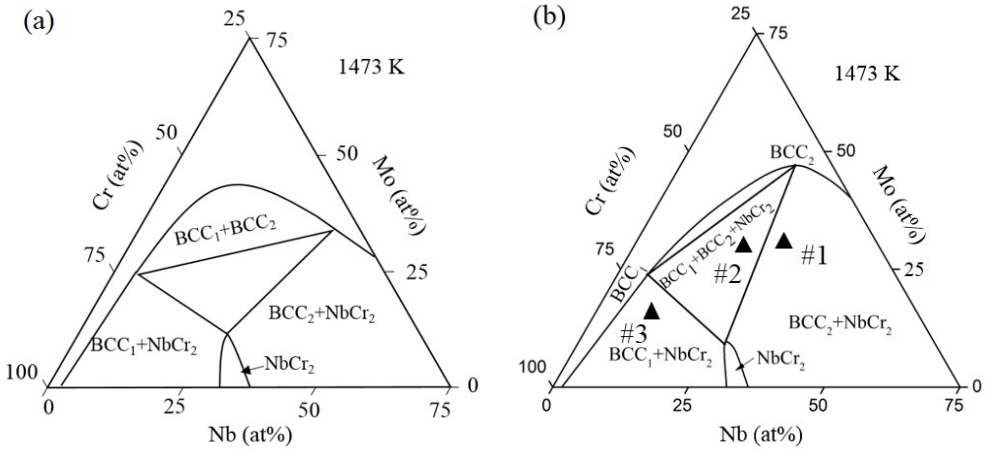

Fig. 25. Cr-rich corner of Cr-Mo-Nb isothermal sections at 1473 K. (a) reported by Zakharova and Prokoshkin [92]. (b) present work.

3.2 Microstructure after two-stage heat-treatment

Homogenous structures were obtained for three alloys (#1-3) at 1973 K, as shown in Fig. 26(a,c,g), which was determined to be single BCC phase, according to the XRD results in Fig. 27. It is not hard to understand that the solubility of BCC phase increases due to the higher temperature. For alloy #3, it should be noted that a limited amount of Laves phase precipitated along the GBs, which may occur during cooling. The lamellar structure is also formed through discontinuous precipitation in Cr-20Ti alloy at 1668 K [93], while it is in the single BCC phase region according to the Cr-Ti binary phase diagram. It strongly suggests that the discontinuous precipitation of Laves phase is quite fast.

After subsequent annealing at 1473 K, each of the three alloys had different precipitation morphologies, as shown in Fig. 26(b,d,e,f,h). Gray precipitates appear at the GBs and cellular structures are formed in alloy #1, while precipitates appear not only at the GBs but also in the grain interior in alloy #3 in which the needle-like precipitates tend to grow in certain directions. The precipitates in both alloys were confirmed to be Laves phases from the XRD patterns shown in Fig. 27. In alloy #2, BCC phase decomposes into two BCC phases (BCC_1 and BCC_2) during 12 h heat-treatment (Fig. 26(d) and Fig. 27(b)) in a manner of a lamellar-like structure, then blocky gray Laves phase appears in sample heat-treated for 100 h (Fig. 26(e,f) and Fig. 27(b)). It is noteworthy that the Laves phase in alloy #2 seems to be surrounded by bright BCC_2 phase. These microstructures of alloys are consistent with the 1473 K isothermal section (Fig. 24(b)) proposed in the present study.

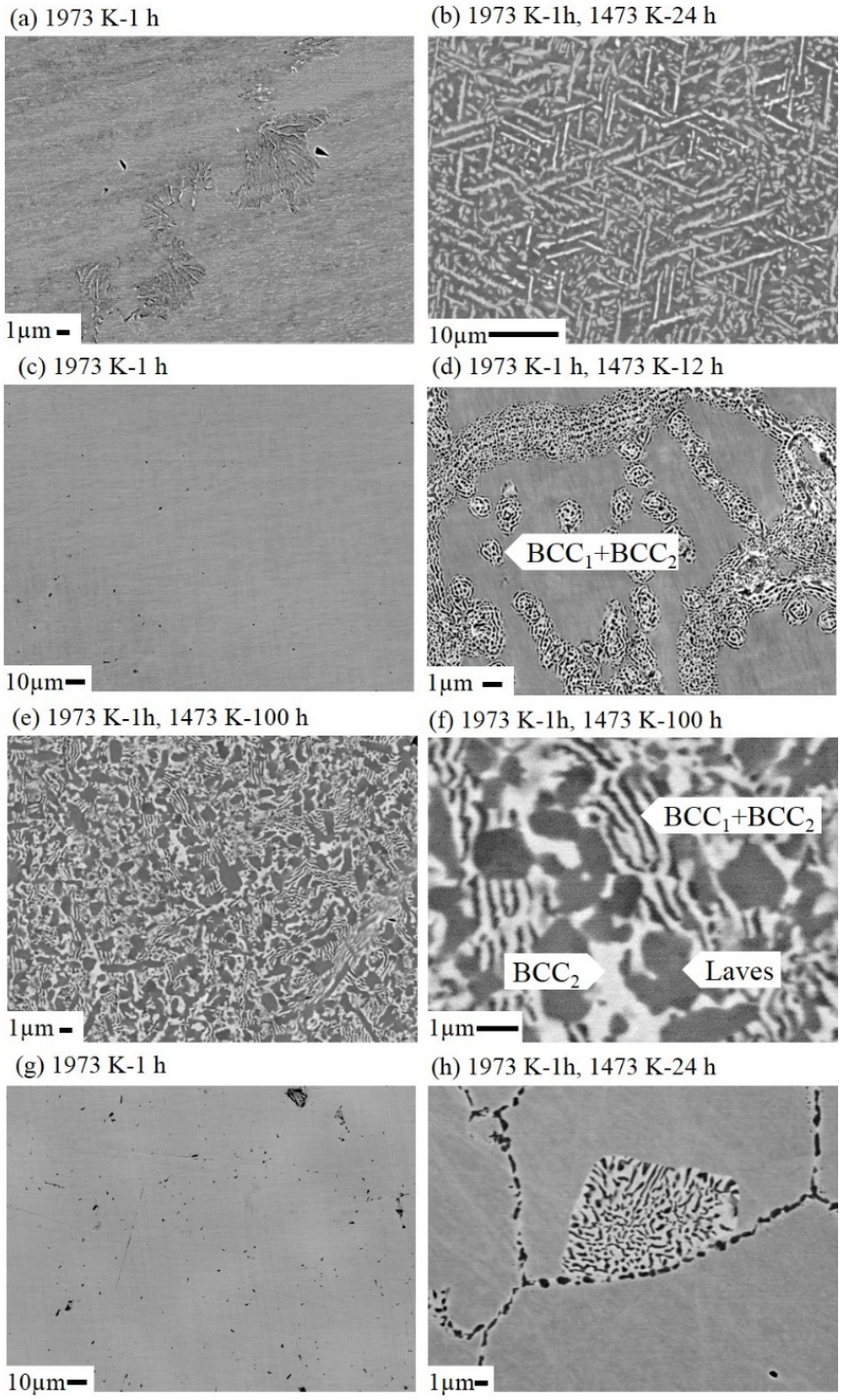

Fig. 26. Microstructure of alloy #3 (a,b), alloy #2 (c-f), and alloy #1 (g,h) heat-treated at different conditions.

(a), (c) and (g): solution-treated at 1973 K for 1 h.

(b), (d), (e), (f) and (h): heat-treated at 1473 K for various duration after the solution treatment.

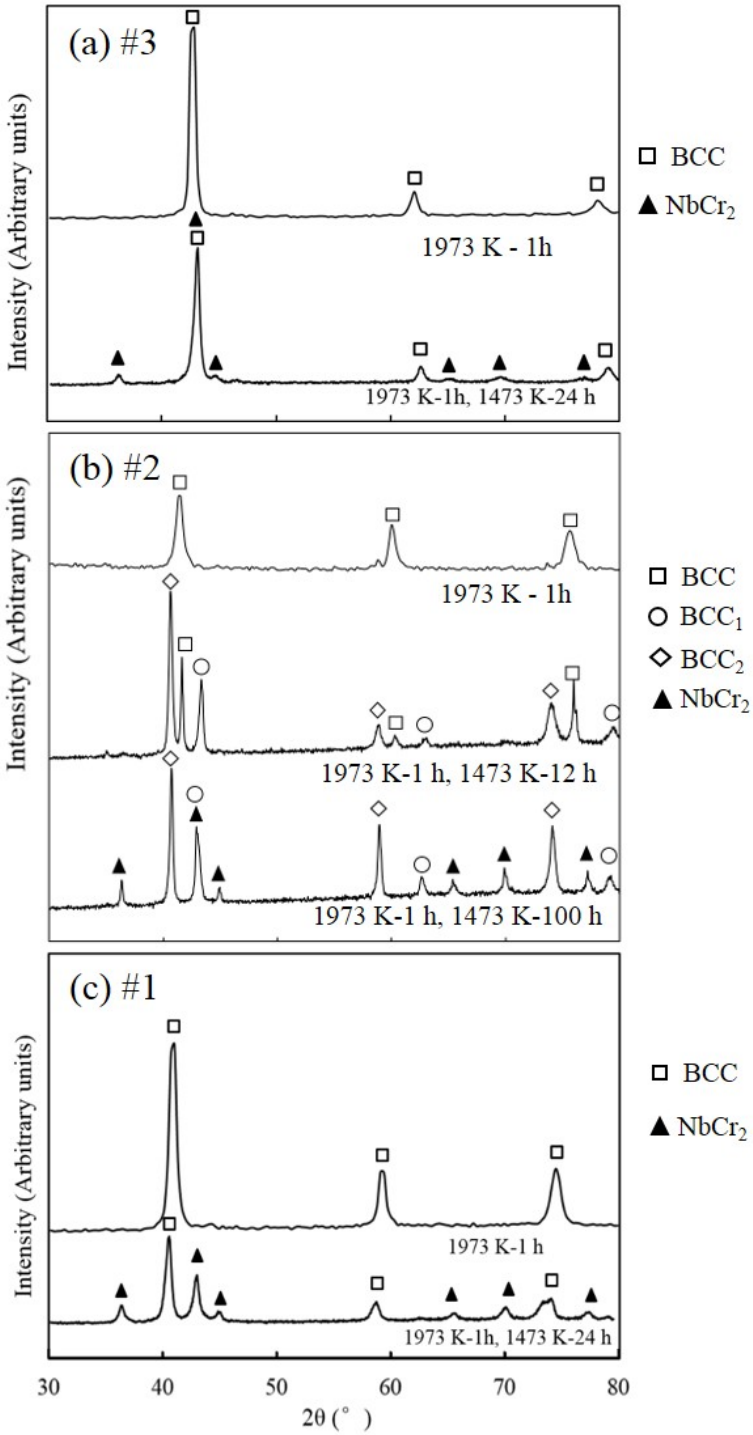

Fig. 27. XRD patterns corresponding to the alloys in Fig. 26.

3.3 Orientation relationship between Laves phase and the BCC matrix

Lots of research has been conducted to examine the crystallographic orientation relationship (OR) between Laves phase and BCC phase in refractory systems, such as in Cr-$NbCr_2$ [88], Cr-$TaCr_2$ [94], and Cr-Nb-Ti [95] systems. Nevertheless, there have been few reports on effect of alloy compositions on the crystallographic OR between $NbCr_2$ Laves precipitates and BCC phases with different alloy compositions. In this study, EBSD was adopted instead of TEM to further understand the precipitation behavior in alloys #3 and #2 because EBSD enables the crystallographic OR between many Laves precipitates and BCC matrix phase to be simultaneously examined over a wide area (approximately several tens of square micrometers).

Fig. 28 shows an SEM image, phase map, corresponding inverse pole figure (IPF) maps, and pole figures (PF) for C15 #3-1&#3-2 of alloy #3. Compared to the $\{011\}_{BCC}$ plane traces shown in Fig. 28(c), the interphase boundaries between the BCC and Laves phases appears to be on the $\{011\}_{BCC}$ plane, which indicates that the habit plane of needle-like precipitates (Fig. 26(b)) in alloy #3 is $\{011\}_{BCC}$ plane. Twinning has been widely reported in C15 Laves phases such as $NbCr_2$ [88], $TiCr_2$ [93], and HfV_2 [96]. In this study, twinning was also observed in C15 $NbCr_2$ Laves phases, as shown in Fig. 28(e), where C15 #3-1&#3-2 share a common (111) twinning plane as a twin pair. Pope and Chu [97] suggested annealing twins of the type $\{111\}\langle 112\rangle$ formed in C15 HfV_2, while some other researchers have proposed that twinning is generated by a C14/C15 phase transformation [88]. Besides, Deformation twinning has also been seen in HfV_2 [57, 58, 98] and $NbCr_2$ [54, 99] via synchroshear mechanism [58].

In the present study, the twinning is more likely to be annealing twins formed during the heat treatment at 1473 K because the C14/C15 transformation temperature is as high as 1860 K for the $NbCr_2$ Laves phase in the Cr-Nb system. Although the stability of C15 $NbCr_2$ is decreased by Mo addition [49], the solubility of Mo in $NbCr_2$ is not high enough to dramatically change the C14/C15 transformation temperature to as low as 1473 K. No C14 peaks were observed in the XRD examination for alloys

heat-treated at 1473 K, as shown in Fig. 27. Takasugi and Yoshida [53] reported only C15 phases and no C14 phase in the Cr-Mo-Nb ternary system after annealing at 1673 K.

Fig. 29 shows pole figures (PFs) of the BCC matrix and C15 #3-1 marked in Fig. 28(d). Based on the former study [87] and the close packed {111} plane of C15, two types of ORs between C15 #3-1 and BCC are identified as:

$$\text{OR 1: } (011)_{BCC} \,//\, (11\bar{1})_{C15},\ [0\bar{1}1]_{BCC} \,//\, [\bar{1}10]_{C15}$$

$$\text{OR 2: } (\bar{4}11)_{BCC} \,//\, (111)_{C15},\ [0\bar{1}1]_{BCC} \,//\, [\bar{1}10]_{C15}.$$

OR 1 between C15 precipitates and the BCC matrix was also reported in the Cr-Hf [77], Cr-Nb [88], and Cr-Ti [93] systems. This also explains the preferred growth directions of C15 (see Fig. 28) which has an interfacial boundary along the $\{011\}_{BCC}$ plane traces, and which may be caused by the lower interfacial energy. The $(11\bar{1})_{C15}$ plane in OR 1 is a twinning plane with C15 #3-2; therefore, it is not surprising that OR 1 is found between C15 #3-2 and the BCC matrix. Interestingly, OR 2 is also confirmed between C15 #3-2 and the BCC matrix, as shown in Fig. 30. However, Fig. 31 shows there is only OR 1 between C15 #3-3 and BCC, while OR 2 is not found. The same examination of OR has also been adopted for C15 #3-4, #3-5, and #3-6. The results are summarized in Table 5. C15 #3-5 and C15 #3-6 show the same ORs with the C15 #3-1&#3-2 twin pair, while C15 #3-3 and C15 #3-4 have only OR 1 but no OR 2. All these precipitates always exhibit OR 1, which indicates the principal OR between C15 precipitates and the BCC matrix should be OR 1, which has been suggested in many BCC-C15 systems [77, 88, 93]. However, OR 2 appears occasionally in the twins.

Fig. 32 shows schematic drawings of the OR between the C15 Laves and BCC phases in the case of the C15 #3-1&#3-2 pair. The angles between the $\{111\}_{C15}$ planes is 70.5°, and the angles between $(411)_{BCC}$ and $(011)_{BCC}$, and between $(\bar{4}11)_{BCC}$ and $(011)_{BCC}$ are also 70.5°, as shown by the side views in Fig. 32. Thus, once OR 2 $(\bar{4}11)_{BCC} \,//\, (111)_{C15}$ exists in the parent grain, it can also be found in the twinned part of the precipitate. This is the reason why both parts of the twin pairs exhibit both OR 1

and OR 2.

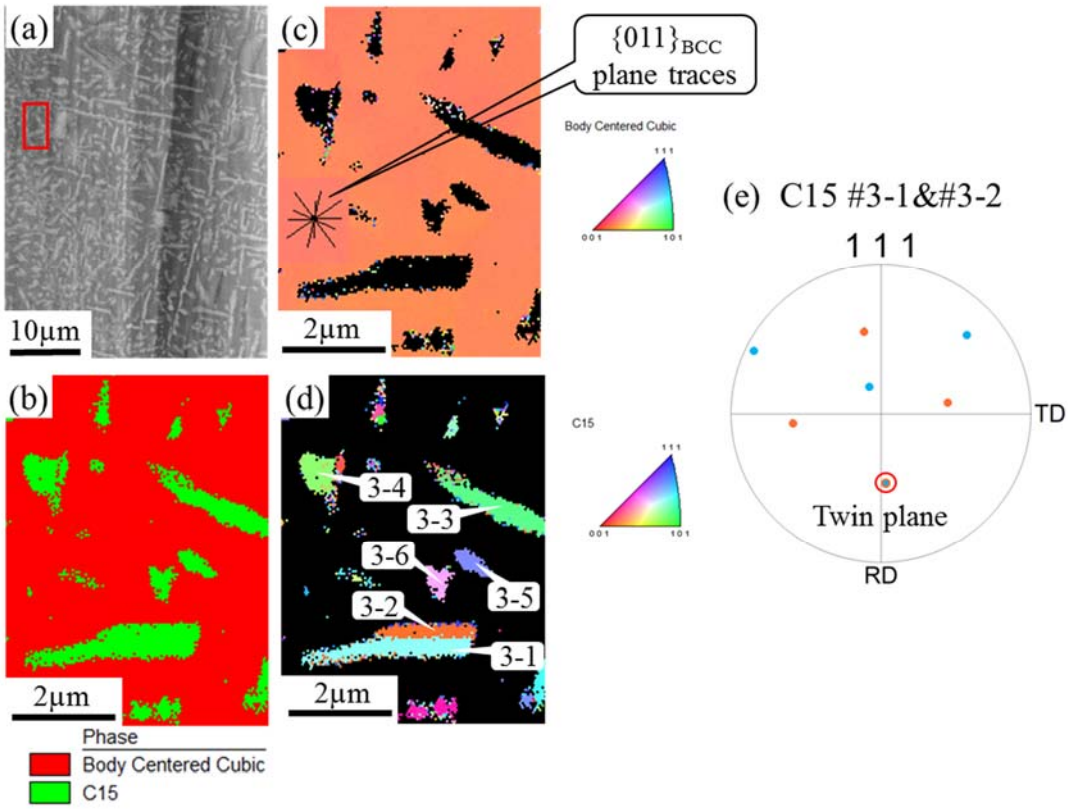

Fig. 28. The results of EBSD analysis of alloy #3 after two-step heat-treatment obtained corresponding to the red box in (a) SEM image. (b) phase map, IPF maps of (c) BCC phase and (with $\{011\}_{BCC}$ plane traces) (d) C15 Laves phases, and PF of (e) C15 #3-1&#3-2 (twin plane is marked by a red circle). Colors for <111> poles correspond to the color in (d).

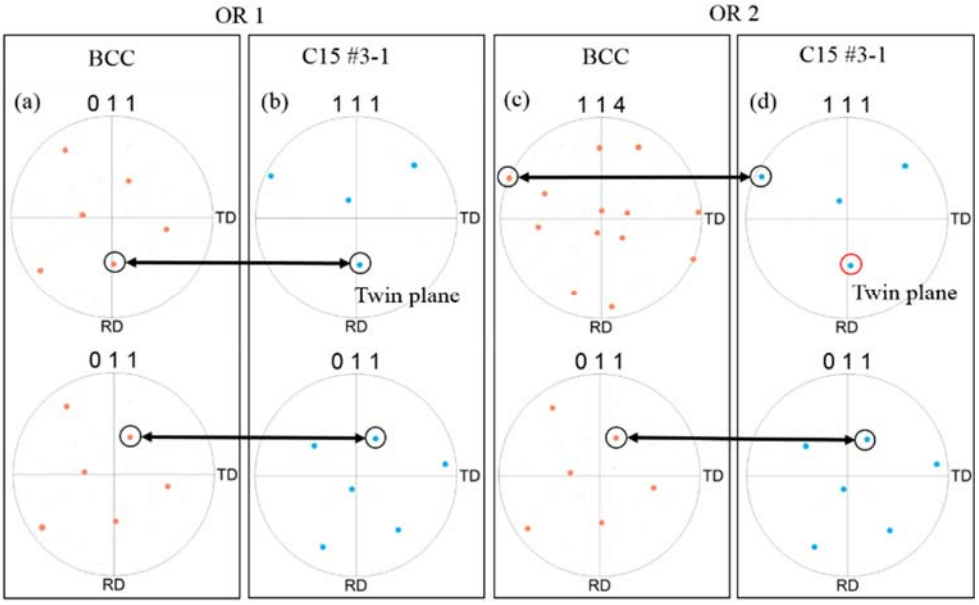

Fig. 29. PFs for (a,c) the BCC matrix and (b,d) C15 #3-1 indicated in Fig. 28(d).

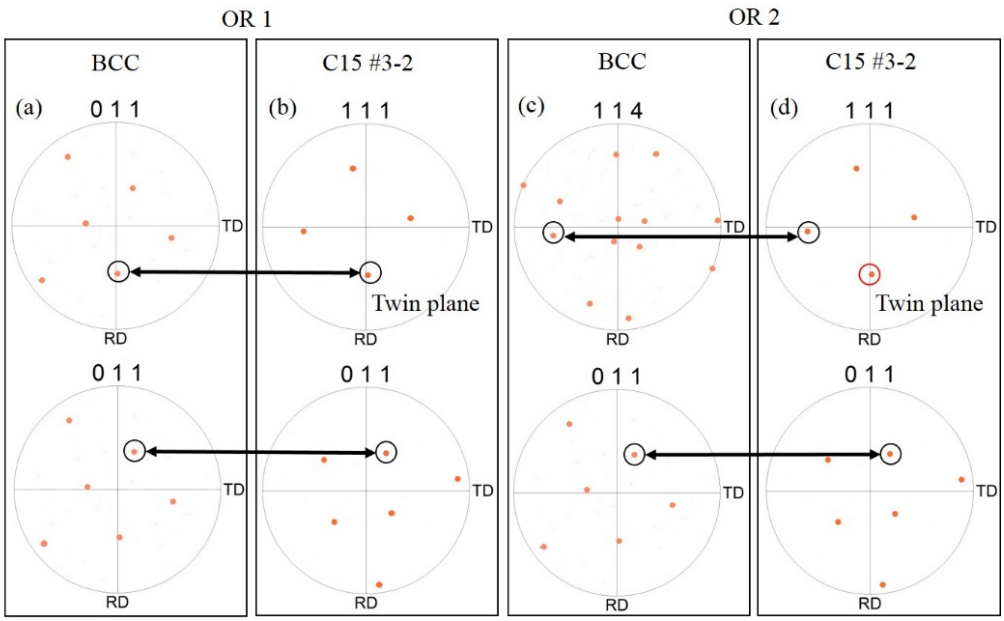

Fig. 30. PFs for (a,c) the BCC matrix and (b,d) C15 #3-2 in Fig. 28(d).

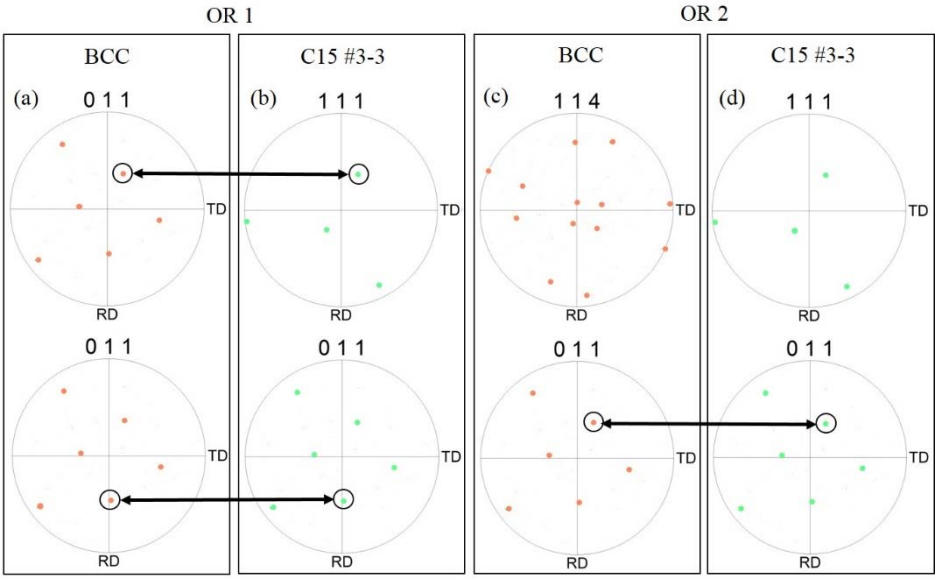

Fig. 31. PFs for (a,c) the BCC matrix and (b,d) C15 #3-3 in Fig. 28(d).

Table 5 OR for grains marked in Fig. 28(d).

C15	OR 1	Involving $(111)_{C15}$ as twin plane	OR 2	Involving $(111)_{C15}$ as twin plane
#3-1	Yes	Yes	Yes	No
#3-2	Yes	Yes	Yes	No
#3-3	Yes	---	No	---
#3-4	Yes	---	No	---
#3-5	Yes	---	Yes	---
#3-6	Yes	---	Yes	---

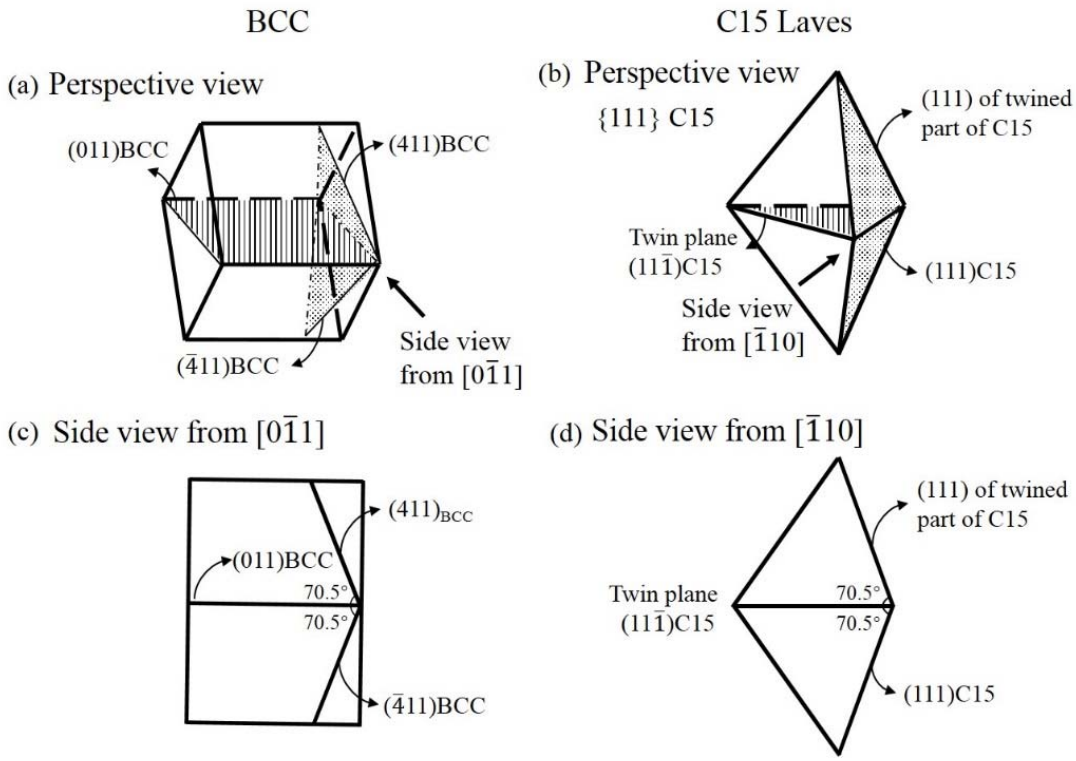

Fig. 32. Schematic diagrams showing the crystallographic OR between the C15 precipitate and BCC phase when the twins hold both OR 1 and OR 2 in alloy #3. (a) Perspective view of the BCC unit cell, (b) perspective view of $\{111\}_{C15}$ tetrahedrons after twinning, (c) side view of BCC indicated in (a), and (d) side view of C15 indicated in (b).

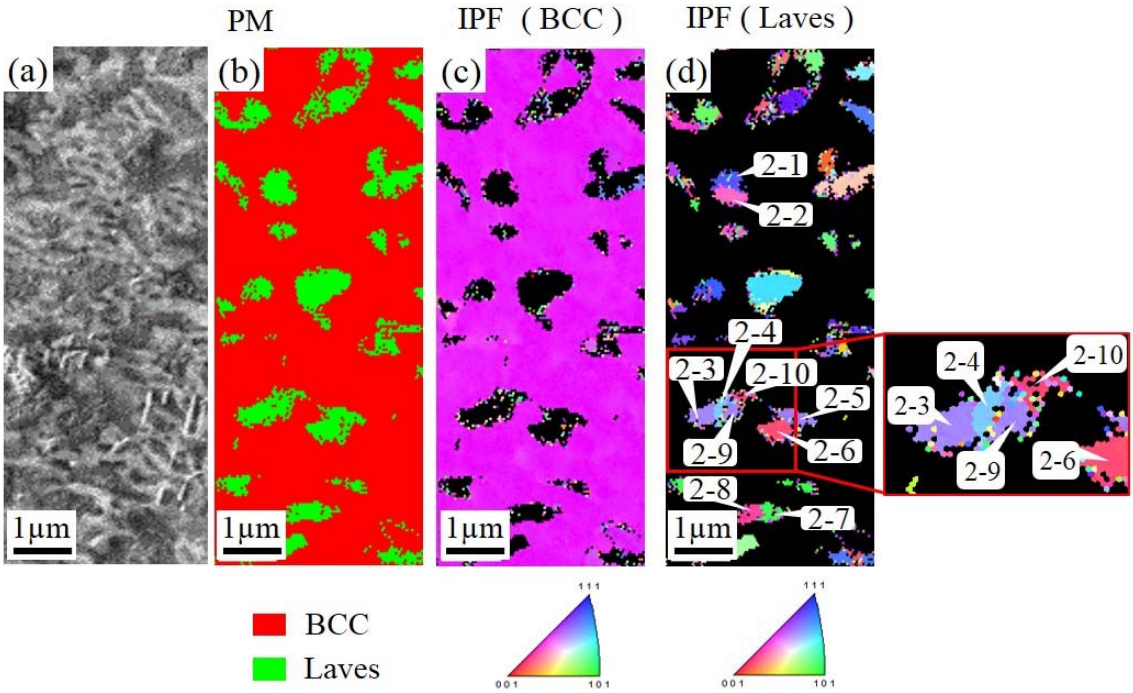

Fig. 33. (a) SEM images and EBSD analysis results of alloy #2 aged at 1473 K for 100 h: (b) phase map and IPF maps of (c) BCC and (d) Laves phase.

Fig. 33 shows orientation maps for alloy #2 annealed at 1473 K for 100 h after homogenization. C15 #2-1&#2-2, C15 #2-3&#2-4, C15 #2-5&#2-6, C15 #2-7&#2-8 and C15 #2-9&#2-10 share a common (111) plane, as shown in Fig. 34. C15 #2-3, #2-4, #2-9, and #2-10 are considered to precipitate as one grain, and then divide into four parts. Each part has twin relationships, but the twin planes are not identical. Therefore, this strongly suggests that the twins are not transformation twins but annealing twins. OR 1 and OR 2 are also found in C15 #2-1 (Fig. 35); however, only OR 2 exists for the counter part of the twin grain, i.e., C15 #2-2 (Fig. 36). $(111)_{C15}$ in OR 2 is identified as a twin plane. The twinning plane tends to be involved in OR 2 for alloy #2, while it tends to be involved in OR 1 for alloy #3. For the C15 #2-3&#2-4 pair, OR 3: $(011)_{BCC}$ // $(111)_{C15}$, $[\bar{1}\bar{1}1]_{BCC}$ // $[01\bar{1}]_{C15}$ is identified between BCC and C15 #2-3, while neither OR 1 nor OR 2 appear, as shown in Fig. 37, and there is no fixed OR between the BCC matrix and C15 #2-4 (Fig. 38). In this case, C15 #2-3 should be the parent grain and OR 3 should be the principal OR. Bhowmik et al. [94] have also found an OR which is similar with OR 3, just the $<111>_{BCC}$ and $<110>_{C15}$ are within a few degrees of each other in Cr matrix and cubic Cr_2Ta. The same examination is employed to deal with the other twin pairs, and the results are summarized in Table 6. C15 #2-7&#2-8 share the same OR with that found in C15 #2-1&#2-2, while C15 #2-5&#2-6 and C15 #2-9&#2-10 have the same OR as that found in C15 #2-3&#2-4. No OR 3 was identified in alloy #3 in any combination of Laves phase and BCC matrix.

Fig. 39 shows schematic drawings of the OR between C15 Laves and the BCC matrix phase in the case of the C15 #2-1&#2-2 pair or the C15 #2-7&#2-8 pair, where OR 2 is found in both grains of the twin pairs, while OR 1 appears in only one of the grains of the twin pairs in alloy #2. This strongly suggests that OR 2 governs the precipitation of Laves phase from BCC, i.e., the twin part of the grain is selected to have another OR 2. From this point of view, alloy #2 has two principal ORs, OR 2 and OR 3.

As discussed above, the twin $(111)_{C15}$ plane is parallel to the $(-411)_{BCC}$ plane in

OR 2. The angle between the $\{111\}_{C15}$ planes is 70.5°, while there is only one $(011)_{BCC}$ plane the angle between $(-411)_{BCC}$ and which is also 70.5°. Thus OR 1 just occasionally appears in one of the grains of the pair.

The lattice misfit of the C15 precipitate and BCC matrix strongly affects the selection of the OR between the two phases. The lattice misfit (δ) between two planes of matrix (α) and precipitate (P) can be estimated with the planar disregistry proposed by Bramfitt [100] as:

$$\delta_{(hkl)_P}^{(hkl)_\alpha} = \sum_{i=1}^{3} \frac{\left|(d_{[uvw]_\alpha^i} \cos\theta) - d_{[uvw]_P^i}\right|}{3d_{[uvw]_P^i}} \times 100 \qquad (1),$$

where $(hkl)_i$ are the low-index planes of the BCC matrix and C15 precipitate. $[uvw]_i$ are the low-index directions in $(hkl)_i$. $d_{[uvw]_i}$ are the interatomic spacing along $[uvw]_i$. θ is the angle between the $[uvw]_\alpha$ and $[uvw]_P$. Presuming that the thermal expansion has a linear relationship for any phases with temperature in the range from room temperature to 1473 K, the lattice constants of the BCC matrix and C15 $NbCr_2$ at 1473 K are calculated based on the room temperature lattice constants obtained from the present XRD results. The planar disregistry was then deduced using the lattice constants at 1473 K. The coefficients of thermal expansion for Cr, Mo, and Nb are 11×10^{-6} /K, 5.5×10^{-6} /K, and 8×10^{-6} /K, respectively [101]. Considering the high solid solution and different composition of each BCC phase, 10×10^{-6} /K was employed as the thermal expansion coefficient for approximation. The lattice constants of another two solid solution alloys, Cr-1.5Nb and Cr-89Nb, which are in equilibrium with $NbCr_2$ at 1473 K in Cr-Nb binary system, are also estimated by Vegard's law between Cr and Nb. The composition of the two solid solutions are read from the Cr-Nb binary diagram [87]. The lattice constants 6.967 kX of Cr-rich C15 NbCr2 in equilibrium with Cr-rich BCC and 6.987 kX of Nb-rich C15 $NbCr_2$ in equilibrium with Nb-rich BCC at 1273 K are referred from Goldschmidt's research [102], which is converted by using the coefficient of 0.1002 nm/kX [103], although Rudy has also reported that the lattice parameter of C15 NbCr2 decreases with the increase of Cr atomic fraction in alloys

heat-treated at higher temperature [104]. It was confirmed that the lattice constants of BCC_1 and BCC_2 in alloy #2 are very close to the results of Goldschmidt and Brand [102]. The lattice parameters of each phase for each alloy are listed in Table 7. The atoms of the three matched BCC/C15 interfaces are illustrated in Fig. 40. The interatomic distances and planar disregistry calculated from the lattice constants for alloy #3 are listed in Table 8 as an example. In the same manner, the lattice misfit for the other alloys were determined, as presented in Table 9 and shown in column diagram (Fig. 41) for comparison.

The δ value increases with the lattice constant of the BCC matrix, i.e., with a decrease in the Cr content, which slightly decreases at first for OR 1 and OR 2. OR 1 and OR2 are more favorable for alloy #3 due to the small δ values. Relatively larger δ values are presented for alloy #1, in which case no precipitation is found in the grain interior. For alloy #2, the Cr-rich BCC_1 matches well with C15 in the form of OR 1 and OR 2 after decomposition to BCC_1 and BCC_2. OR 3 also exists in alloy #2 but not in alloy #3 although the δ values are almost the same for these two alloys (#3 and #2-BCC_1). One possible explanation is that the phase boundaries between BCC_1 and BCC_2 in alloy #2 may facilitate the formation of C15 $NbCr_2$ in OR 3 due to fast diffusion. The change in elastic constants with the composition of the BCC matrix may have some effect on the selection of OR through the interfacial elastic energy. The δ values for OR 1 and OR 2 are 8.75% for alloy #1, where no fixed OR exists. OR 3 with a δ value of 8.78% is not found in alloy #3. Bramfitt suggested that the δ of 12% is the upper limit value for the formation of a matching interface in supercooled liquid iron [100]. It appears the limit value is around 8%, which is much smaller than the 12% in the present system.

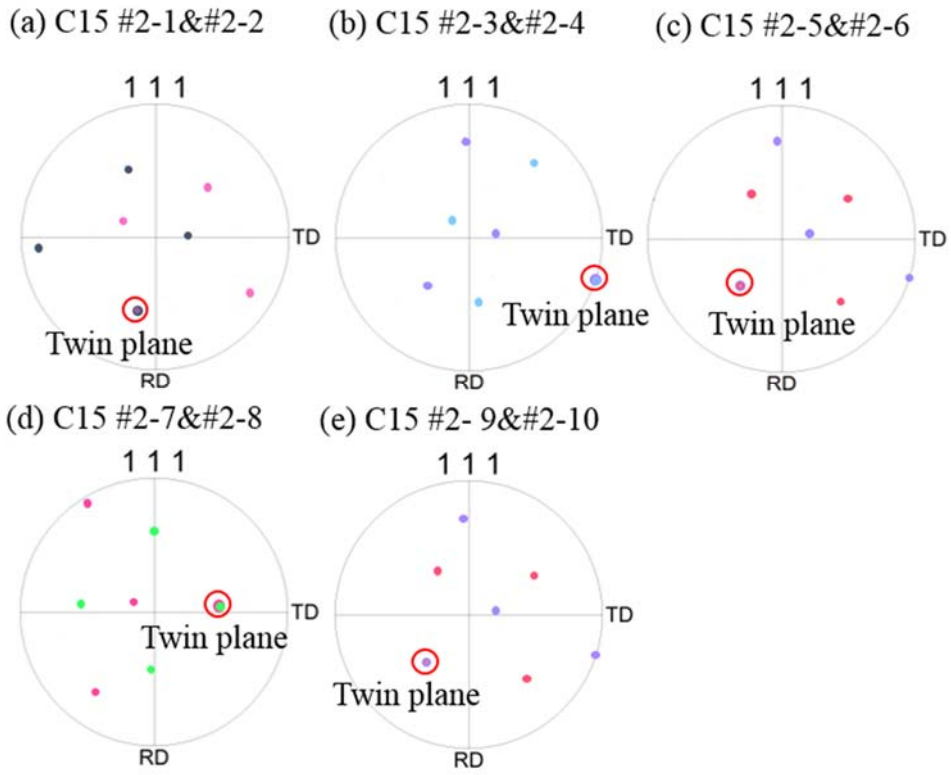

Fig. 34. PFs for the grains marked in Fig. 33(d). (Colors for <111> poles correspond to the colors in Fig. 33(d))

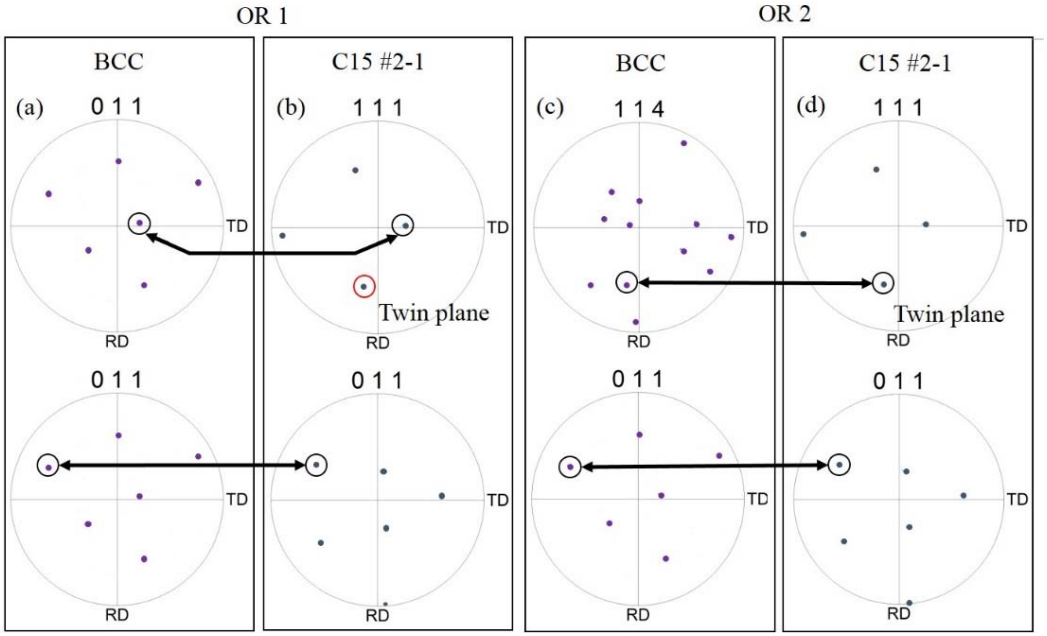

Fig. 35. PFs for (a,c) the BCC matrix and (b,d) C15 #2-1 in Fig. 33(d).

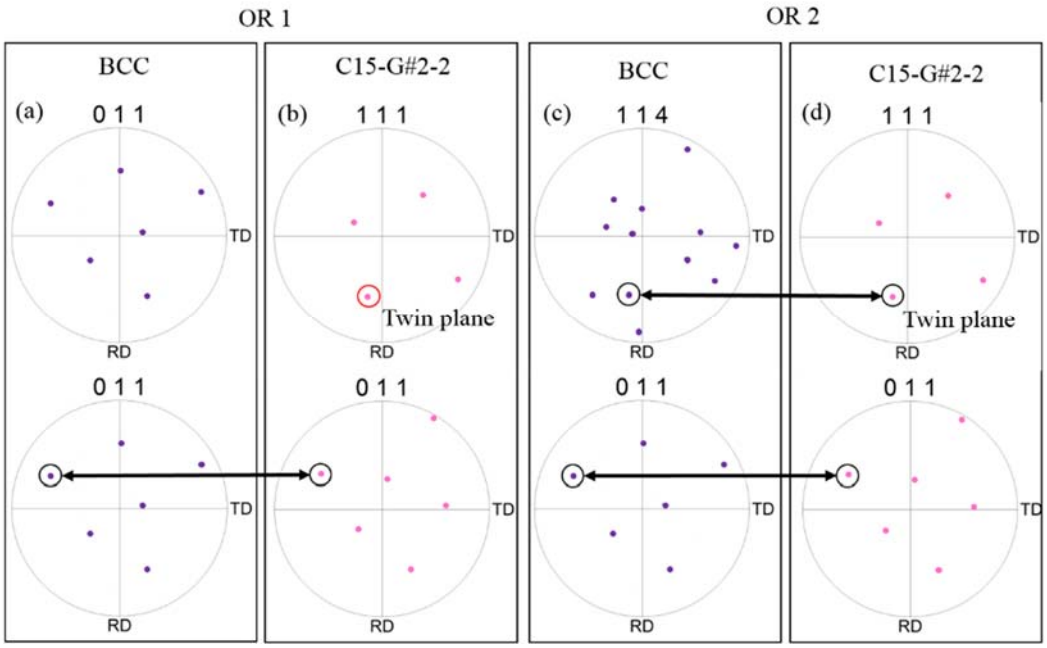

Fig. 36. PFs for (a,c) the BCC matrix and (b,d) C15 #2-2 in Fig. 33(d).

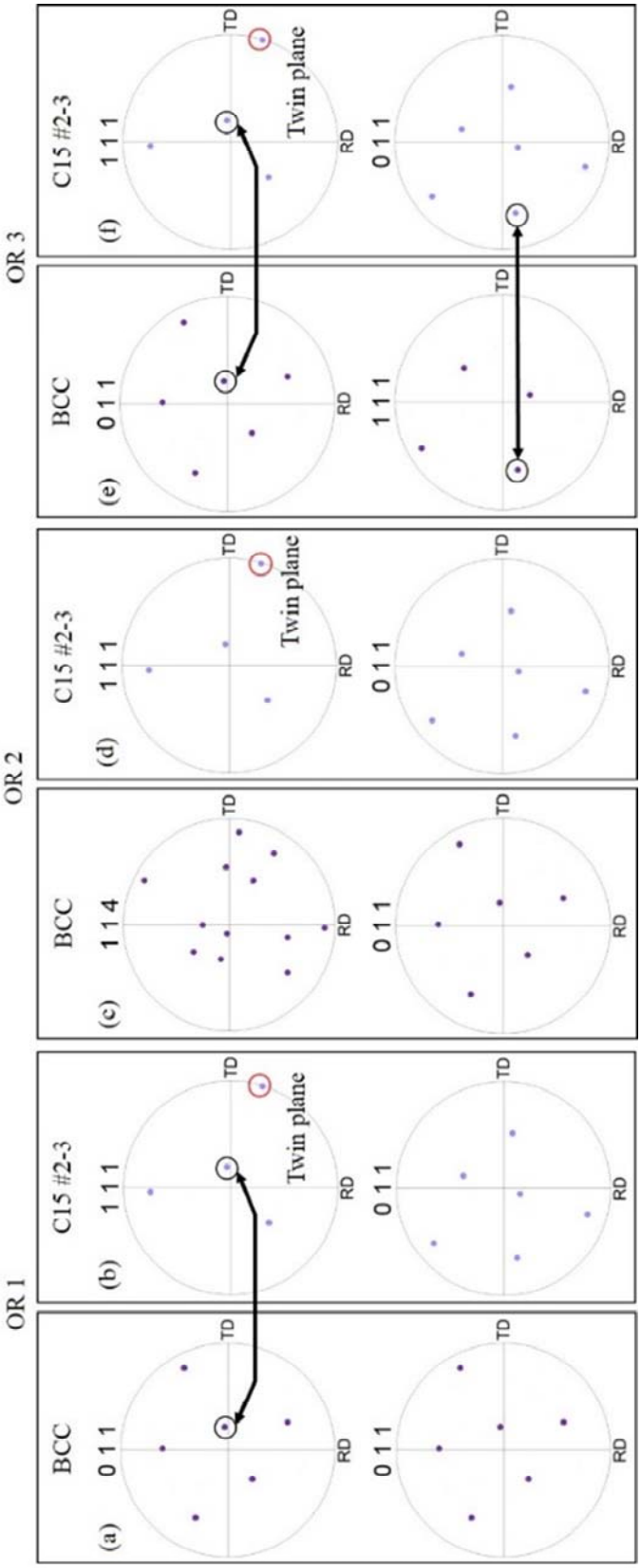

Fig. 37. PFs for (a,c,e) the BCC matrix and (b,d,f) C15 #2-3 in Fig. 33(d).

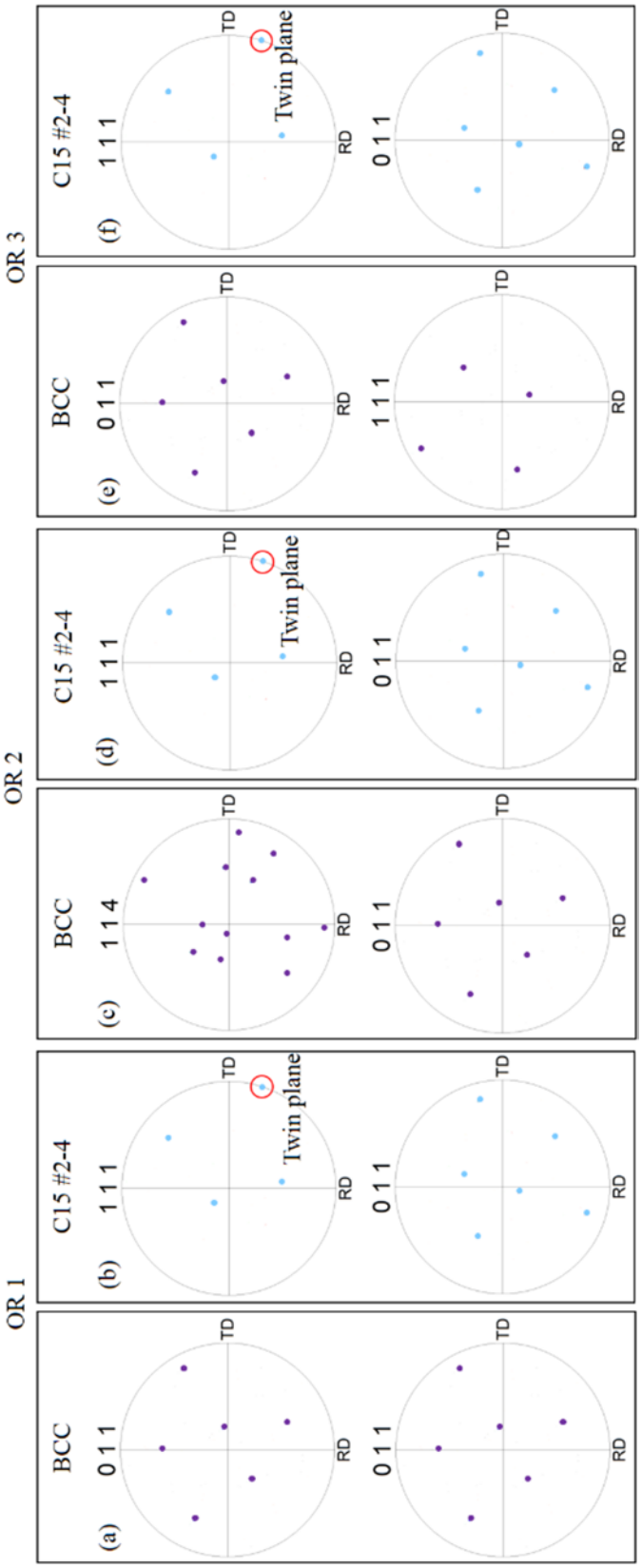

Fig. 38. PFs for (a,c,e) the BCC matrix and (b,d,f) C15 #2-4 in Fig. 33(d).

Table 6 OR for grains in Fig. 33(d).

Grain	OR 1	Involving $(111)_{C15}$ as twin plane	OR 2	Involving $(111)_{C15}$ as twin plane	OR 3	Involving $(111)_{C15}$ as twin plane
#2-1_{O1}	Yes	No	Yes	Yes	No	---
#2-2_{T1}	No	---	Yes	Yes	No	---
#2-3_{O2}	No	---	No	---	Yes	No
#2-4_{T2}	No	---	No	---	No	---
#2-5_{O3}	No	---	No	---	Yes	No
#2-6_{T3}	No	---	No	---	No	---
#2-7_{O4}	Yes	No	Yes	Yes	No	---
#2-8_{T4}	No	---	Yes	Yes	No	---
#2-9_{O5}	No	---	No	---	Yes	No
#2-10_{T5}	No	---	No	---	No	---

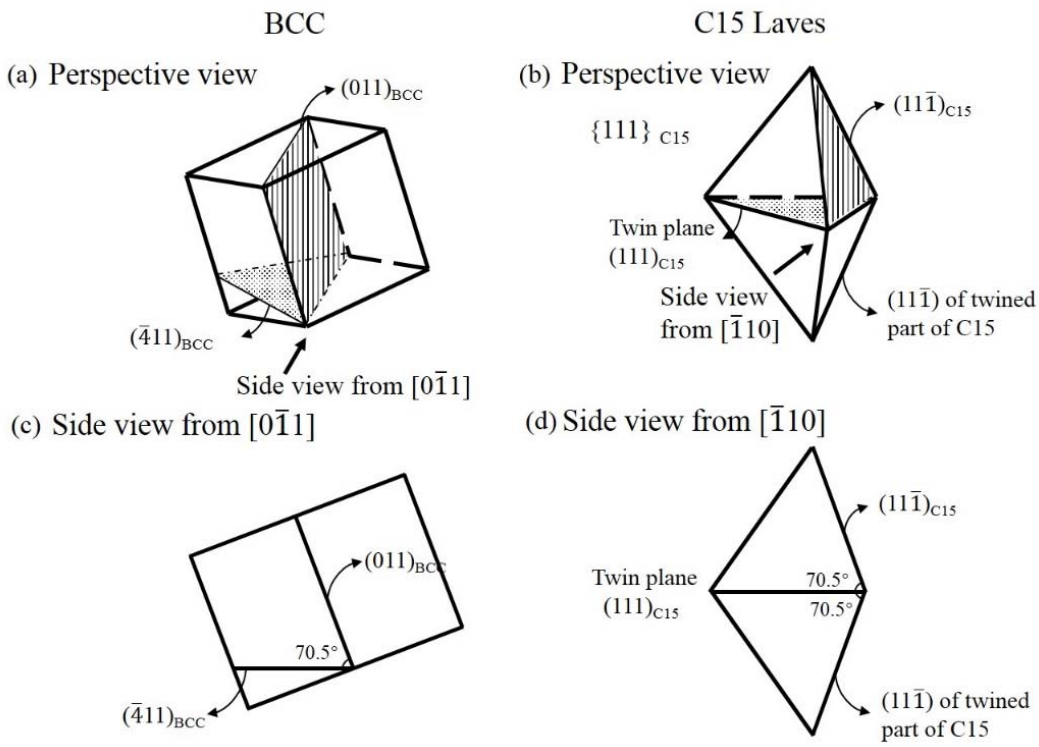

Fig. 39. Schematic diagram showing the crystallographic OR based on OR 1 and OR 2 between the C15 precipitate and BCC matrix phase in alloy #2. (a) Perspective view of the BCC unit cell, (b) perspective view of $\{111\}_{C15}$ tetrahedrons after twinning, (c) side view of BCC indicated in (a), and (d) side view of C15 indicated in (b).

Table 7. Lattice constant of phases at different temperatures

Alloy	Phase	Lattice constant a/nm, (at RT)	Thermal expansion coefficient $\alpha/10^{-6}$ K	Lattice constant a*/nm, (at 1473 K)
	Cr-1.5Nb, BCC	0.2891	10	0.2925
	$NbCr_2$ (C15)	0.6981 [102]	6.4 [105]	0.7033
#3	BCC	0.2960	10	0.2995
	$NbCr_2$ (C15)	0.6979	6.4 [105]	0.7031
#2	BCC_1	0.2965	10	0.3000
	BCC_2	0.3132	10	0.3169
	$NbCr_2$ (C15)	0.6986	6.4 [105]	0.7038
#1	BCC	0.3151	10	0.3188
	$NbCr_2$ (C15)	0.6983	6.4	0.7035
	Cr-89Nb, BCC	0.3255	10	0.3293
	$NbCr_2$ (C15)	0.7001 [102]	6.4 [105]	0.7054

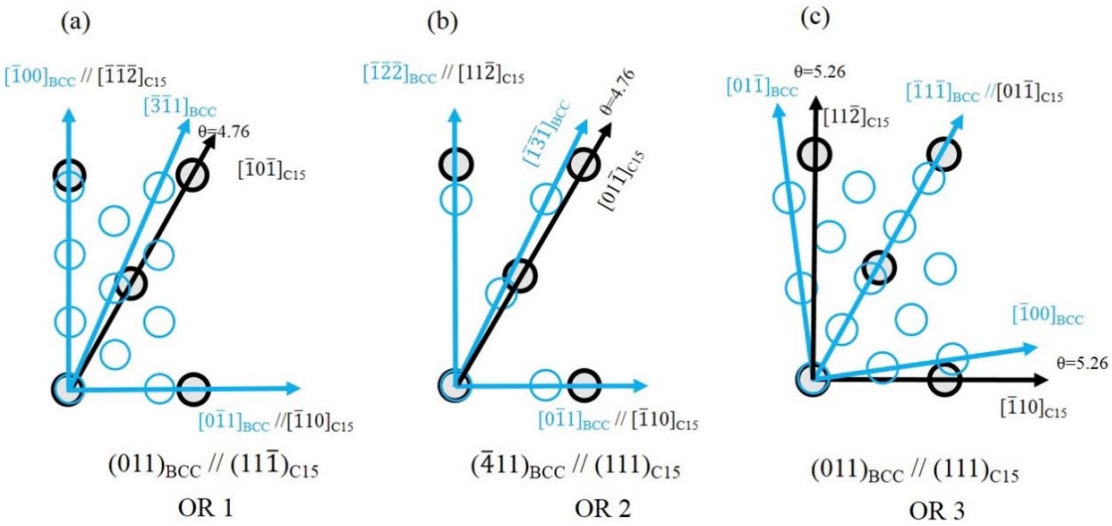

Fig. 40. Atomic matching at three BCC/C15 interfaces.

Table 8 Planar disregistry calculations between C15 $NbCr_2$ and the BCC matrix phase for alloy #3.

Planes	$[uvw]_\alpha$	$[uvw]_P$	$d_{[uvw]\alpha}$	$d_{[uvw]P}$	θ/deg	δ (%)
(011)BCC // (11$\bar{1}$)C15	3[$\bar{1}$00]$_{BCC}$	[$\bar{1}\bar{1}\bar{2}$]$_{C15}$	0.8984	0.8612	0	6.54
	[$\bar{3}\bar{1}$1]$_{BCC}$	[$\bar{1}0\bar{1}$]$_{C15}$	0.4966	0.4972	4.76	
	[0$\bar{1}$1]$_{BCC}$	[$\bar{1}$10]$_{C15}$	0.4235	0.4972	0	
($\bar{4}$11)BCC // (111)C15	[$\bar{1}\bar{2}\bar{2}$]$_{BCC}$	[11$\bar{2}$]$_{C15}$	0.8984	0.8612	0	6.54
	[$\bar{1}\bar{3}\bar{1}$]$_{BCC}$	[01$\bar{1}$]$_{C15}$	0.4966	0.4972	4.76	
	[0$\bar{1}$1]$_{BCC}$	[$\bar{1}$10]$_{C15}$	0.4235	0.4972	0	
(011)BCC // (111)C15	2[01$\bar{1}$]$_{BCC}$	[11$\bar{2}$]$_{C15}$	0.8470	0.8612	5.26	8.78
	2[$\bar{1}$1$\bar{1}$]$_{BCC}$	[01$\bar{1}$]$_{C15}$	0.5187	0.4972	0	
	2[$\bar{1}$00]$_{BCC}$	[$\bar{1}$10]$_{C15}$	0.5989	0.4972	5.26	

Table 9 Lattice misfit δ, between C15 $NbCr_2$ and the BCC matrix.

Alloy	δ/%		
	OR1	OR2	OR3
Cr-1.5Nb	7.17	7.17	7.79
#3	6.54	6.54	8.78
#2-BCC1	6.52	6.52	8.80
#2-BCC2	8.48	8.48	13.53
#1	8.75	8.75	14.27
Cr-89Nb	10.03	10.03	17.72

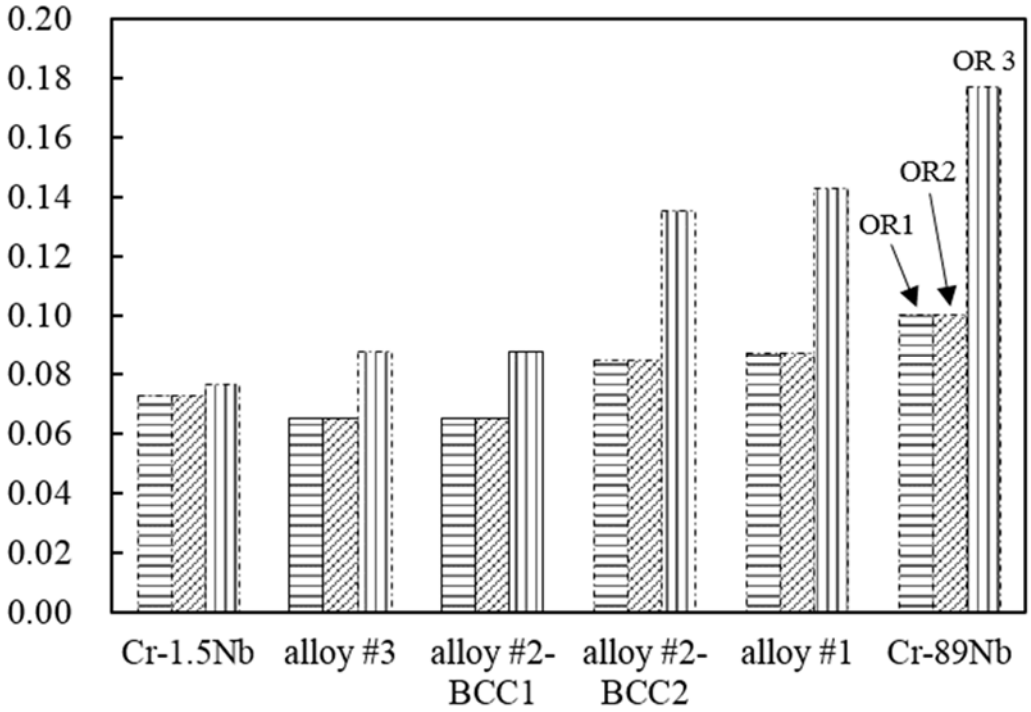

Fig. 41. The comparison of the δ values for each alloy.

3.4 summary

In this chapter, the isothermal sections of Cr-Mo-Nb ternary phase diagram and the evolution of microstructure are investigated. The precipitation behavior of C15 $NbCr_2$ Laves phase in various alloys at 1473 K is investigated by SEM, XRD, and EBSD at 1473 K. The results are summarized as follow:

(1) A three-phase region is found in the isothermal section of Cr-Mo-Nb ternary phase diagram at 1473 K. No three-phase region appears at 1773 K.

(2) The C15 $NbCr_2$ Laves precipitation morphology is quite different in the three alloys of #1, #2, and #3. After two-step heat treatment, gray precipitates appear at the GB and cellular structure is formed in alloy #1, while precipitates appear not only at the GB but also in the grain interior in alloy #3. Alloy #2 is turned out to be a three-phase alloy which consisted of fine lamellar structure of two BCC phases with relatively larger Laves precipitates.

(3) OR 1 and OR 2 with low lattice misfit are both observed between BCC matrix phase and C15 precipitates in alloys #3 and #2. Besides, OR 3 with a relatively larger δ value is also found in alloy #2, which may be resulted from existence of the phase boundaries of BCC_1 and BCC_2 formed after BCC decomposition. It seems the limit value is seemingly 8% for the formation of matching interface between BCC matrix and Laves precipitates.

Chapter 4

Microstructure evolution and mechanical properties of the three-phase alloy

In this chapter, the purpose was to determine the details of the microstructural evolution mechanism for a BCC_1/BCC_2/Laves three-phase alloy #2 composed of 50Cr-30Mo-20Nb in the Cr-Mo-Nb system. Microstructural evolution of the 50Cr-30Mo-20Nb alloy at a temperature of 1473 K was mainly considered here, although isothermal treatments at other temperatures were also conducted to reveal the precipitation behavior of the Laves phase. The strength of alloys heat treated at 1473 K for various periods after solid solution treatment was also evaluated using room-temperature Vickers hardness and compression tests, in order to determine the relationship between the microstructure and crack formation.

4.1 Microstructure evolution at 1473 K

Fig. 42 and 41 shows the microstructure of the 50Cr-30Mo-20Nb alloy before and after aging at 1473 K for various time periods following solution treatment at 1973 K for 1 h. The phases in the regions indicated by ①-⑤ in Fig. 41 were identified by TEM and EDS, and the results are listed in Table 10. As shown in Fig. 42(a), before aging, the alloy has a single-phase microstructure, with no evidence of $NbCr_2$ Laves phase precipitates. After aging at 1473 K for 3 h (Fig. 40(b)), dark Cr-rich BCC_1 particles appear in the matrix. At GBs, the Cr-rich particles are larger and the Mo-rich BCC_2 phases (bright regions) appear. Fig. 42(c) shows that the original BCC phase decomposes into dark Cr-rich BCC_1 phases and bright Mo-rich BCC_2 phases in the grain interiors (indicated by white arrows) after aging for 12 h. These phases form a broad banded structure (about 2 μm in width) with circular sub-structures that spread in the grain interiors and terminate at the original BCC phase GBs. The original matrix BCC phase gradually disappears with increasing aging time and is replaced by a BCC_1/BCC_2 two-phase alternating microstructure (Fig. 42(d)). Precipitation and growth of the blocky gray Laves phase occurs following longer aging times, as shown in Fig. 42(e) and 40(f); this phase also appears at GBs in the original BCC phase (area outlined by square in Fig. 40(c)) during the early aging stage. This sequence of microstructural evolution is consistent with former results.

The TEM images and SAED patterns in Fig. 41 show the details of the microstructure and phases present under different aging conditions. A comparison of Fig. 43(a) and Fig. 43 (b) shows that the original BCC phase decomposes into BCC_1 and BCC_2 phases following 6 h of aging. From the EDS results shown in Table 10, the black intragranular precipitates in Fig. 40(b) correspond to the Cr-rich BCC_1 phase. This stimulates the subsequent precipitation of a Mo-rich BCC_2 phase in adjacent regions (bright regions), which in turn induces the precipitation of a Cr-rich BCC_1 phase (dark regions), as shown in Fig. 43 (b).

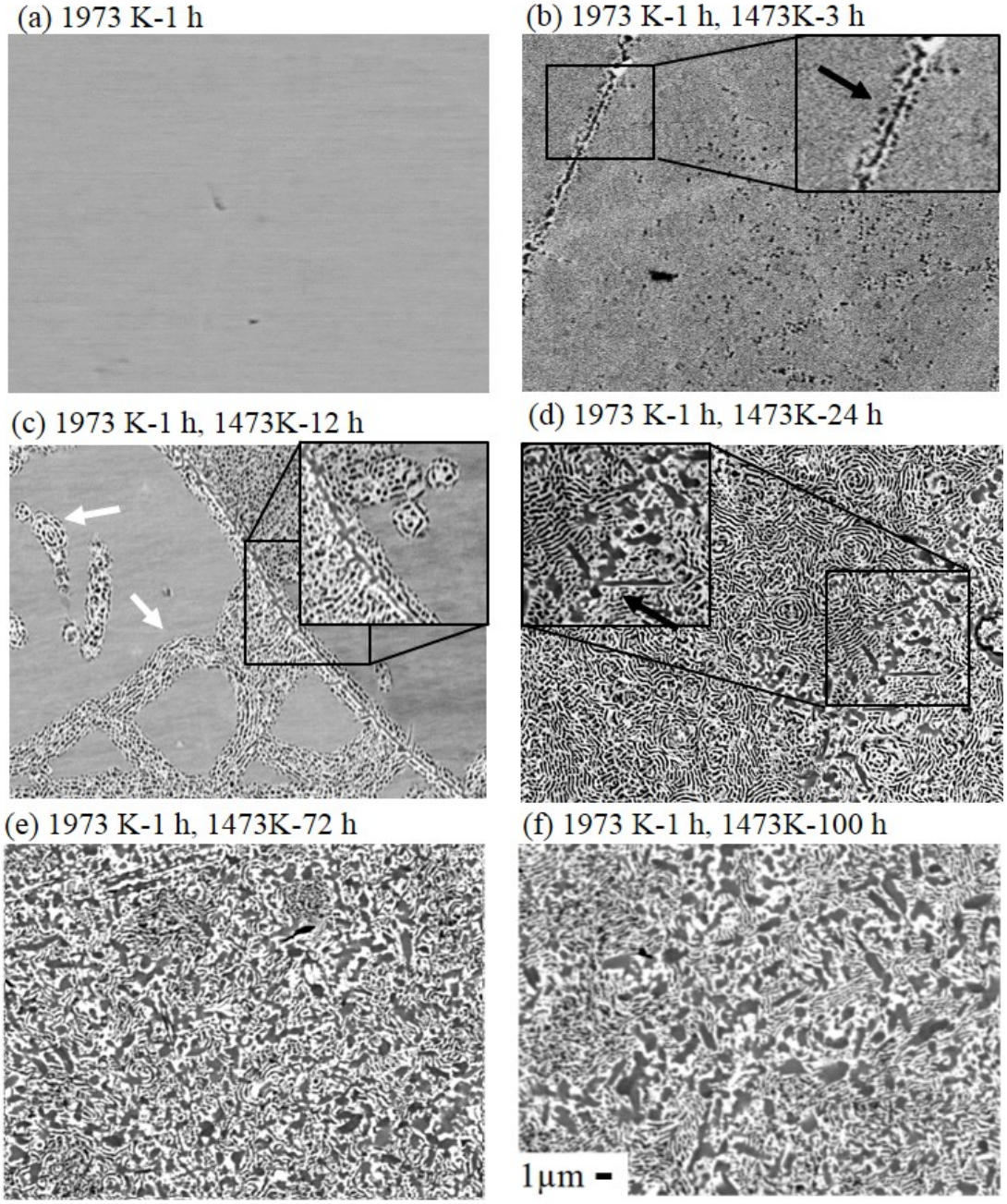

Fig. 42. Microstructural evolution of 50Cr-30Mo-20Nb alloy before and after aging at 1473 K following solution treatment at 1973 K for 1 h: (a) before aging, and aged for (b) 3 h, (c) 12 h, (d) 24 h, (d) 72 h, and (d) 100 h.

Figures 41(c)-(f) show TEM images of the alloy aged for 12 h, and SAED patterns for the original supersaturated BCC structure and the BCC_1/BCC_2 structure, which correspond to the original BCC area (A in Fig. 43(c)) and BCC_1/BCC_2 two-phase area (B in Fig. 43 (c), and the magnified view in Fig. 43 (d)), respectively. Diffraction spot doubling is seen in the SAED pattern in Fig. 43 (f), which indicates BCC regions with the same crystallographic orientation as each other (cube-on-cube). This verifies the decomposition of the original BCC phase into BCC_1 and BCC_2 phases in the grain interiors, and that the latter phases dominate the microstructure in the early stages of evolution.

TEM images of the alloy aged at 1473 K for 100 h and the corresponding SAED patterns are shown in Figs. 41(g)-(j). The BCC_1 and BCC_2 phases consistently maintain a cube-on-cube relationship, even after long-term aging, as shown in Fig. 43(i). Table 10 also shows that the dark phase is the Mo-rich BCC_2 phase, and the relatively large gray precipitate (denoted as ⑤) in Fig. 43(h) is the $NbCr_2$ Laves phase. The phase surrounding the Laves phase is mostly the gray Mo-rich BCC_2 phase, which implies that the Laves phase forms at the boundary of the Cr-rich BCC_1 phase and grows by consuming it.

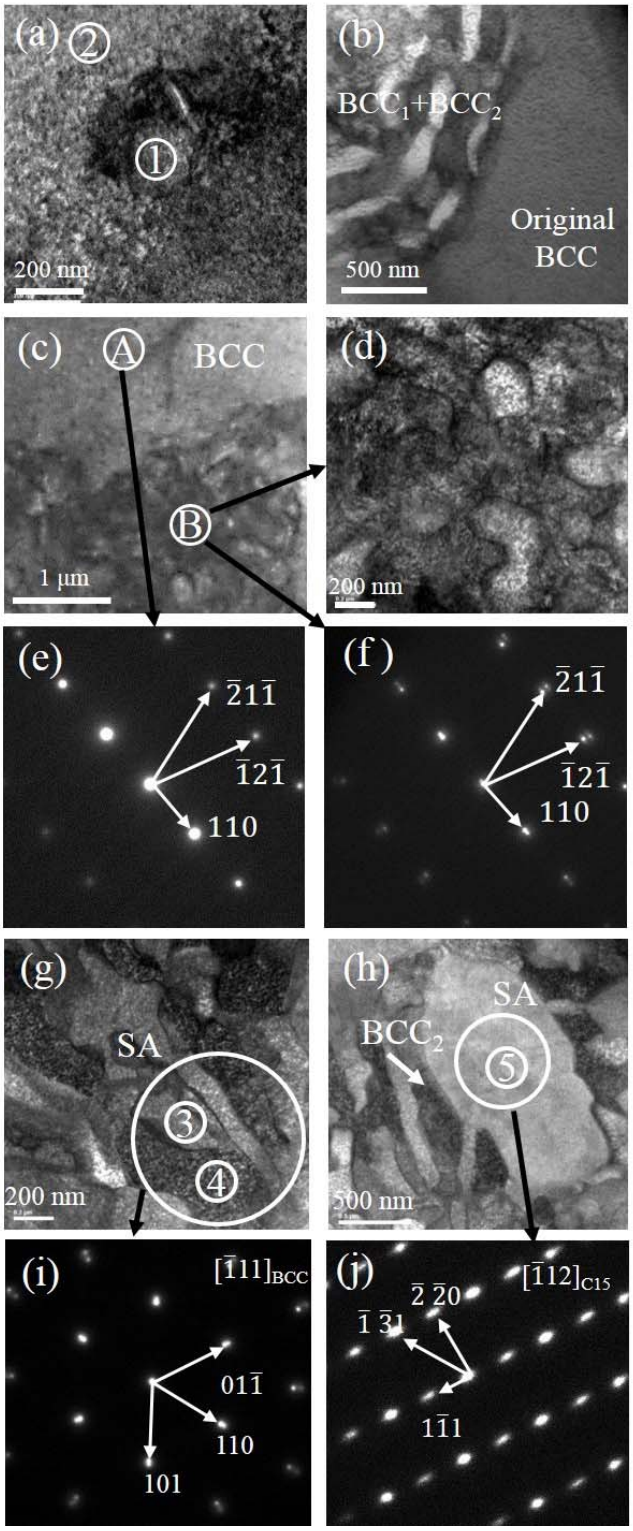

Fig. 43. TEM analyses of alloys aged at 1473 K for (a) 3 h, (b) 6 h, (c,d) 12 h, and (g,h) 100 h. SAED patterns for (e) region A in panel (c), (f) region B in panel (c), (i) region SA in panel (g), and (j) region SA in panel (h). (Numbers refer to regions analyzed using EDS, the results of which are shown in Table 10).

Table 10 EDS results for regions indicated in Fig. 43(a,g,h) (at%).

#	Cr	Mo	Nb	Phase constituent
1	74	19	7	BCC_1
2	47	33	20	BCC
3	73	23	4	BCC_1
4	23	54	23	BCC_2
5	63	10	27	$NbCr_2$

It should be noted that the XRD analysis of an alloy (Fig. 27) aged for 12 h revealed distinct peaks that corresponded to three BCC phases. The lattice constants were different from each other, which strongly suggests that microstructural evolution occurred through discontinuous precipitation (DP), with no evidence for a spinodal-like process. The TEM observations clearly indicate that the BCC_1 and BCC_2 phases are formed by a discontinuous precipitation (DP) process, and that the precipitation products gradually replace the parent phase (original BCC) by migration of the reaction front. However, this is also quite different from typical DP [106, 107], where nucleation typically occurs at GBs and growth is accompanied by GB migration [108]. Nevertheless, in the present study, intragranular nucleation of the Cr-rich BCC_1 phase in this alloy dominates the early stage of the precipitation process, and becomes a trigger for precipitation of the neighboring Mo-rich BCC_2 phase, which in turn induces further precipitation of the Cr-rich BCC_1 phase, until an alternating BCC_1/BCC_2 two-phase microstructure if finally formed. The mechanism for the occurrence of this type of DP is as yet unclear. This morphology shows a resemblance to spinodal decomposition [109-111] and surface-directed spinodal decomposition [112]. Further investigation of the reasons for the formation of such a unique microstructure is still required.

We proposed three different crystallographic ORs between the BCC matrix phase and the Laves phase precipitates in chapter 3, and it was shown that the lattice mismatch (δ) between the matrix BCC phase and the C15 Laves phase plays an important role in determining the OR. It was concluded that no Laves phase precipitates are formed in the grain interiors during the early stages, due to the relatively large lattice mismatch with the original BCC phase for any OR.

Fig. 43(i) and (j) show SAED patterns for the BCC and C15 Laves phases, respectively, obtained at the same sample tilt angle. The zone axes for the BCC and C15 phases are $<111>_{BCC}$ and $<112>_{C15}$, respectively. The {110} reflections for the BCC phase coincide with the {111} reflections for the C15 phase. Thus, the OR (OR4)

between the BCC matrix and the C15 phase is:

$$(01\bar{1})_{BCC}//(1\bar{1}1)_{C15}$$

$$[\bar{1}11]_{BCC}//[\bar{1}12]_{C15}$$

Previous studies [88, 93] showed that the OR between the BCC and C15 Laves phase is:

$$(01\bar{1})_{BCC}//(1\bar{1}1)_{C15}$$

$$[011]_{BCC}//[\bar{1}01]_{C15},$$

which was defined as OR 1 in alloy #2, which corresponds to the present alloy.

The two ORs share common parallel planes, although the directions are different. The angle between the $[\bar{1}11]_{BCC}$ and $[011]_{BCC}$ zones is 35.26°, and the angle between the $[\bar{1}12]_{C15}$ and $[\bar{1}01]_{C15}$ zones is 30°. When the $[\bar{1}11]_{BCC}$ zone is parallel to the $[\bar{1}12]_{C15}$ zone, the angle between the $[011]_{BCC}$ and $[\bar{1}01]_{C15}$ zones is 5.26°. Therefore, the OR observed here can be considered to have a small deviation from OR 1 reported by other researchers and in our previous study [11].

The lattice misfit for OR4 is relatively large and it seems this OR is not preferable. When OR4 is considered, the angle between the $[\bar{1}1\bar{1}]_{C15}$ and $[\bar{3}\bar{1}1]_{C15}$ zones is 0.5° and the lattice misfit becomes 6.38% between the BCC_1 phase and the Laves phase when these two directions are taken into consideration to calculate δ value. Actually, it is not easy to tell that $[\bar{1}1\bar{1}]_{C15}$ and $[\bar{3}\bar{1}1]_{C15}$ are not parallel due to the small angle. In this case, the relatively closer atom is taken into account instead of the observed direction, which is very vital when calculating the δ value.

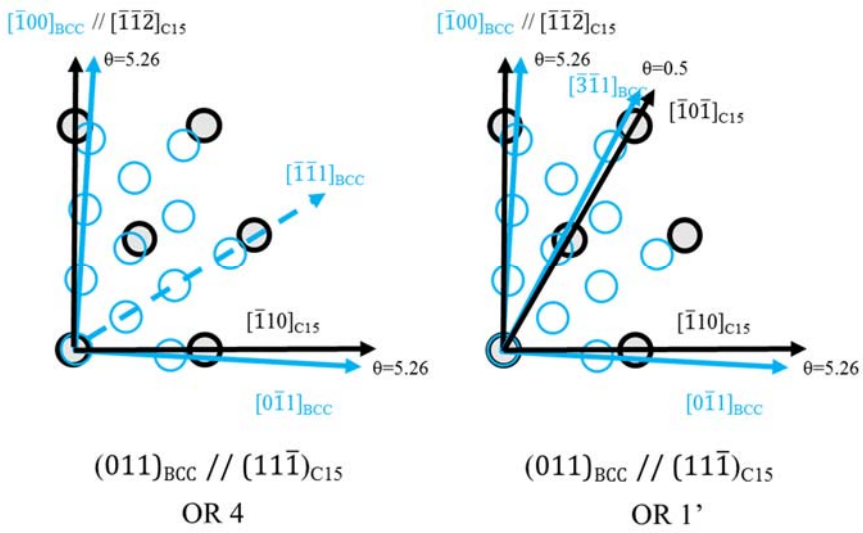

Fig. 44. Atomic matching at BCC/C15 interfaces for observed OR.

Table 11 Lattice misfit δ, between C15 $NbCr_2$ and the BCC matrix for observed OR.

Alloy	δ/%	
	OR4	OR1'
#2-BCC1	9.56	6.38
#2-BCC2	8.22	8.58

Therefore, the low δ value between the Cr-rich BCC_1 and Laves phases facilitates the precipitation of the Laves phase by consumption of the Cr-rich BCC_1 phase. As reported by Cui et al. [113] and Xu et al. [114], the growth of a $(Fe,Cr)_2(Mo,W)$ type Laves phase close to a $(Fe,Cr)_{23}C_6$ type $M_{23}C_6$ carbide phase proceeds by consumption of the Cr-rich carbide in the vicinity. Similarly in the present study, the $NbCr_2$ Laves phase surrounded by the Mo-rich BCC_2 phase may grow at the expense of the Cr-rich BCC_1 phase in the vicinity. This is also consistent with previous SEM observation results. A schematic diagram of the proposed microstructural evolution mechanism is shown in Fig. 45.

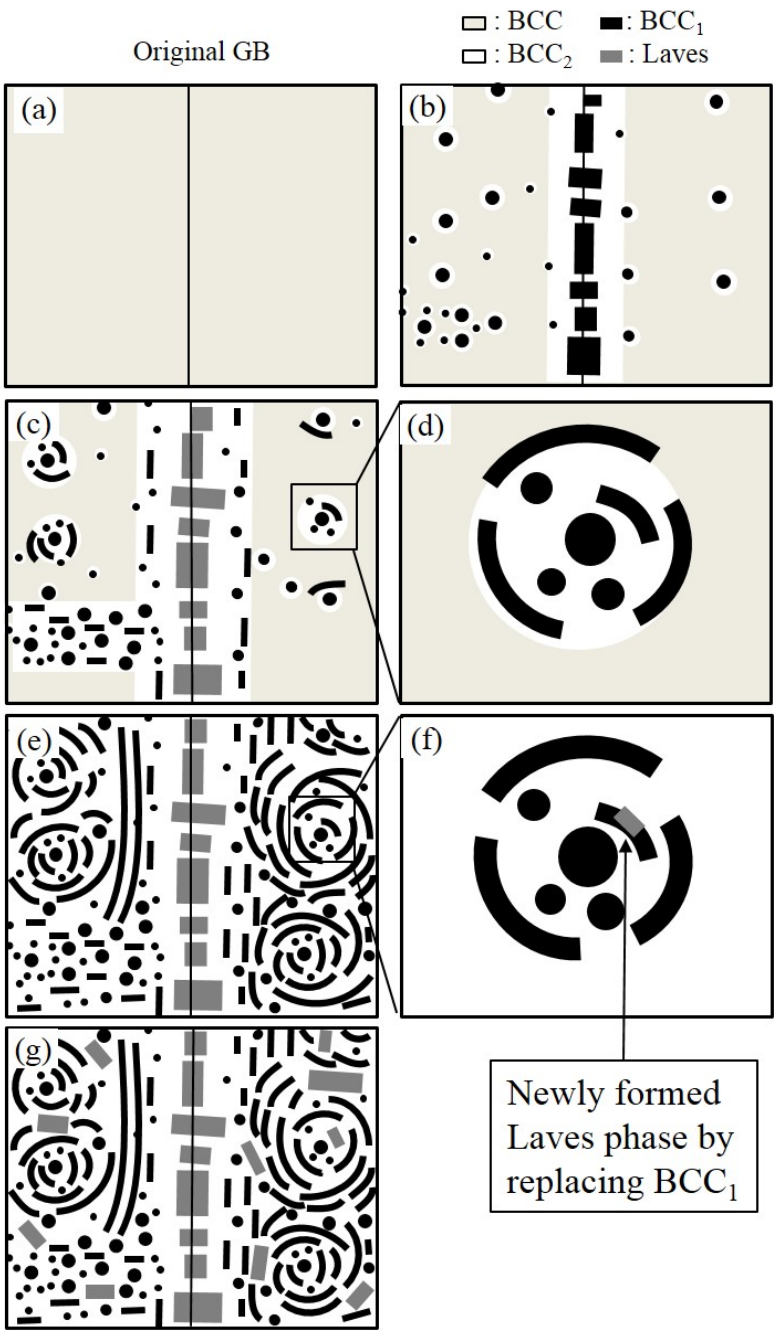

Fig. 45. Schematic diagram of the microstructural evolution of 50Cr-30Mo-20Nb alloy.

4.2 Temperature dependence of microstructure evolution

Fig. 46 shows SEM micrographs of specimens aged at three different temperatures. Similar morphologies were obtained for alloys heat treated at 1423 K, 1473K and 1523 K after solution treatment at 1973 K for 1 h. At relatively high temperature, precipitation of the Laves phase (gray phase) occurs in BCC_1/BCC_2 regions before full BCC decomposition takes place, due to the higher diffusion rate at the BCC_1/BCC_2 interphase boundaries. On the other hand, for heat treatment at 1773 K without a solution treatment, no BCC decomposition is observed and the microstructure indicates a BCC/Laves two-phase alloy.

The decomposed fraction of the original BCC phase and the fraction of the precipitated Laves phase as a function of the isothermal aging time are shown in Fig. 47. Although the BCC decomposition curves include the Laves phase precipitated in the BCC_1/BCC_2 two-phase structure, they also present the precipitation rates for alternating BCC_1 and BCC_2 phases from the original BCC phase because the Laves phase always precipitates at BCC_1/BCC_2 interfaces and not in BCC grain interiors. The three BCC decomposition curves (precipitation of BCC_1 and BCC_2 phases) appear to be sigmoidal. The interface area (reaction front) between the decomposition products and the original BCC phase first increases, and then decreases due to the reduction in the amount of the original BCC phase as the aging time is increased.

The fraction of the Laves phase also increases at a faster rate in the alloy heat treated at higher temperature. Although the fraction of the Laves phase and the aging time appear to have a linear relationship, a similar growth rate is evident at all three temperatures once nucleation has begun. Precipitation of the Laves phase always occurs after the formation of the BCC_1/BCC_2 two-phase microstructure. It starts as soon as individual BCC1/BCC2 two-phase areas are formed, so that each area undergoes precipitation for different lengths of time. The Mo-rich BCC_2 phase surrounding the

Laves phase may also govern the size of the Laves phase. However, further investigation is required to clarify these complicated kinetics.

Fig. 48 shows a time-temperature-transformation (TTT) diagram obtained from the transformation curves. The time taken to achieve 1% transformation to the BCC_1/BCC_2 mixed phase and precipitation of the Laves phases is taken to be the starting time. The transformation curve for the Laves phases is on the right side of the BCC_1/BCC_2 transformation curve because precipitation of the Laves phases always occurs after BCC decomposition. The incubation times for BCC decomposition at 1473 and 1523 K are so close that the 'nose' of the curve is likely to be around 1523 K, where the maximum transformation rate is obtained. At higher temperatures, the driving force for the transformation gradually deceases, which results in a lower transformation rate. When the temperature is sufficiently high, e.g., 1773 K, the BCC_1/BCC_2 transformation curve disappears due to the absence of BCC decomposition. Although the driving force for the precipitation of the BCC_1 and BCC_2 phases continues to increase below the 'nose' temperature, the transformation is impeded by slow diffusion. Therefore, two 'C' shaped curves can be expected for BCC_1/BCC_2 and Laves phase transformations.

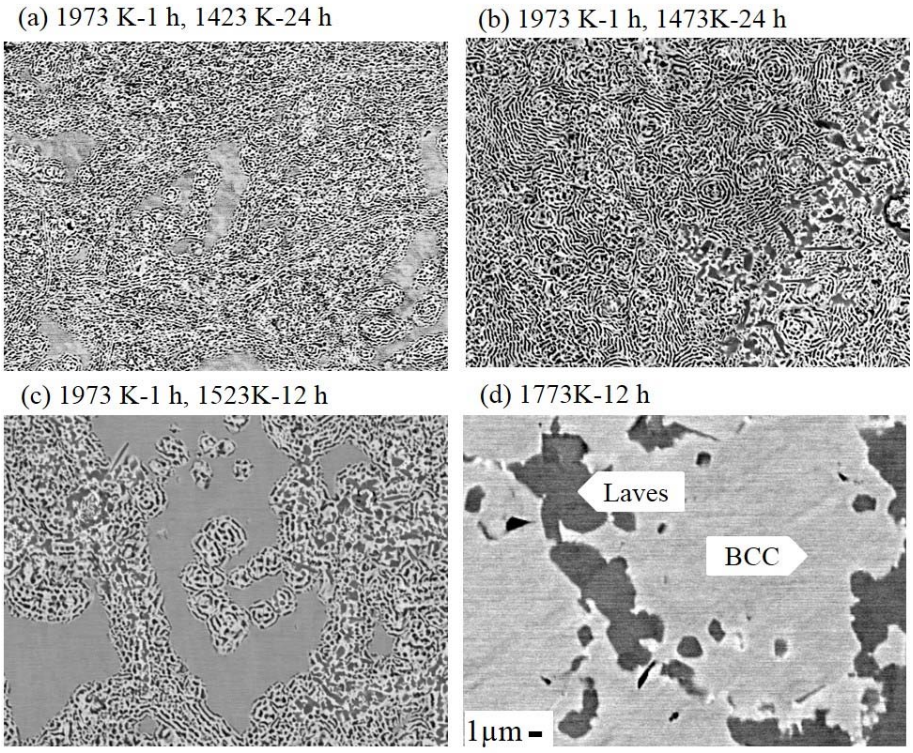

Fig. 46. SEM images of 50Cr-30Mo-20Nb alloy aged (a) at 1423 K for 24 h after solution treatment (1973 K/1 h), (b) at 1473 K for 24 h after solution treatment, (c) at 1523 K for 12 h after solution treatment, and (d) at 1773 K for 12 h without solution treatment.

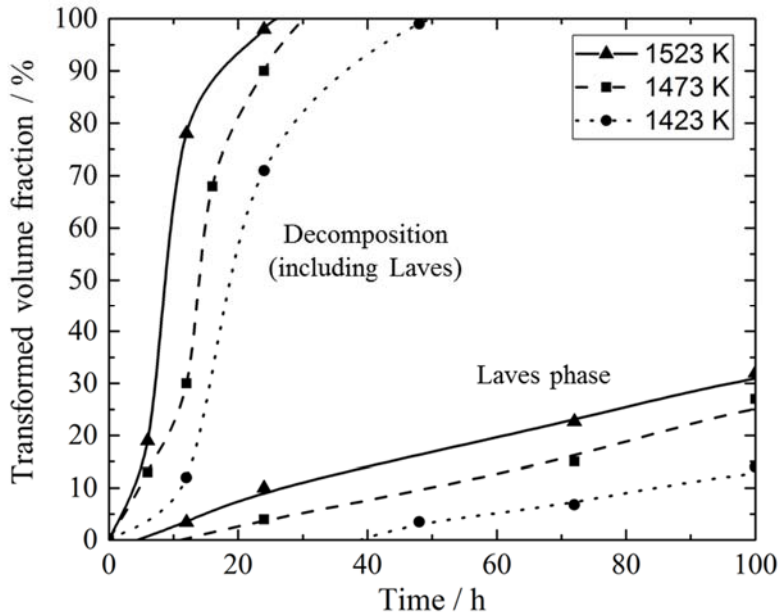

Fig. 47. Transformed volume fraction for 50Cr-30Mo-20Nb alloy as function of aging time at various temperatures.

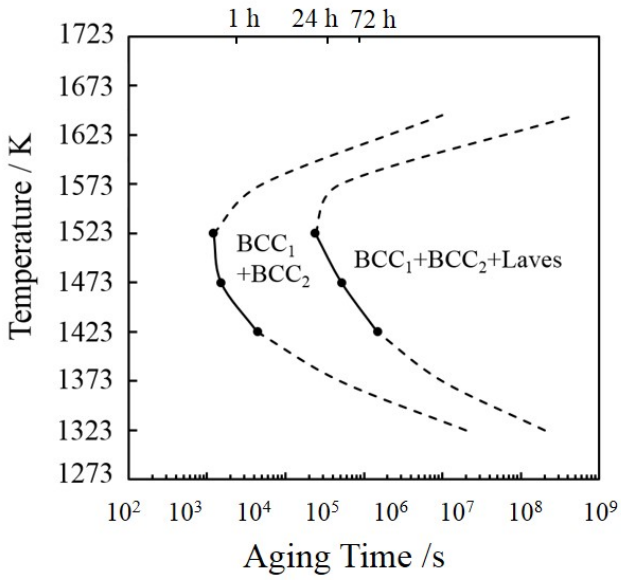

Fig. 48. TTT diagrams for BCC decomposition and Laves phase precipitation in 50Cr-30Mo-20Nb alloy.

4.3 Mechanical properties

Fig. 49 shows SEM images of the microstructure of alloys produced under different heat-treatment conditions after Vickers indentation tests. In both cases, the area of the indentation is almost the same. For the alloy directly annealed at 1473 K without solution treatment at 1973 K, cracks are present in the extensive Laves phase at the corners of the Vickers indentations because of stress concentration, as shown in Fig. 49(c) and 46(d). The cracks are impeded at the interface between the Laves phase and the Mo-rich BCC_2 phase, which indicates that ductile phase toughening is effective for suppressing crack propagation [115, 116]. Zhu et al. [38] evaluated the fracture toughness of the $NbCr_2$ Laves phase, which is around 0.9 MPa$\sqrt{m}\sqrt{\mathrm{m}}$, by Vickers indentation testing using:

$$\mathrm{K} = 0.016\left(\frac{E}{HV}\right)^{1/2}\frac{P}{c^{3/2}}, \tag{2}$$

where E is Young's modulus, HV is the Vickers hardness, P is the indentation load and c is the average length of the four surface radial cracks from the indent center to the crack tip. Although it is difficult to estimate the fracture toughness of the present multiphase alloys by Vickers indentation tests because no half-penny cracks can be produced, even at higher loads [117], the average length of the four radial cracks evaluated according to the previously reported toughness is about 60 μm [38, 118], which is much longer than even the longest crack in the present study (about 20 μm), as shown in Fig. 49. No obvious cracks are apparent at the corners of the indentation in the alloy with a fine-grained microstructure (Fig. 49(e) and (f)). The fine-grained microstructure, which is composed of a brittle Laves phase and a BCC_1/BCC_2 two-phase matrix undoubtedly plays an important role in preventing the formation of cracks, which also illustrates that improved fracture toughness could be expected from such alloys with fine-grained structures.

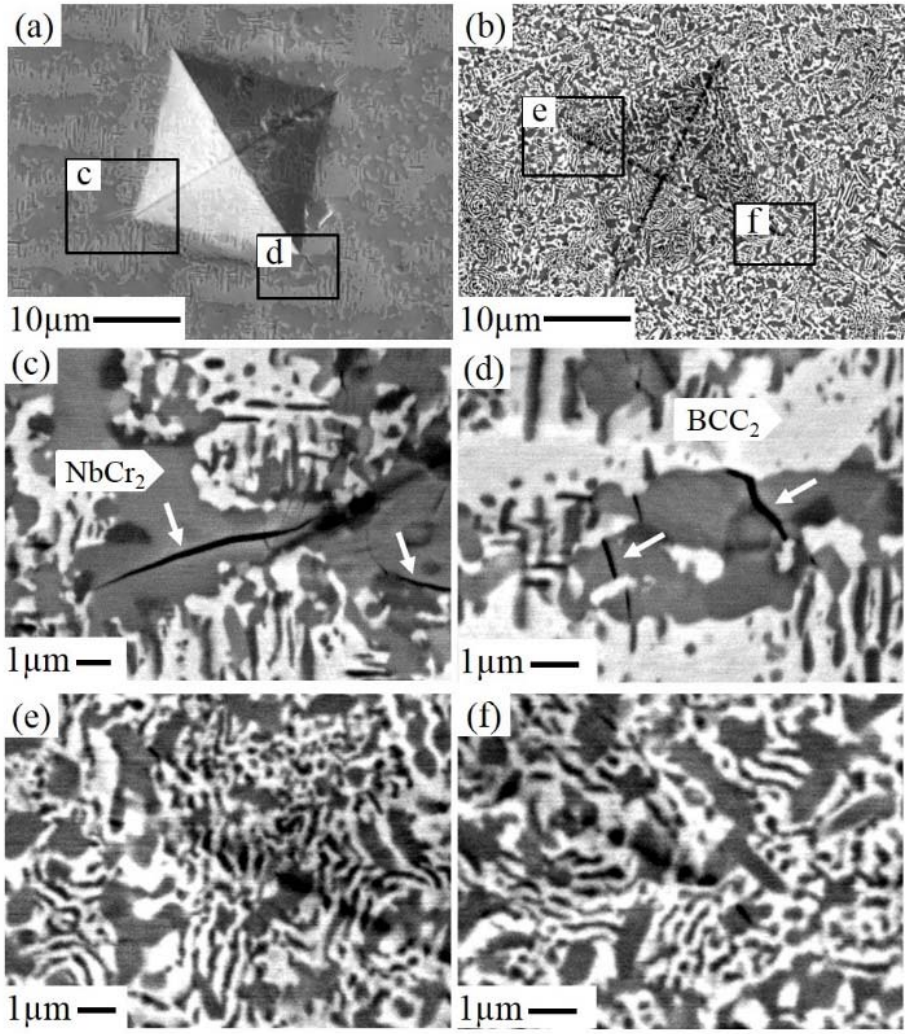

Fig. 49. SEM images of 50Cr-30Mo-20Nb alloy after Vickers hardness test: (a) aged at 1473 K for 168 h without solution treatment, (b) aged at 1473 K for 72 h following solution treatment at 1973 K for 1 h. (c,d) Area indicated in (a), and (e,f) area indicated in (b).

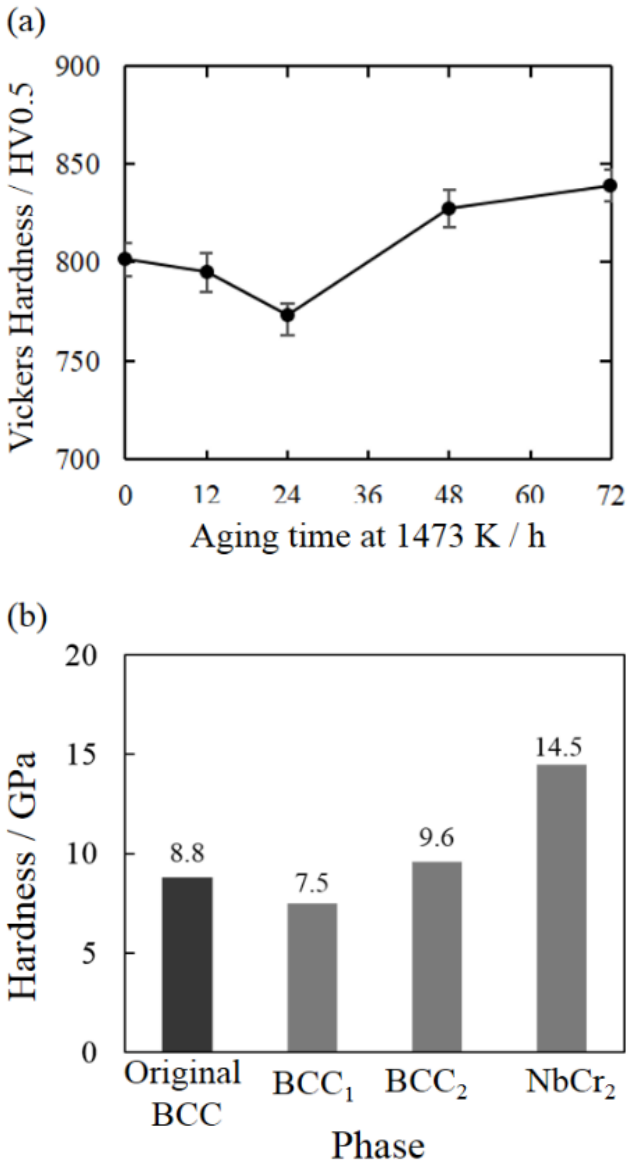

Fig. 50. (a) Vickers hardness for 50Cr-30Mo-20Nb alloy as function of aging time at 1473 K, and (b) hardness of each phase measured by nanoindentation.

Fig. 50(a) shows the dependence of the hardness on aging time at 1473 K. The maximum value of 839±8 HV is obtained after 72 h, and this is very similar to the hardness values reported for the $NbCr_2$ Laves phase [38, 52]. Even when it contains the two BCC phases, the alloy still maintains very high hardness and improved toughness. Unlike the typical aging process [119-121], the hardness changes only slightly at the early stage and then reaches a minimum of 773±7 HV after 24 h, when the microstructure is composed of the two BCC phases. Fig. 50(b) shows that the hardness of the Cr-rich BCC_1 phase (7.5 GPa) obtained by nanoindentation hardness testing is lower than that for the original supersaturated BCC phase (8.8 GPa) and that for the BCC_2 phase (9.6 GPa). This could therefore be the reason for the decrease in the Vickers hardness during BCC decomposition. The hardness of the alloy is then increased by the subsequent aging at 1473 K due to the precipitation and growth of hard $NbCr_2$. The hardness of 14.5 GPa obtained in the present study is much larger than that for a monolithic $NbCr_2$ Laves phase evaluated by Vickers hardness tests [38, 52]. During Vickers hardness measurements of brittle materials, cracks may be formed, and this results in lower hardness values. The hardness of the previously evaluated Laves phase could be lower because of the difference in measurement methods.

Fig. 51(a) shows compressive stress-strain curves for the 50Cr-30Mo-20Nb alloy aged at 1473 K for various times and tested at room temperature. Even though the alloy with $NbCr_2$ is toughened by the BCC_1/BCC_2 two-phase matrix, no obvious plastic deformation is observed for any of the alloys at room temperature. A sharp drop in stress (indicated by broken circles) appears in all stress-strain curves during compression, and the compression test for one of the samples was terminated when microcracks were formed (Fig. 51(c)); these were observed using optical microscopy of the surface of the alloy aged for 72 h after unloading. The unalloyed $NbCr_2$ has been reported to be deformable at temperatures above 1473 K [47], and the deformation temperature was reduced by the addition of Mo to $NbCr_2$ [48]. In addition, duplex alloys composed of the $NbCr_2$ Laves phase and the Cr-rich BCC phase showed a significantly reduced

brittle-to-ductile transition temperature (BDTT) in the Cr-Nb-Mo system; however, plastic deformation was only observed at temperatures above 1223 K with a large volume fraction of $NbCr_2$ [76]. Li et al. [79] observed a yield stage in arc-melted Cr-20Nb BCC/Laves two-phase alloys during compression testing at room temperature. A subsequent high-temperature observation is planned in order to determine how the BCC phases affect the mechanical properties in terms of the BDTT behavior.

The crack initiation strength and fracture strength of each alloy evaluated from compression tests are plotted in Fig. 52. The fracture strength is almost unchanged for heat treatment until 12 h, reaches a maximum value of 1493 MPa for heat treatment at 1473 K up to 24 h, which is consistent with the Vickers hardness results, and then remains almost constant with increasing aging time. This indicates that for aging periods longer than 24 h, the precipitation and growth of $NbCr_2$ has little effect on the fracture strength. However, the crack initiation strength decreases up to 12 h of aging, then increases up to 48 h, and then decreases significantly for 72 h heat treatment. The volume fraction of the $NbCr_2$ Laves phase increases with increasing aging time, and has a significant impact on the crack initiation strength. The volume fraction of the Laves phase is around 10% for the alloy aged for 48 h. In the early stages of microstructural evolution, when there is a lower volume fraction of the Laves phase, the crack initiation strength is expected to be governed by the BCC_1/BCC_2 structure. When the volume fraction of the Laves phase exceeds a critical value, cracking can then occur easily. Therefore, a critical volume fraction of the Laves phase may exist where the highest crack initiation strength can be obtained.

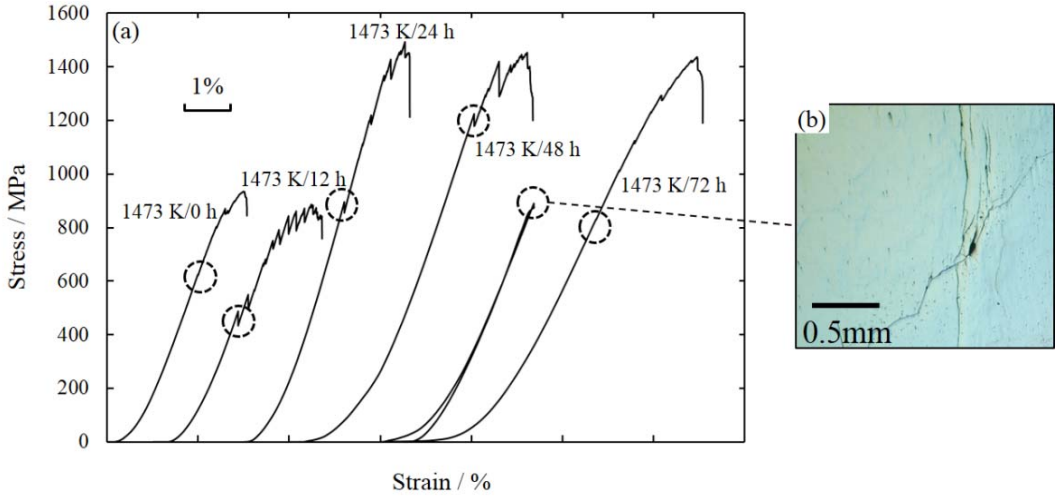

Fig. 51. (a) Compressive stress-strain curves for 50Cr-30Mo-20Nb alloy aged at 1473 K, (b) enlarged view of region where sharp stress drop occurred, and (c) surface microstructure of 1473 K/72 h sample after unloading when sharp stress drop occurred.

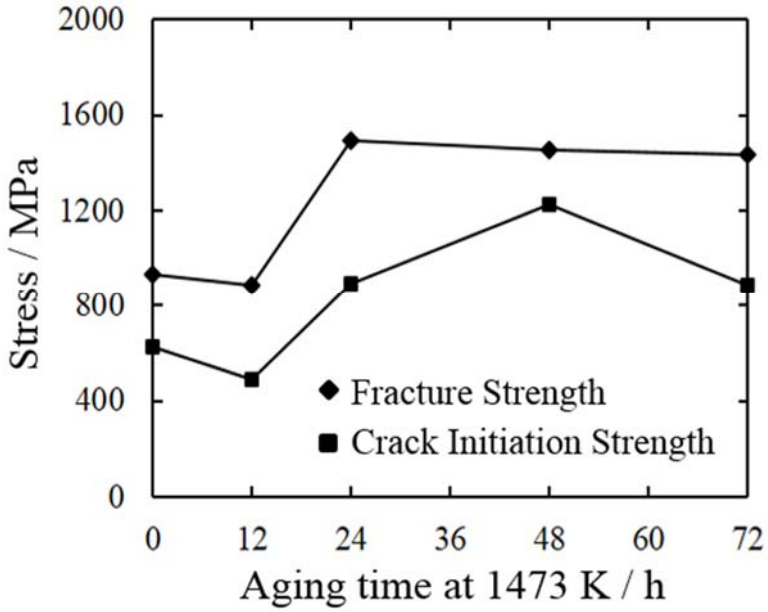

Fig. 52. Effect of heat-treatment time at 1473 K on strength of 50Cr-30Mo-20Nb alloy.

4.4 Summary

A three-phase alloy with a composition of 50Cr-30Mo-20Nb was studied. The microstructural evolution and precipitation behavior of the Laves phase were investigated using SEM, SAED, and TEM, and the fracture behavior was examined using Vickers hardness and compression tests at room temperature. The results are summarized as follows:

(1) During aging at 1473 K after solution treatment, fast intragranular precipitation of the Cr-rich BCC_1 phase induces precipitation of alternating BCC_1/BCC_2 phases through a DP process, and this morphology remains stable with increasing aging time.

(2) The Laves phase precipitates at BCC phase GBs and BCC_1/BCC_2 interphase boundaries. The growth of the Laves phase in BCC_1/BCC_2 two-phase areas consumes the Cr-rich BCC_1 phase in the vicinity.

(3) Higher-temperature heat treatment results in higher BCC decomposition and Laves phase precipitation rates, while at 1773 K no BCC decomposition occurs and a BCC/Laves two-phase structure is formed.

(4) The alloy aged at 1473 K for 72 h following solution treatment at 1973 K exhibits a hardness of 839±8 HV and has better toughness than that for an alloy directly annealed at 1473 K because no obvious microcracks were observed after the Vickers hardness test, even under a load of 0.5 kgf for 30 s.

(5) A minimum hardness and a highest fracture strength of 1493 MPa are obtained for the alloy aged at 1473 K for 24 h, where the two BCC phases dominate the microstructure. The volume fraction of the $NbCr_2$ Laves phase has a relatively small effect on the crack initiation strength.

Chapter 5

Effect of Si on the stability of Laves phase

The BCC_1/BCC_2/Laves three-phase alloy is also confronted with the same concerns with BCC/Laves two-phase alloy, poor oxidation resistance of the BCC phase at high temperatures. Silicon additions have previously been shown to be beneficial to the mechanical properties of Cr/Cr_2Ta based alloys, increasing both the hardness and room temperature fracture toughness [122] as well as improving the high temperature oxidation behavior [51]. Besides, Si seems to enhance the stability of $NbCr_2$ and the polytype of Laves phase changes with the increase of Si content. This chapter investigates the effect of Si on the stability of Laves phase at high temperature 1973 K and a part of the Cr-Nb-Mo-Si quaternary phase diagram. Subsequent heat treatment at 1573 K is conducted to investigate the effect of Si on the stability of the three-phase alloy. The alloy compositions are shown in Table 12. The alloys are named as 0 Si, 0.1 Si, 0.5 Si, 1 Si, 5 Si according to the amount of Si.

Table 12 Nominal compositions of alloys.

No.	Cr	Mo	Nb	Si
#5	50.0	30.0	20.0	--
#6	50.0	29.9	20.0	0.1
#7	50.0	29.5	20.0	0.5
#8	50.0	29.0	20.0	1.0
#9	49.0	28.0	18.0	5.0

5.1 Microstructure of the as-cast alloys

Figure 51 shows the microstructure of the as-cast alloys in table 11. Between the dendrite arms of BCC primary phase, high Cr region appears in which $NbCr_2$ is included. Although the composition of alloys is close to each other, the volume fraction of $NbCr_2$ phase increases with increasing Si addition up to 1 %. It strongly suggests that the relative phase stability of Laves $NbCr_2$ is enhanced by the addition of Si. The corresponding XRD results are shown in Fig. 54. The $NbCr_2$ in alloys 0.5Si and 1Si are confirmed to be C14 Laves phases. No obvious C14 Laves phase peaks are observed for alloys 0Si and 0.1Si due to the low volume fraction of $NbCr_2$.

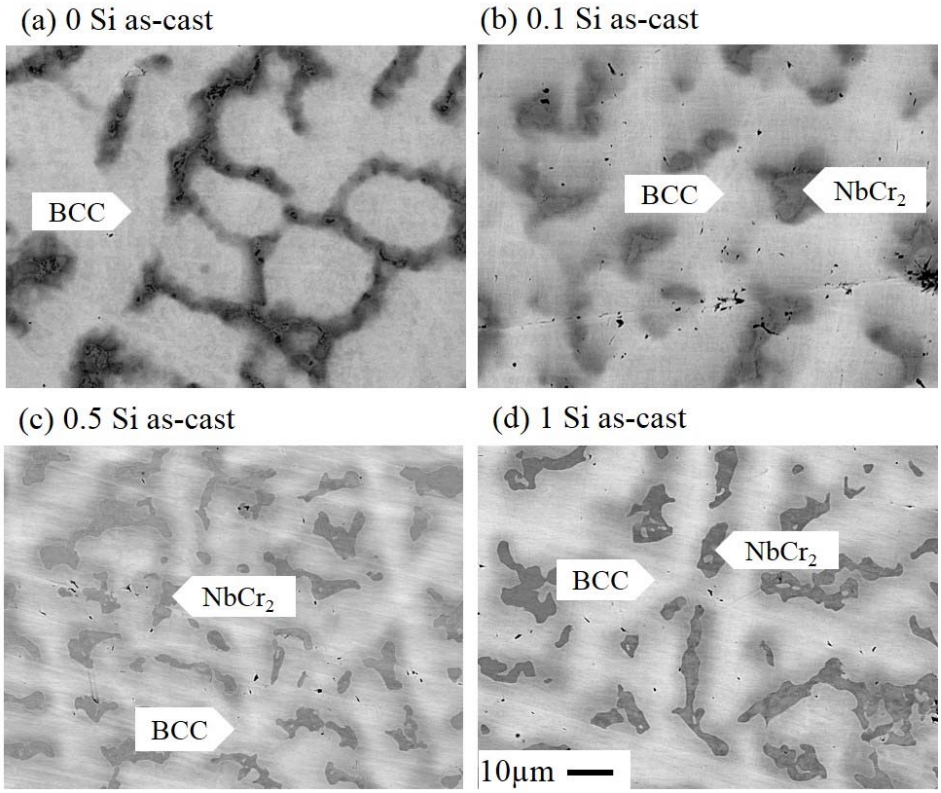

Fig. 53. Microstructure of the as-cast alloys.

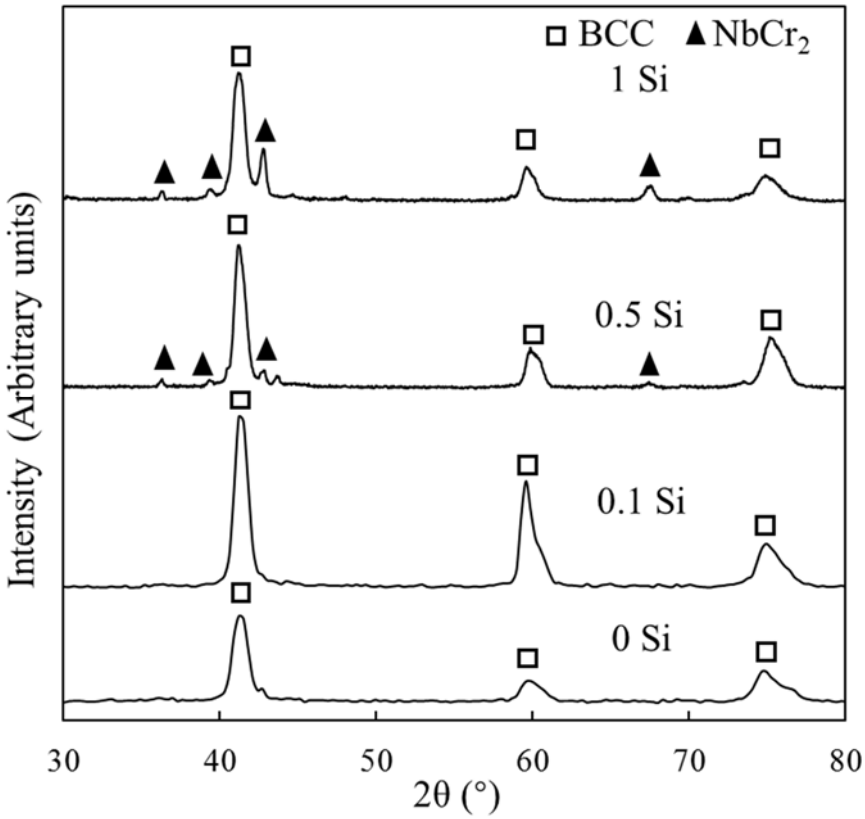

Fig. 54. XRD patterns of the as-cast alloys.

The composition of Laves NbCr2 in as-cast specimens is summarized in Table 13 and Fig. 55. The WDS results shows that Si tends to substitute for Cr-site, and Mo may mainly substitute for Nb-site. Interesting thing is that the amount of Mo increases with increasing the amount of Si in alloys.

Table 13 WDS results of $NbCr_2$ in as-cast alloys

	Cr	Mo	Nb	Si
0 Si	63.5	6.4	30.1	--
0.1 Si	62.8	6.9	29.1	1.2
0.5 Si	57.4	10.3	28.1	4.2
1 Si	54.8	10.9	28.6	5.6

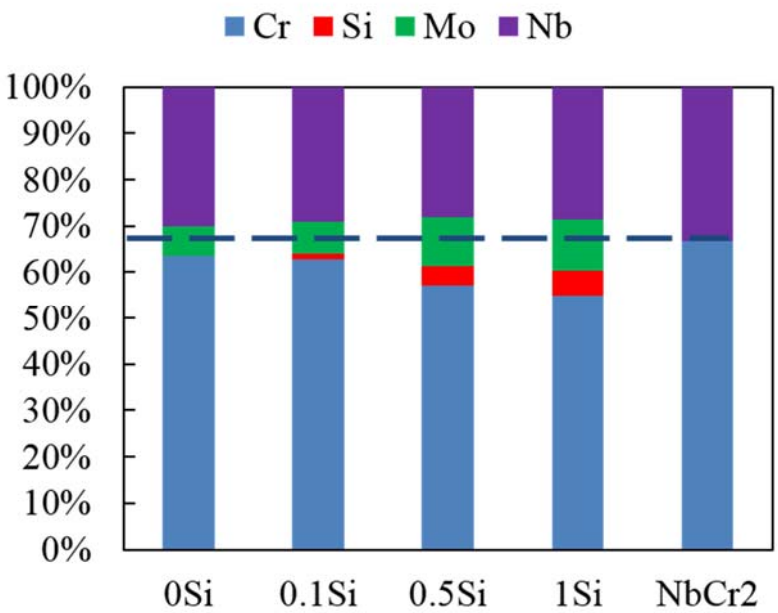

Fig. 55. Composition change of $NbCr_2$ in as-cast alloys.

5.2 Microstructure of the alloys heat-treated at 1973 K

The microstructure of alloys heat-treated at 1973 K is shown in Fig. 56. NbCr2 phase disappeared in Si-free alloy and low Si alloy, however, larger amounts of NbCr2-based Laves phases are found in higher Si alloys. The compositions of the Laves phase and BCC phase of alloys are plotted on the Cr-Mo-Nb projection (Fig. 58). It is obvious that Si changes the solvus line of BCC phase systematically towards Mo-rich direction. The amount of Mo increases with increasing the amount of Si also in heat-treated alloys. Furthermore, it is found that almost all of Si distributes to Laves phase, as shown in Table 14 and Fig. 59. These experimental results strongly suggest the stabilization of NbCr2 is enhanced by co-doping of Mo and Si. According to the XRD patterns in Fig. 57(b) together with the Cr-Nb binary phase diagram and Cr-Nb-Si ternary phase diagram, the crystal structure of Laves phase is C14, not C15, during solidification and heat-treatment at 1973 K. Therefore, the formation enthalpy of C14-NbCr2 with and without Mo and Si are calculated for comparison.

Figure Fig. 61 shows the Cr-Mo-Nb-Si quaternary system with a $NbCr_2$-"$NbSi_2$"-"$MoSi_2$"-"$MoCr_2$" plane and the change in formation enthalpy H and average atomic volume V_{ave} of C14-$NbCr_2$ with Si and/or Mo addition. Here, the Laves phases with " " are unstable and not found. Two different conditions are considered when Si substitute for the Cr-sites of 2a or 6h, while Mo substitutes for Nb-site (4f).

The calculation results show that the change in average atomic volume of phases is systematic and seemingly in good agreement with the fact that the size of Mo and Si is smaller than that of Nb and Cr, respectively. It is found that the Mo addition increases the formation enthalpy, i.e., destabilization of $NbCr_2$, even with a calculation condition in which Mo occupies Nb-site. This result is consistent with the fact that there is no stable $MoCr_2$ laves phase, and also implies the destabilization of Laves phase $NbCr_2$ with Mo suggested in terms of the atomic size ratio concept.

On the other hand, the Si addition is found to decreases the formation enthalpy of $NbCr_2$, i.e., $NbCr_2$ is stabilized. This result is also consistent with the stabilization of

Laves phase $NbCr_2$ with Si suggested in terms of the atomic size ratio concept as discussed above.

Interesting thing is that the change in formation enthalpy by Si addition to $NbCr_2$ with Mo on Nb-site is larger than that to Mo-free $NbCr_2$. It suggests that co-doping of Mo and Si enhance the stabilization of $NbCr_2$, i.e., some additional contribution (a synergetic effect) of co-doping of Mo and Si into $NbCr_2$ to the phase stability of $NbCr_2$, although $NbCr_2$ with Mo is less stable. This is also consistent with the above discussion that the atomic size ratio of Mo/Si which is smaller than that of Nb/Cr may have some positive contribution to the stabilization of $NbCr_2$.

This result of DFT calculation is consistent with the experimental results and support the stabilization of $NbCr_2$ Laves phase with co-doped Mo and Si. Also, the conclusion is consistent with the phase stability of the Laves phase $NbCr_2$ with Si and Mo suggested in terms of the atomic size ratio concept. A further investigation on the effect of Si on the stability of Laves phase composed of refractory metal element(s) not only in refractory-metal based materials but also in a wide range of alloys including ferrous alloys is needed.

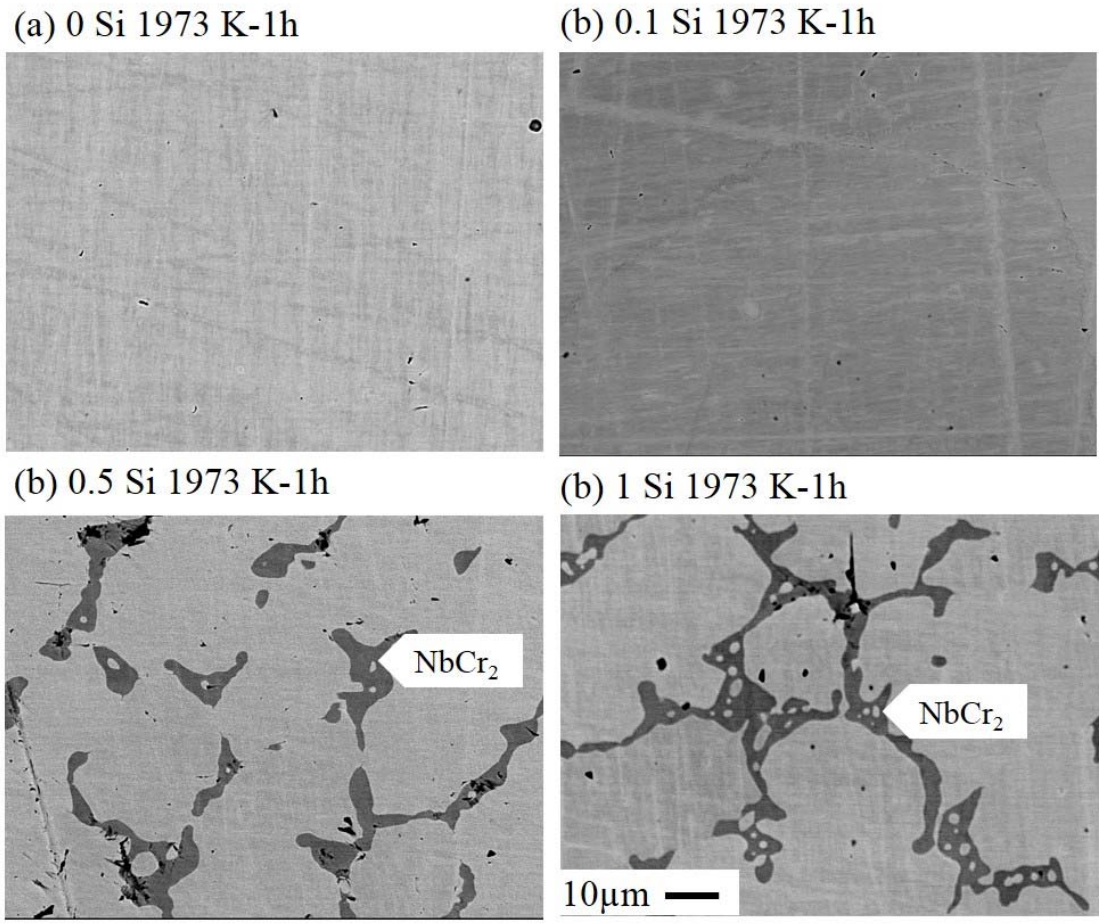

Fig. 56. SEM images of alloys heat-treated at 1973 K for 1 h.

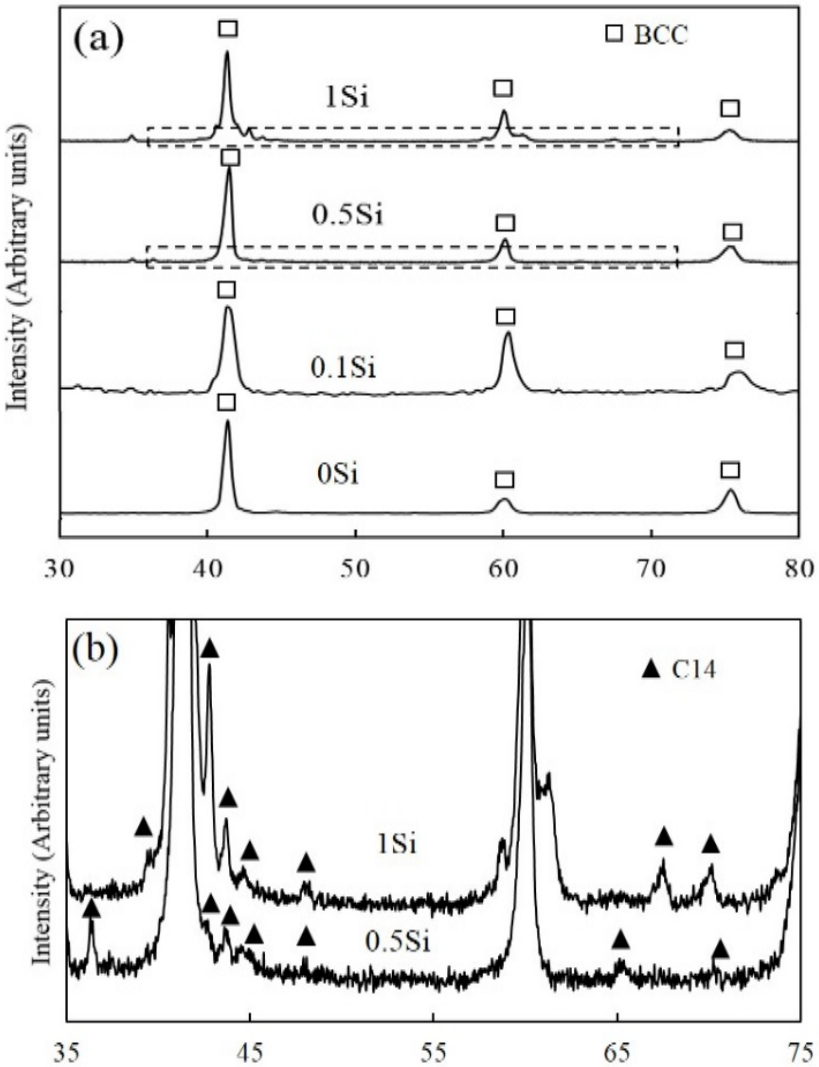

Fig. 57. (a) XRD patterns of the four alloys after heat-treatment at 1973 K, (b) enlarged patterns for alloys with 0.5Si and 1Si indicated in (a).

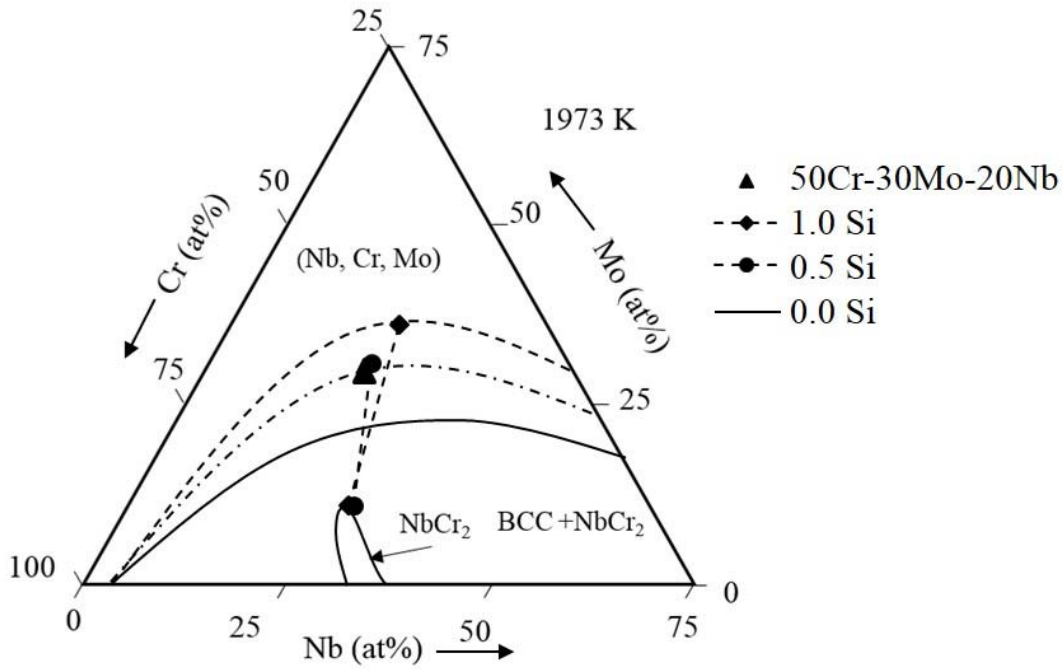

Fig. 58. BCC-$NbCr_2$ phase equilibrium at 1973 K shown in Cr-Mo-Nb projection.

Table 14 WDS results of BCC and $NbCr_2$ in high Si alloys heat-treated at 1973 K for 1 h.

	phase	Cr	Mo	Nb	Si
0.5Si	BCC	48.6	30.5	20.6	0.3
	$NbCr_2$	56.2	11.2	28.0	4.6
1Si	BCC	42.4	35.6	21.3	0.7
	$NbCr_2$	53.5	11.3	28.4	6.8

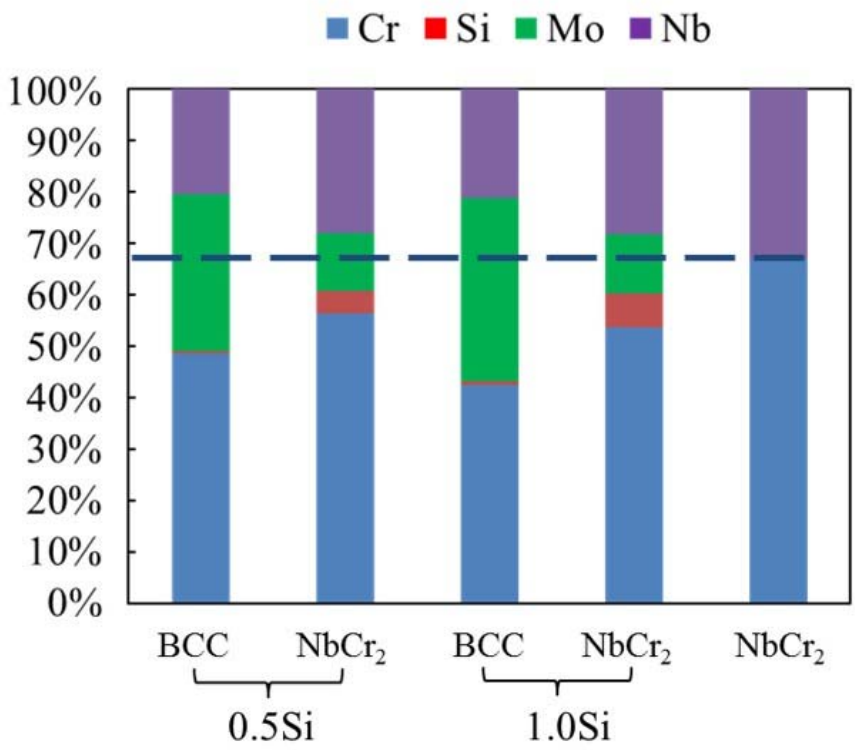

Fig. 59. Compositions of BCC and $NbCr_2$ in high Si alloys heat-treated at 1973 K.

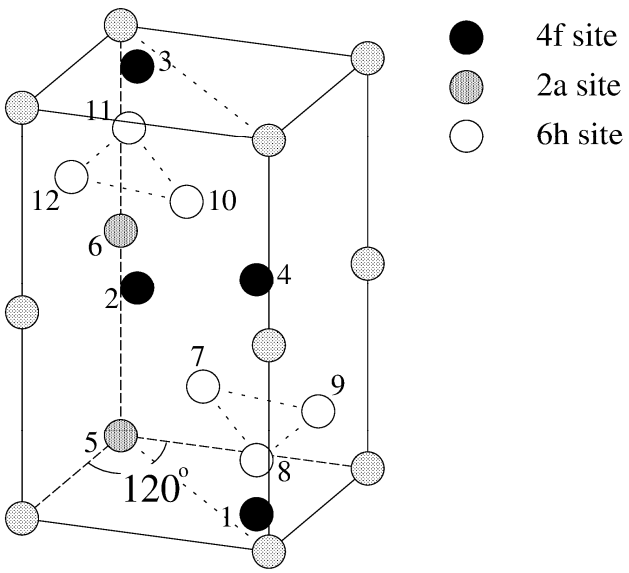

Fig. 60. Position of atoms in C14 structure.

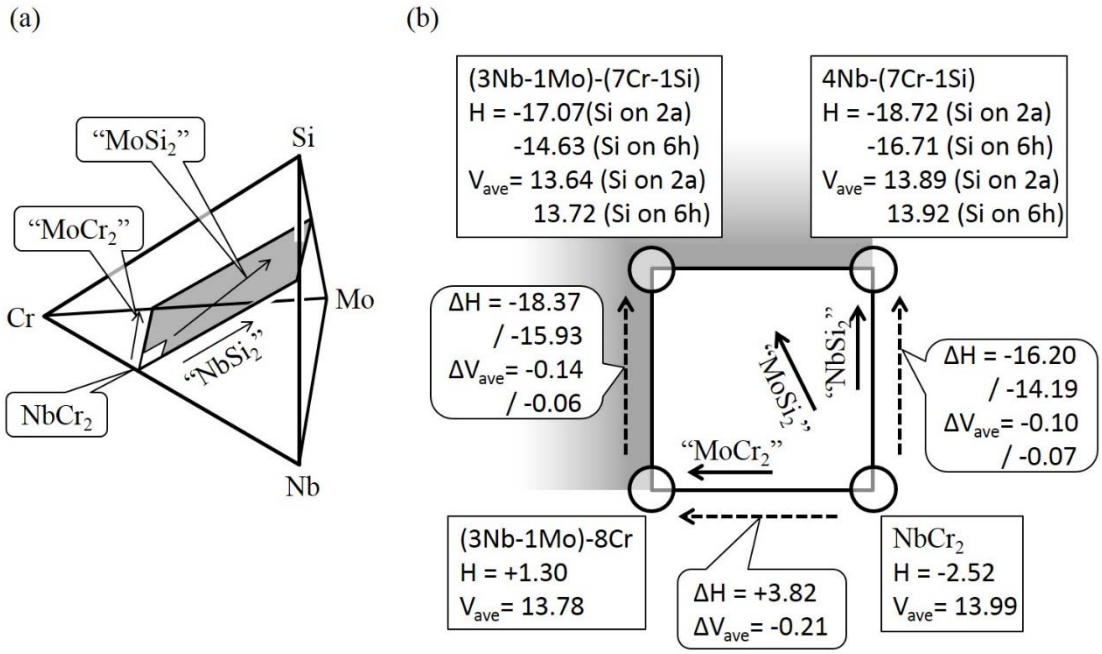

Fig. 61. (a) Cr-Mo-Nb-Si quaternary system with $NbCr_2$- "$NbSi_2$"- "$MoSi_2$"- "$MoCr_2$" plane and (b) change in formation enthalpy H (kJ/mol-atom) and average atomic volume V_{ave} (nm^3/atom) of C14-$NbCr_2$ with Si and/or Mo addition.

5.3 Microstructure of the alloys aged at 1573 K

Fig. 62 shows the microstructure of alloys aged at 1573 K for various time periods after solution-treatment at 1973 K for 1 hour. Laves phases precipitate from the supersaturated solid solution single phase in alloys 0Si and 0.1Si. Besides the precipitation Laves phases, the remaining Laves phases from solution-treatment at 1973 K are also observed for alloys 0.5Si and 1Si. The corresponding XRD results are shown in Fig. 63. For no Si and low Si alloys, the polytype of the $NbCr_2$ Laves phases is identified to be C15. However, for the relatively high Si alloys 0.5Si and 1Si, the polytype of the $NbCr_2$ Laves phase is identified to be C14. The remaining Laves phase from solution-treatment at 1973 K remains C14 even after aging at 1573 K. The WDS results in Table 15 shows that the Laves phases have high solid solubility of Si. This indicates that the Si tends to stabilize the C14 Laves phase.

According to Cr-Mo-Nb ternary phase diagram, Mo tends to occupy Nb-site in $NbCr_2$ [48, 61]. The stability of the AB_2 Laves phase is known to be governed by the size ratio of constituent atoms R_A/R_B, the number of valence electron per atom, and electron negativity [26, 30, 36-38]. One of the authors reported that the size of constituent atoms in ternary Laves phase is quite important [48]. In the Cr-Mo-Nb system, the size of Mo atom is smaller than Nb [123] and the atomic size ratio Mo/Cr is 1.088, much smaller than Nb/Cr ratio of 1.144 (see Table 1). The atomic size ratio for the Laves phase is reported to be ranging from 1.05 to 1.68 [24, 25]. Therefore, $NbCr_2$ might be de-stabilized by Mo addition.

On the other hand, Si has a smaller atomic size than that of Cr. The larger atomic size ration of Nb/Si (1.222) than that of Nb/Cr (1.144) is close to the ideal ratio of 1.225, which might be beneficial to stabilize $NbCr_2$.

Moreover, the atomic size ration of Mo/Si (1.162) is larger than that of Nb/Cr (1.144). It suggests that co-doping of Mo and Si to $NbCr_2$ may enhance the stability of the Laves phase.

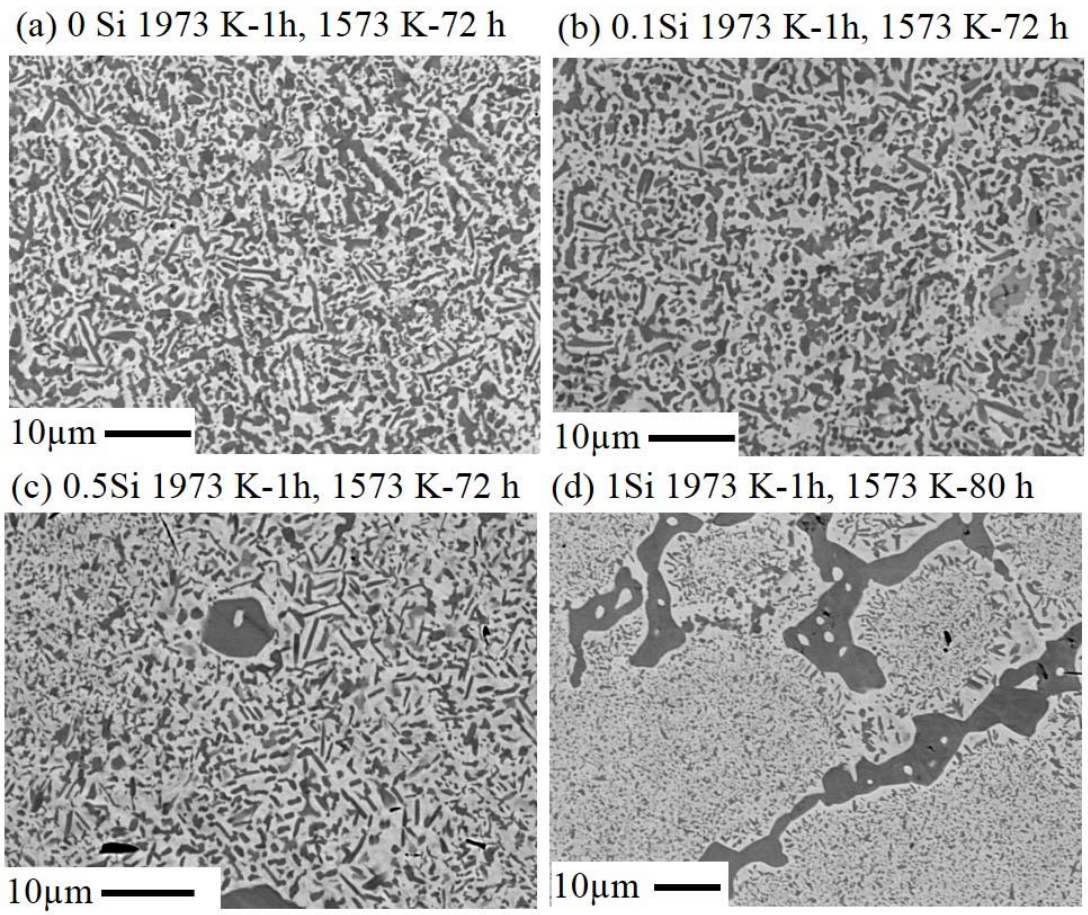

Fig. 62. SEM images of alloys heat-treated at 1573 K after solution treatment at 1973 K.

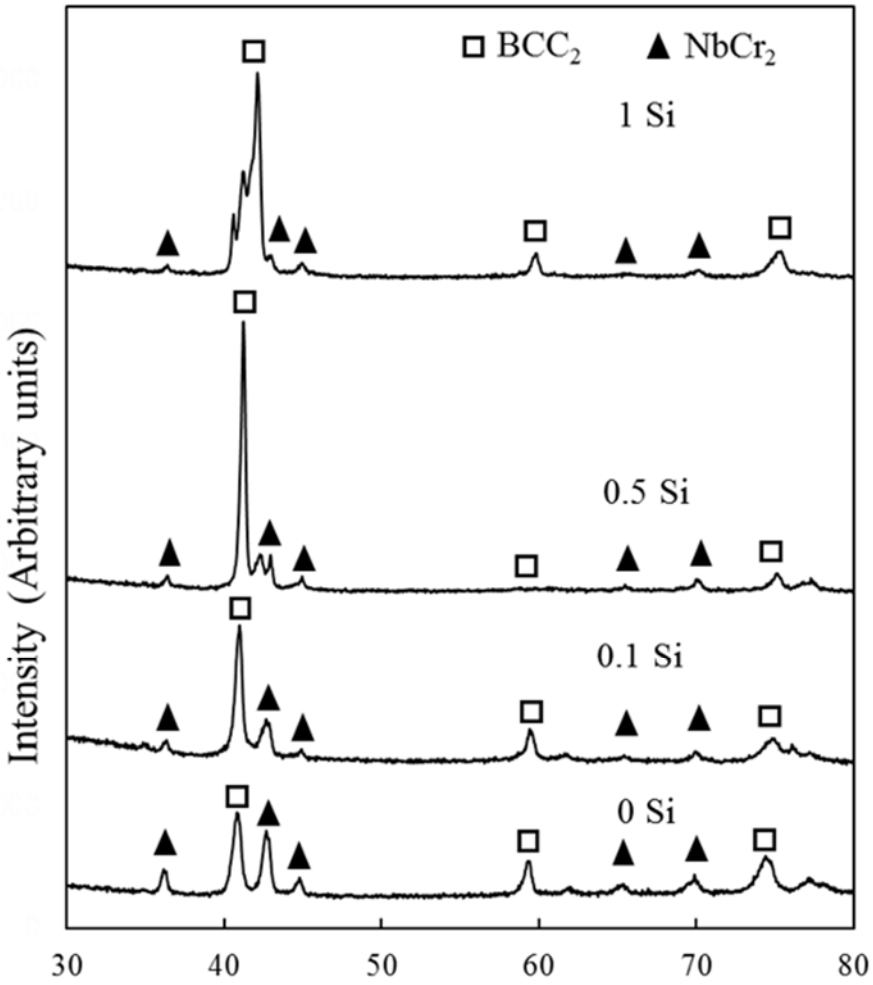

Fig. 63. XRD results corresponding to the alloys in Fig. 62.

Table 15 WDS results of $NbCr_2$ in alloys heat-treated at 1573 K after solution treatment.

	Cr	Mo	Nb	Si
0.5 Si	60.7	9.5	27.6	2.1
1 Si	59.6	9.6	26.8	4.0

Table 16 The atomic radii of elements [123].

	Nb	Mo	Cr	Si
Atomic radius (r/nm)	0.143	0.136	0.125	0.117

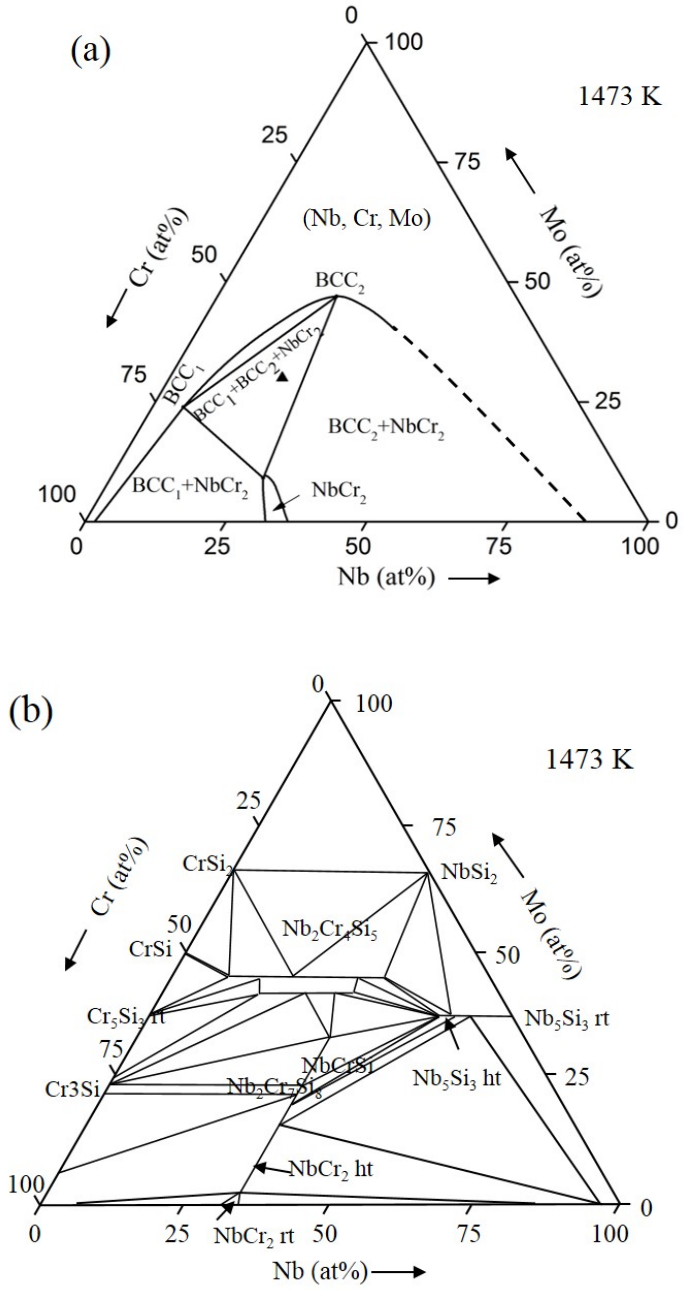

Fig. 64. Reported ternary phase diagrams (a) Cr-Mo-Nb [124] and (b) Cr-Nb-Si [125].

5.4 Summary

We conducted the experimental study on the stability of $NbCr_2$ Laves phase in Cr-Mo-Nb system with small amount of Si. The results are compared with the results of DTF calculations and concluded as follows:

(1) It is found that the amount of Laves phase in as-cast increases with the increase of the Si addition, which strongly suggests that the relative phase stability of Laves $NbCr_2$ is enhanced by the addition of Si. The $NbCr_2$ in alloys 0.5Si and 1Si are confirmed to be C14 Laves phases. No obvious C14 Laves phase peaks are observed for alloys 0Si and 0.1Si due to the low volume fraction of $NbCr_2$.

(2) NbCr2 phase disappeared in Si-free alloy and low Si alloy 0.1Si, however, larger amounts of NbCr2-based Laves phases are found in higher Si alloys 0.5Si and 1Si.

(3) It is found that Si is enriched in $NbCr_2$ phase and Mo is also tend to be distributed into the Laves phase. It indicates that $NbCr_2$ is relatively stabilized with Si addition and the solvus line of BCC moves towards Mo-rich direction.

(4) Laves phases precipitate from the supersaturated solid solution single phase in alloys 0Si and 0.1Si. Besides the precipitation Laves phases, the remaining Laves phases from solution-treatment at 1973 K are also observed for alloys 0.5Si and 1Si. For no Si and low Si alloys, the polytype of the $NbCr_2$ Laves phases is identified to be C15. However, for the relatively high Si alloys 0.5Si and 1Si, the polytype of the $NbCr_2$ Laves phase is identified to be C14.

(5) The obtained results are consistent with the phase stability of the Laves phase $NbCr_2$ with Mo and Si suggested in terms of the atomic size ratio concept.

Chapter 6

Conclusions

The BCC_1-BCC_2-$NbCr_2$ three-phase alloy in the Cr-Mo-Nb system is proposed. Based on the isothermal sections of the Cr-Mo-Nb ternary phase diagram at 1473 K, the precipitation behavior of C15 $NbCr_2$ Laves phase in various alloys at 1473 K was investigated using SEM, XRD, and EBSD. the microstructure evolution of the three-phase alloy was also investigated using EPMA and TEM, and the fracture behavior was examined using Vickers hardness and compression tests at room temperature. The hardness of each phase was also measured using nanointendation tests to understand how these phases affect the mechanical properties of the alloys. silicon has been chosen to add to the Cr-Mo-Nb system to study the stability of $NbCr_2$ Laves phase. The conclusions are summarized as follows:

(1) A three-phase region is found in the isothermal section of Cr-Mo-Nb ternary phase diagram at 1473 K. The three-phase region is composed of Cr-rich BCC_1, Mo-rich BCC_2 and C15 Laves phase. No three-phase region appears at 1773 K.

(2) The C15 $NbCr_2$ Laves precipitation morphology is quite different in the three alloys of #1, #2, and #3. After two-step heat treatment, gray precipitates appear at the GB and cellular structure is formed in alloy #1, while precipitates appear not only at the GB but also in the grain interior in alloy #3. Alloy #2 is turned out to be a three-phase alloy which consisted of fine lamellar structure of two BCC phases with relatively larger Laves precipitates.

(3) OR 1 and OR 2 with low lattice misfit are both observed between BCC matrix phase and C15 precipitates in alloys #3 and #2. Besides, OR 3 with a relatively larger δ value is also found in alloy #2, which may be resulted from existence of the phase boundaries of BCC_1 and BCC_2 formed after BCC decomposition. It seems the limit value is seemingly 8% for the formation of matching interface between BCC matrix and Laves precipitates.

(4) During aging at 1473 K after solution treatment, fast intragranular nucleation of the Cr-rich BCC_1 phase induces precipitation of alternating BCC_1/BCC_2 phases through a DP process, which maintains a stable morphology with increasing aging time.

(5) The Laves phase forms at BCC phase GBs and BCC_1/BCC_2 interphase boundaries. The growth of the Laves phase in BCC_1/BCC_2 two-phase areas consumes the Cr-rich BCC_1 phase in the vicinity.

(6) Higher-temperature heat treatment results in higher BCC decomposition and Laves phase precipitation rates, while at 1773 K no BCC decomposition occurs and a BCC/Laves two-phase structure is formed.

(7) The alloy aged at 1473 K for 72 h following solution treatment at 1973 K exhibits a hardness of 839±8 HV and has better toughness than that for an alloy directly annealed at 1473 K because no obvious microcracks were observed after the Vickers hardness test, even under a load of 0.5 kgf for 30 s.

(8) A minimum hardness and a highest fracture strength of 1493 MPa are obtained for the alloy aged at 1473 K for 24 h, where the two BCC phases dominate the microstructure. The volume fraction of the $NbCr_2$ Laves phase has a relatively small effect on the crack initiation strength.

(9) It is found that the amount of Laves phase in as-cast increases with the increase of the Si addition, which strongly suggests that the relative phase stability of Laves $NbCr_2$ is enhanced by the addition of Si. The $NbCr_2$ in alloys 0.5Si and 1Si are confirmed to be C14 Laves phases. No obvious C14 Laves phase peaks are observed for alloys 0Si and 0.1Si due to the low volume fraction of $NbCr_2$.

(10) NbCr2 phase disappeared in Si-free alloy and low Si alloy 0.1Si, however, larger amounts of NbCr2-based Laves phases are found in higher Si alloys 0.5Si and 1Si.

(11) It is found that Si is enriched in $NbCr_2$ phase and Mo is also tend to be distributed into the Laves phase. It indicates that $NbCr_2$ is relatively stabilized with Si addition and the solvus line of BCC moves towards Mo-rich direction.

(12) Laves phases precipitate from the supersaturated solid solution single phase in

alloys 0Si and 0.1Si. Besides the precipitation Laves phases, the remaining Laves phases from solution-treatment at 1973 K are also observed for alloys 0.5Si and 1Si. For no Si and low Si alloys, the polytype of the $NbCr_2$ Laves phases is identified to be C15. However, for the relatively high Si alloys 0.5Si and 1Si, the polytype of the $NbCr_2$ Laves phase is identified to be C14.

(13) The existence of Laves phase at 1973 K are consistent with the phase stability of the Laves phase $NbCr_2$ with Mo and Si suggested in terms of the atomic size ratio concept that co-doping of Mo and Si to $NbCr_2$ may enhance the stability of the Laves phase.

References

[1] A. Sengupta, S.K. Putatunda, L. Bartosiewicz, J. Hangas, P.J. Nailos, M. Peputapeck, F.E. Alberts, J Mater Eng Perform, 3 (1994) 664-672.

[2] T. Murakumo, Y. Koizumi, K. Kobayashi, H. Harada, Superalloys, (2004) 155-162.

[3] M.V. Nathal, Metall Trans A, 18 (1987) 1961-1970.

[4] Y. Wang, Z.K. Liu, L.Q. Chen, Acta Materialia, 52 (2004) 2665-2671.

[5] Q. Wu, S.S. Li, Computational Materials Science, 53 (2012) 436-443.

[6] C. Jiang, D.J. Sordelet, B. Gleeson, Acta Materialia, 54 (2006) 1147-1154.

[7] R.C. Reed, The superalloys : fundamentals and applications, Cambridge University Press, Cambridge, UK ; New York, 2006.

[8] M.J. Donachie, S.J. Donachie, Superalloys : a technical guide, 2nd ed., ASM International, Materials Park, OH, 2002.

[9] S.G. Tian, M.G. Wang, H.C. Yu, X.F. Yu, T. Li, B.J. Qian, Mat Sci Eng a-Struct, 527 (2010) 4458-4465.

[10] A. Heckl, S. Neumeier, S. Cenanovic, M. Goken, R.F. Singer, Acta Materialia, 59 (2011) 6563-6573.

[11] P. Caron, Superalloys, 2000 (2000) 737-746.

[12] C.W. Brown, J.E. King, M.A. Hicks, Metal Science, 18 (1984) 374-380.

[13] A.K. Jena, M.C. Chaturvedi, J Mater Sci, 19 (1984) 3121-3139.

[14] R.A. MacKay, T.P. Gabb, A. Garg, R.B. Rogers, M.V. Nathal, Materials Characterization, 70 (2012) 83-100.

[15] Z.N. Bi, J.X. Dong, L. Zheng, X.S. Xie, J Mater Sci Technol, 29 (2013) 187-192.

[16] X.G. Liu, L. Wang, L.H. Lou, J. Zhang, J Mater Sci Technol, 31 (2015) 143-147.

[17] Y. Ru, S.S. Li, Y.L. Pei, J. Zhou, S.K. Gong, H.B. Xu, J Alloy Compd, 662 (2016) 431-435.

[18] V. Biss, G.N. Kirby, D.L. Sponseller, Metallurgical Transactions A, 7 (1976) 1251-1261.

[19] C. Rae, M. Karunaratne, C. Small, R. Broomfield, C. Jones, R. Reed, Superalloys, 2000 (2000) 767-776.

[20] S.G. Tian, M.G. Wang, T. Li, B.J. Qian, J. Xie, Mat Sci Eng a-Struct, 527 (2010) 5444-5451.

[21] B.P. Bewlay, M.R. Jackson, J.C. Zhao, P.R. Subramanian, Metallurgical and Materials Transactions A, 34A (2003) 2043-2052.

[22] K. Li, S. Li, Y. Xue, H. Fu, International Journal of Refractory Metals and Hard Materials, 36 (2013) 154-161.

[23] F. Laves, Naturwissenschaften, 27 (1939) 65-73.

[24] D.J. Thoma, J.H. Perepezko, J Alloy Compd, 224 (1995) 330-341.

[25] T. Yamanouchi, S. Miura, Materials Transactions, 59 (2018) 546-555.

[26] F. Stein, M. Palm, G. Sauthoff, Intermetallics, 12 (2004) 713-720.

[27] S.B. Roy, P. Chaddah, Pramana-J Phys, 53 (1999) 659-684.

[28] I. Ansara, T.G. Chart, A.F. Guillermet, F.H. Hayes, U.R. Kattner, D.G. Pettifor, N.

Saunders, K. Zeng, Calphad, 21 (1997) 171-218.
[29] J.H. Westbrook, Intermetallic compounds, Wiley, New York, 1967.
[30] C. Li, C.L. Liu, F.S. Li, Q.H. Gong, Chem Phys Lett, 380 (2003) 201-205.
[31] A.E. Dwight, Trans. ASM, 53 (1961) 479.
[32] F. Laves, Naturwissenschaften, 25 (1937) 721-733.
[33] G. Leitner, G. Schulze, Cryst Res Technol, 6 (1971) 449-463.
[34] J.H. Zhu, C.T. Liu, L.M. Pike, P.K. Liaw, Intermetallics, 10 (2002) 579-595.
[35] J.H. Zhu, C.T. Liu, L.M. Pike, P.K. Liaw, Metallurgical and Materials Transactions A, 30 (1999) 1449-1452.
[36] A.R. Edwards, Metall Trans, 3 (1972) 1365-1372.
[37] F. Laves, H. Witte, Metallwirschaft, (1936) 840.
[38] J.H. Zhu, C.T. Liu, P.K. Liaw, Intermetallics, 7 (1999) 1011-1016.
[39] C.T. Liu, J.H. Zhu, M.P. Brady, C.G. McKamey, L.M. Pike, Intermetallics, 8 (2000) 1119-1129.
[40] J.H. Zhu, P.K. Liaw, C.T. Liu, Mat Sci Eng a-Struct, 240 (1997) 260-264.
[41] R.L. Berry, G.V. Raynor, Acta Crystallogr, 6 (1953) 178-186.
[42] R.L. Johannes, R. Haydock, V. Heine, Phys Rev Lett, 36 (1976) 372-376.
[43] Y. Ohta, D.G. Pettifor, J Phys-Condens Mat, 2 (1990) 8189-8194.
[44] A. Von Keitz, G. Sauthoff, P. Neumann, Z Metallkd, 89 (1998) 803-810.
[45] P. Villars, K. Brandenburg, M. Berndt, S. LeClair, A. Jackson, Y.H. Pao, B. Igelnik, M. Oxley, B. Bakshi, P. Chen, S. Iwata, J Alloy Compd, 317 (2001) 26-38.
[46] D.G. Pettifor, Mater Sci Tech Ser, 4 (1988) 675-691.
[47] T. Takasugi, M. Yoshida, S. Hanada, J Mater Res, 10 (1995) 2463-2470.
[48] T. Takasugi, M. Yoshida, S. Hanada, Acta Materialia, 44 (1996) 669-674.
[49] M. Yoshida, T. Takasugi, Materials Science and Engineering A, 224 (1997) 69-76.
[50] Y.L. Xue, S.M. Li, H. Zhong, H.Z. Fu, Materials Science and Engineering A, 638 (2015) 340-347.
[51] A. Bhowmik, H.J. Stone, J Mater Sci, 48 (2013) 3283-3293.
[52] D.J. Thoma, F. Chu, P. Peralta, Materials Science and Engineering A, 239-240 (1997) 251–259.
[53] T. Takasugi, M. Yoshida, J Mater Res, 13 (1998) 2505-2513.
[54] A.V. Kazantzis, M. Aindow, I.P. Jones, G.K. Triantafyllidis, J.T.M. De Hosson, Acta Materialia, 55 (2007) 1873-1884.
[55] K. Inoue, K. Tachikawa, Ieee T Magn, 13 (1977) 840-843.
[56] K. Inoue, T. Kuroda, K. Tachikawa, Ieee T Magn, 15 (1979) 635-638.
[57] J.D. Livingston, E.L. Hall, J Mater Res, 5 (1990) 5-8.
[58] F.M. Chu, D.P. Pope, Mat Sci Eng a-Struct, 170 (1993) 39-47.
[59] D.E. Luzzi, G. Rao, T.A. Dobbins, D.P. Pope, Acta Materialia, 46 (1998) 2913-2927.
[60] P.G. Kotula, C.B. Carter, K.C. Chen, D.J. Thoma, F. Chu, T.E. Mitchell, Scripta Mater, 39 (1998) 619-623.
[61] H. Okaniwa, D. Shindo, M. Yoshida, T. Takasugi, Acta Materialia, 47 (1999) 1987-

1992.
[62] D.J. Thoma, K.A. Nibur, K.C. Chen, J.C. Cooley, L.B. Dauelsberg, W.L. Hults, P.G. Kotula, Mat Sci Eng a-Struct, 329 (2002) 408-415.
[63] M. Rotter, A. Grytsiv, X.-Q. Chen, P. Rogl, R. Podloucky, W. Wolf, V.T. Witusiewicz, A. Saccone, H. Noel, M. Doerr, A. Lindbaum, H. Michor, E. Bauer, S. Heathman, W. Kockelmann, J. Taylor, Physical Review B, 74 (2006).
[64] C. Jiang, Acta Materialia, 55 (2007) 1599-1605.
[65] Q. Long, J. Wang, Y. Du, D. Holec, X. Nie, Z. Jin, Computational Materials Science, 123 (2016) 59-64.
[66] S.Q. Lu, H.Z. Zheng, M.W. Fu, Scripta Mater, 61 (2009) 205-207.
[67] W.Y. Kim, T. Takasugi, Scripta Mater, 48 (2003) 559-563.
[68] X.W. Nie, S.Q. Lu, K.L. Wang, T.C. Chen, C.L. Niu, Mat Sci Eng a-Struct, 502 (2009) 85-90.
[69] Z.Y. Wei, Y.X. Yang, J.C. Huang, B. Wu, B.S. Sa, Y.Y. Huang, S.L. Wang, M.H. Lin, C.T. Tsai, K.W. Bai, Intermetallics, 96 (2018) 33-40.
[70] Q. Yao, J. Sun, Y. Zhang, B. Jiang, Acta Materialia, 54 (2006) 3585-3591.
[71] A. Bhowmik, H.J. Stone, Metallurgical and Materials Transactions A, 43 (2012) 3283-3292.
[72] A. Bhowmik, R.J. Bennett, B. Monserrat, G.J. Conduit, L.D. Connor, J.E. Parker, R.P. Thompson, C.N. Jones, H.J. Stone, Intermetallics, 48 (2014) 62-70.
[73] Y. Xue, S. Li, H. Zhong, K. Li, H. Fu, J Alloy Compd, 684 (2016) 403-411.
[74] K. Li, R. Hao, C. Di, D. Gong, J Mater Res, 31 (2016) 2214-2222.
[75] T. Takasugi, K.S. Kumar, C.T. Liu, E.H. Lee, Mat Sci Eng a-Struct, 260 (1999) 108-123.
[76] M. Yoshida, T. Takasugi, Materials Science and Engineering A, 224 (1997) 77-86.
[77] K.S. Kumar, D.B. Miracle, Intermetallics, 2 (1994) 257-274.
[78] M. Takeyama, C.T. Liu, Mat Sci Eng a-Struct, 132 (1991) 61-66.
[79] K.W. Li, S.M. Li, Y.L. Xue, H.Z. Fu, Int J Refract Met H, 36 (2013) 154-161.
[80] M. Fujita, Y. Kaneno, T. Takasugi, J Alloy Compd, 424 (2006) 283-288.
[81] D.L. Davidson, K.S. Chan, D.L. Anton, Metall Mater Trans A, 27 (1996) 3007-3018.
[82] T. Ohta, Y. Nakagawa, Y. Kaneno, H. Inoue, I.T. Takasugi, W.Y. Kim, J Mater Sci, 38 (2003) 657-665.
[83] K.W. Li, T. Wang, C. Di, D.Q. Gong, Vacuum, 131 (2016) 28-33.
[84] B.P. Bewlay, J.A. Sutliff, M.R. Jackson, H.A. Lipsitt, Acta Metallurgica Et Materialia, 42 (1994) 2869-2878.
[85] D.J. Thoma, J.H. Perepezko, D.H. Plantz, R.B. Schwarz, Mat Sci Eng a-Struct, 179-180 (1994) 176-180.
[86] T.M. Pollock, S. Tin, Journal of Propulsion and Power, 22 (2006) 361-374.
[87] H. Okamoto, Desk handbook: phase diagrams for binary alloys, 2nd ed., ASM International, Materials Park, Ohio, 2010.
[88] K.S. Kumar, C.T. Liu, Acta Materialia, 45 (1997) 3671-3686.

[89] J. Ventura, B. Portillo, S.K. Varma, J Alloy Compd, 476 (2009) 257-262.
[90] V.N. Svechnikov, G.F. Kobzenko, Dopov. Akad. Nauk Ukr. RSR, (1964) 492-498.
[91] C. Wang, B. Chen, Y. Chen, J. Zhang, S. Yang, Z. Shi, X. Liu, Journal of Xiamen University (Natural Science), (2017).
[92] M.I. Zakharova, D.A. Prokoshkin, Izv. Akad. Nauk SSSR, Otd. Tekh. Nauk, Metall, Topl., (1961) 59-67.
[93] K.C. Chen, S.M. Allen, J.D. Livingston, J Mater Res, 12 (1997) 1472-1480.
[94] A. Bhowmik, K.M. Knowles, H.J. Stone, Intermetallics, 31 (2012) 34-47.
[95] Y.L. Xue, S.M. Li, K.W. Li, H. Zhong, H.Z. Fu, Materials Chemistry and Physics, 167 (2015) 119-124.
[96] F. Chu, Y.C. Lu, P.G. Kotula, T.E. Mitchell, D.J. Thoma, Philos Mag A, 77 (1998) 941-956.
[97] D.P. Pope, F.M. Chu, Philos Mag A, 69 (1994) 409-420.
[98] Y. Kimura, D.E. Luzzi, D.P. Pope, Materials Science and Engineering A, 329–331 (2002) 241–248.
[99] M. Yoshida, T. Takasugi, Intermetallics, 10 (2002) 85-93.
[100] B.L. Bramfitt, Metall Trans, 1 (1970) 1987-1995.
[101] Y.S. Touloukian, R.K. Kirby, R.E. Taylor, P.D. Desal, Thermal Expansion: Metallic elements and Alloys, Plenum, New York, 1975.
[102] H.J. Goldschmidt, J.A. Brand, Journal of the Less-Common Metals, 3 (1961) 44-61.
[103] B.D. Cullity, Elements of X-ray Diffraction, 2nd ed., Reading, Mass. : Addison-Wesley Pub. Co., 1978.
[104] E. Rudy, Ternary phase equilibria in transition metal-boron-carbon-silicon systems. part 5. compendium of phase diagram data, Aerojet-General Corp Sacramento Ca Materials Research Lab, 1969.
[105] B. Mayer, H. Anton, E. Bott, M. Methfessel, J. Sticht, J. Harris, P.C. Schmidt, Intermetallics, 11 (2003) 23-32.
[106] I. Manna, Interface Sci, 6 (1998) 113-131.
[107] S. Ueta, M. Hida, M. Kajihara, ISIJ International, 53 (2013) 347-355.
[108] P. Zięba, Archives of Metallurgy and Materials, 62 (2017) 955-968.
[109] H. Ramanarayan, T.A. Abinandanan, Physica A, 318 (2003) 213-219.
[110] J.M. Park, Applied Mathematics and Computation, 330 (2018) 11-22.
[111] L.Q. Chen, Acta Metallurgica et Materialia, 42 (1994) 3503-3513.
[112] S. Puri, Journal of Physics: Condensed Matter, 17 (2005) R101-R142.
[113] H.R. Cui, F. Sun, K. Chen, L.T. Zhang, R.C. Wan, A.D. Shan, J.S. Wu, Materials Science and Engineering A, 527 (2010) 7505-7509.
[114] Y. Xu, M. Wang, Y. Wang, T. Gu, L. Chen, X. Zhou, Q. Ma, Y. Liu, J. Huang, J Alloy Compd, 621 (2015) 93-98.
[115] S. Miura, T. Hatabata, T. Okawa, T. Mohri, Metallurgical and Materials Transactions A, 45 (2014) 1136-1147.
[116] M. Krüger, P. Jain, K.S. Kumar, M. Heilmaier, Intermetallics, 48 (2014) 10-18.

[117] D. Casellas, J. Caro, S. Molas, J.M. Prado, I. Valls, Acta Materialia, 55 (2007) 4277-4286.
[118] A. Von Keitz, G. Sauthoff, Intermetallics, 10 (2002) 497-510.
[119] J.A. Hanna, I. Baker, M.W. Wittmann, P.R. Munroe, J Mater Res, 20 (2005) 791-795.
[120] H.J. Dorantes-Rosales, V.M. Lopez-Hirata, J.L. Gonzalez-Velazquez, N. Cayetano-Castro, M.L. Saucedo-Muñoz, Precipitation Process in Fe-Ni-Al-based Alloys, Superalloys, InTech, 2015, pp. 77-100.
[121] M.L. Saucedo-Muñoz, V.M. Lopez-Hirata, Scanning Electron Microscopy, InTech, 2012.
[122] A. Bhowmik, C.N. Jones, I.M. Edmonds, H.J. Stone, J Alloy Compd, 530 (2012) 169-177.
[123] P. Villars, K. Cenzual, Pearson's Crystal Data, ASM International, Materials Park, Ohio, USA, 2014/15.
[124] L. Peng, K. Ikeda, T. Horiuchi, S. Miura, Materials Transactions, 59 (2018) 1706-1715.
[125] N. David, Y. Cartigny, T. Belmonte, J.M. Fiorani, M. Vilasi, Intermetallics, 14 (2006) 464-473.